

182p
N64 11743

CODE-1

NASA CR 52921

Research
Laboratories

U

UNITED AIRCRAFT CORPORATION

A

EAST HARTFORD,
CONNECTICUT

OTS PRICE

XEROX \$ 1.50 per
MICROFILM \$ 2.00 per

UNITED AIRCRAFT CORPORATION

RESEARCH LABORATORIES

EAST HARTFORD, CONN.

8943003

(NASA CR-529213)

B910056-12) OTS: \$13.00 ph, \$5.66 mf

Investigation of
Nonequilibrium Flow Effects in
High Expansion Nozzles
Final Report

(NASA Contract NASw-366)

[7]

REPORTED BY

V. J. Sarli

→ V. J. Sarli, Program Manager

APPROVED BY

A. W. Blackman

A. W. Blackman, Chief
Rocket and Air-Breathing
Propulsion

NO. OF PAGES 123
TABLES 7
FIGURES 40

20
DATE September 20, 1963

182 p refs

Investigation of Nonequilibrium Flow Effects

in High Expansion Nozzles

Final Report

Contract No. NASw-366

TABLE OF CONTENTS

	<u>Page</u>
FOREWORD	i
SUMMARY	ii
CONCLUSIONS AND RECOMMENDATIONS	iii
INTRODUCTION	1
TASK I - RELATIVE IMPORTANCE OF EQUILIBRATION PROCESSES	3
Chemical Recombination	4
<u>Sudden Freezing Approximation</u>	5
<u>Performance Calculations</u>	7
Thermodynamic Relaxation	11
<u>Performance Calculations</u>	15
Two-Phase Flow in Rocket Nozzles	19
<u>One-Dimensional Two-Phase Flow Calculations</u>	20
<u>Performance Calculations for the Be-O₂-H₂ System</u>	21
Condensation Losses	24
Nonequilibrium Boundary Layer Effects on Nozzle Heat Transfer	24
TASK II - FINITE KINETICS NOZZLE FLOW MACHINE PROGRAMS	29
The One-Dimensional Finite Reaction Rate Analysis in Flow Systems	29
Reaction Mechanism and Thermodynamic Data for the Hydrogen-Oxygen System	31

TABLE OF CONTENTS
(Cont.)

	<u>Page</u>
One-Dimensional Performance Calculations	32
<u>Freezing Point</u>	34
<u>Scaling</u>	35
<u>Vibrational Nonequilibrium</u>	36
<u>Combustion Efficiency</u>	36
General Description of Construction of the Two-Dimensional Nozzle Decks	37
<u>Step Control for the Runge-Kutta Integration Procedure</u>	38
<u>Starting Conditions for Supersonic Calculations</u>	39
<u>Stability of Calculation Procedures</u>	39
<u>Criterion for "Freezing"</u>	39
<u>Optimization Map</u>	40
TASK III - EXPERIMENTAL PROGRAM	41
Method of Approach	41
Apparatus.	43
Test Procedure	44
Results and Discussion	46
LIST OF REFERENCES.	49
LIST OF SYMBOLS	55
APPENDIX I - DEPARTURE FROM EQUILIBRIUM IN ROCKET NOZZLES	62
APPENDIX II - CRITERION FOR DEPARTURE FROM MOLECULAR VIBRATIONAL EQUILIBRIUM	67
APPENDIX III - CONSTANT VELOCITY AND THERMAL LAGS IN TWO-PHASE FLOW	70
APPENDIX IV - ANALYSIS OF HEAT TRANSFER RATES TO NOZZLE SURFACES WITH FROZEN BOUNDARY LAYER FLOW.	72
APPENDIX V - EQUATION SYSTEM FOR THE FLOW OF A REACTING GAS MIXTURE IN A ONE-DIMENSIONAL PASSAGE	78
APPENDIX VI - THE METHOD OF CHARACTERISTICS FOR STEADY TWO-DIMENSIONAL OR AXISYMMETRIC FLOW OF A REACTING GAS	88

TABLE OF CONTENTS
(Cont.)

	<u>Page</u>
APPENDIX VII - METHOD OF CHARACTERISTICS: NUMERICAL CONSTRUCTION	97
APPENDIX VIII - DETAILED DESCRIPTION OF TEST APPARATUS	110
APPENDIX IX - DISTRIBUTION LIST	116
TABLES	124
FIGURES	131

LIST OF FIGURES

<u>Fig. No.</u>	<u>Title</u>
1	Vacuum Specific Impulse Vs Area Ratio - H_2-F_2 - Chamber Pressure = 60 psia
2	Vacuum Specific Impulse Vs Area Ratio - H_2-F_2 - Chamber Pressure = 1000 psia
3	Vacuum Specific Impulse Vs Area Ratio - $N_2H_4-N_2O_4$ - Chamber Pressure = 60 psia
4	Vacuum Specific Impulse Vs Area Ratio - $N_2H_4-N_2O_4$ - Chamber Pressure = 1000 psia
5	Vacuum Specific Impulse Vs Area Ratio - $C_6H_{14}-OF_2$ - Chamber Pressure = 60 psia
6	Vacuum Specific Impulse Vs Area Ratio - $C_6H_{14}-OF_2$ - Chamber Pressure = 1000 psia
7	Loss in Characteristic Velocity Versus Throat Geometry For Two-Phase Flow - Be- H_2-O_2 System
8	Loss in Characteristic Velocity Versus Throat Geometry For Two-Phase Flow - Be- H_2-O_2 System
9	Loss in Vacuum Specific Impulse Versus Area Ratio For Two-Phase Flow - Be- H_2-O_2 System
10	Variation of Nozzle Parameters in Nozzle Exit Cone
11	Partial Pressure B_2O_3 Versus Area Ratio and Temperature - $B_2H_6-OF_2$ - $p_c = 1000$ psia
12	Partial Pressure B_2O_3 Versus Area Ratio and Temperature - $B_2H_6-OF_2$ - $p_c = 60$ psia
13	Variation of Area Ratio and Species Concentration in Hypothetical Nozzle Configuration
14	Heat-Transfer Rate for H_2-O_2 Nozzle
15	Ratio of Convective to Total Heat Transfer for H_2-O_2 Nozzle

LIST OF FIGURES
(Cont.)

<u>Fig. No.</u>	<u>Title</u>
16	Temperature Profile Vs Area Ratio
17	Nozzle Contours for One-Dimensional Studies
18	Vacuum Specific Impulse Versus Area Ratio - Nozzle Contours I and II
19	Vacuum Specific Impulse Versus Area Ratio - Nozzle Contours I and II Cont'd
20	Mean Molecular Weight Versus Mach Number
21	Scaling Effect: Temperature Versus Area Ratio
22	Scaling Effect: Pressure Versus Area Ratio
23	Scaling Effect: Mean Molecular Weight Versus Mach Number
24	Combustion Efficiency: Vacuum Specific Impulse Versus Area Ratio
25	Combustion Efficiency: Temperature Versus Area Ratio
26	Optimization Map
27	Diagram of Experimental Apparatus
28	Schematic Diagram of Test Nozzle
29	Photograph of Test Nozzle and Traversing Mechanism
30	Five Beam Absorption Photometer
31	Photograph of Five Beam Absorption Photometer
32	Photograph of Main Test Section
33	Variation of Mach Number and Pressure Ratio With Axial Distance From Nozzle Throat
34	Transverse Pressure Distributions at Various Axial Locations in Calibration Nozzle

LIST OF FIGURES
(Cont.)

<u>Fig. No.</u>	<u>Title</u>
35	Variation of Pitot Pressure Ratio With Distance From Bottom Wall of Nozzle
36	Variation of Boundary Layer Displacement Thickness With Axial Distance From Nozzle Throat
37	Variation of Nitrogen Dioxide Concentration Ratio in the Supersonic Portion of the Test Nozzle
38	Comparison of Predicted and Measured Nitrogen Dioxide Concentration Ratios in Supersonic Portion of Test Nozzle
39	Calculated Variation of Nitrogen Dioxide Concentration Ratio in the Supersonic Portion of the Test Nozzle
40	Photomultiplier Tube Circuit

LIST OF TABLES

Table No.

- | | |
|---|--|
| 1 | Kinetic Data for H_2-F_2 System |
| 2 | Selected Rate Data for the $N_2H_4-N_2O_4$ System |
| 3 | Significant Recombination Reactions $B_2H_6-OF_2$ System |
| 4 | Reaction Mechanism and Rate Data for Hydrogen-Oxygen System |
| 5 | Summary of Performance Results for Contours Studied in Task II |
| 6 | Freezing Points for Different Throat Contours |
| 7 | Optimum Nozzle Configuration and Flow Properties |

FOREWORD

This work was performed by the United Aircraft Corporation Research Laboratories for the National Aeronautics and Space Administration under Contract NASw-366. The work was initiated under the contract on June 14, 1962.

Included among those who cooperated in the research and preparation of this report were: Dr. V. J. Sarli, Program Manager; Mr. A. W. Blackman, Chief, Rocket and Air-Breathing Propulsion Section; Dr. W. G. Burwell, Supervisor, Kinetics and Heat Transfer Group; Mr. J. R. Keilbach, Supervisor, Rocket Technology Group, and Mr. R. L. O'Brien of the Internal Aerodynamics Group of the Research Laboratories' Staff. Personnel from the Pratt & Whitney Aircraft Division of the United Aircraft Corporation included Dr. E. N. Nilson, Chief, Scientific Staff; Mr. T. F. Zupnik and Mr. D. E. Ables, members of Scientific Staff of the Advanced Power Systems Group, and Dr. F. Landis, Consultant to the Pratt & Whitney Division. Personnel from the United Technology Center of the United Aircraft Corporation included Mr. M. Gilbert, Principal Scientist; Dr. R. Dunlap, Senior Staff Scientist; and Dr. R. Hermsen, Staff Scientist of the Research and Advanced Technology Section.

This work was under the program management of Mr. H. Burlage, Jr., Chief, Liquid Propulsion Systems, NASA Headquarters, Washington, D. C., and the Technical Managers were Messrs. T. Mariani and N. Saminich, NASA Lewis Research Center, Cleveland, Ohio.

This document is unclassified in its entirety.

Investigation of Nonequilibrium Flow Effects
in High Expansion Nozzles

SUMMARY

11743

The Research Laboratories of United Aircraft Corporation under Contract NASw-366 with the NASA have performed an investigation (a) to determine the effect of nonequilibrium flow processes on the performance of high-expansion-ratio rocket exhaust nozzles and (b) to develop improved techniques for predicting the performance of high expansion ratio exhaust nozzles for rocket motors utilizing high energy liquid propellants.

Order-of-magnitude calculations were carried out for six propellant combinations to determine the relative effects on nozzle performance of lack of equilibrium in the nozzle due to continuing reaction or recombination lag, thermodynamic relaxation, velocity and thermal lags associated with two-phase flow, condensing flow, and heat transfer to a wall with a nonequilibrium boundary layer.

A machine computational program previously developed by the United Aircraft Corporation was perfected under the contract to treat the one-dimensional flow of a reacting gas mixture in a variable area passage. Using the refined program, an investigation was performed to determine the effects of throat contours, freezing point locations, constant entropy assumptions, combustion efficiency and vibrational relaxation on the theoretical performance of a nozzle designed for use with the H_2-O_2 propellant combination.

Two additional machine programs for constructing two-dimensional and axisymmetric flows with finite chemical kinetics have been completed under the contract. These consisted of a "performance deck", used to evaluate the performance for a prescribed nozzle contour, and a "design deck" used in the determination of an optimum nozzle contour.

A comparison was made between analysis and experiment for a simplified reaction system in which the recombination of nitrogen dioxide to form nitrogen tetroxide was followed. The results of this experiment are in good agreement with results computed using the "performance deck".

AUTHOR

CONCLUSIONS AND RECOMMENDATIONS

On the basis of the analytical and experimental investigation conducted under the contract, the following conclusions and recommendations are made.

1. Order of magnitude calculations employing a "sudden freezing" criterion in a hypothetical high expansion ratio exhaust nozzle show that recombination lags can reduce the nozzle specific impulse from the theoretical maximum value obtainable under equilibrium flow for all propellant systems considered. The reduction in impulse is largest at the lowest pressure employed in the analysis, 60 psia, and ranges from about 6% to 11% of the ideal impulse at an expansion ratio of 100. Reductions in nozzle specific impulse were less than 1% at 1000 psia chamber pressure for all propellant combinations studied.

2. Order of magnitude calculations of the vibrational relaxation freezing point for the propellant combinations studied under Task I suggest that no significant reduction in performance will occur because of vibrational freezing except in the case where diatomic nitrogen is present in large concentrations. Performance losses due to the presence of nitrogen may be appreciably reduced if water is also present in the exhaust nozzle flow. Freezing area ratios are generally greater than 10:1 at 60 psia (chamber) and increase markedly as chamber pressure is increased.

3. Performance losses can be considerably increased because of the velocity and thermal lags associated with two phase flow. For the Be-H₂-O₂ propellant combination in a typical nozzle configuration, specific impulse reduction can be in the order of 10 to 20% of the ideal impulse, depending upon the chamber pressure, particle size, and thrust level. These losses increase as particle size increases and decrease as pressure and thrust level increase.

4. Losses in performance due to condensation are associated only with the B₂H₆-OF₂ system of the six propellant systems studied. For the B₂H₆ system, condensation occurs well downstream of the nozzle throat and specific impulse losses are therefore not significant.

5. Changes in the heat flux to the nozzle wall are of small magnitude when nonequilibrium recombination of the H₂-O₂ system is permitted in the boundary layer. Under the most severe condition of a perfectly catalytic wall in the vicinity of the nozzle throat, the heat transfer associated with the complete recombination at the wall is only 5% of the total heat transfer at the throat.

6. Specific impulse losses for the H₂-O₂ system computed by means of the one-dimensional kinetic machine program for nozzles with varying throat configurations amounted to from 2.5% to 4.3% of the ideal equilibrium impulse at an area ratio of 400:1. The assumed chamber pressure was 60 psia and the thrust level was 150 pounds. Investigations indicated nozzle throat contour changes do not appear to provide significant effects on performance.

7. No noticeable difference in nozzle specific impulse was observed between the results of kinetic calculations for H_2-O_2 combustion efficiencies of 98% and 100%. These efficiencies are not sufficiently different, however, to conclude that incomplete combustion does not affect nozzle performance.

8. Limited calculations employing the one-dimensional kinetic machine program indicate that there is no obvious scaling parameter which can be used to predict the exact performance of geometrically similar nozzles under nonequilibrium flow conditions. Additional investigations are felt to be necessary in order to determine a suitable scaling criterion.

9. The two-dimensional/axisymmetric machine programs for including the reaction kinetics in a method of characteristics construction have been completed under Task II. The "performance deck" has been run repeatedly in connection with the N_2O_4 system studied under Task III of this contract. Good agreement was obtained between predicted and measured reactant compositions for a two-dimensional test nozzle in which the recombination of NO_2 to form N_2O_4 was followed. It is concluded from this agreement that the calculation procedures employed in the two-dimensional finite kinetics machine program provide results representative of the supersonic flow field.

10. An optimum nozzle map for H_2-O_2 has been constructed utilizing the two-dimensional/axisymmetric design deck.

INTRODUCTION

Design of rocket exhaust nozzles to provide maximum expansion efficiency requires accurate methods for evaluating nonequilibrium flow processes and the effects of nozzle contour and size on such processes. The nonequilibrium processes which are of significance (depending on the propellant combination and operating conditions) include chemical recombination lags, thermodynamic relaxation lags, condensation lags, and velocity and thermal lags associated with two-phase flow. An additional problem which is related to nozzle flows involves the effect of the kinetics of recombination on heat transfer to the nozzle wall with nonequilibrium boundary layers.

Previous investigations (e.g., Refs. 1-4) of nonequilibrium flow processes have been concerned primarily with techniques for determining chemical recombination lags in one-dimensional flow processes. A technique common to many early investigations involved only simplified analyses of single reaction systems as in the method developed by Bray (Ref. 1).

The other nonequilibrium processes are usually considered to be of lesser importance than recombination lags. Special situations do occur, however, when the dominating nonequilibrium process is not the chemical recombination lag as, for example, two-phase flow losses. Recent studies of two-phase flow phenomena have been reported (Ref. 5); however, calculations of the relative importance of two-phase flow losses in the performance of particular propellants is generally lacking. Similarly, the effect of vibrational relaxation of the combustion products during expansion has not been generally considered in rocket nozzle calculations, although criteria for determining vibrational relaxation have been discussed in the literature (Refs. 6, 7).

In order to understand and optimize techniques for predicting the performance of exhaust nozzles and to provide information on the relative effects of the various nonequilibrium process for selected propellant combinations, a theoretical and experimental investigation was undertaken at the United Aircraft Corporation under the sponsorship of the National Aeronautics and Space Administration. This investigation was divided into three main Tasks and was directed towards: the determination of the relative effects of the various nonequilibrium processes by exploring order-of-magnitude calculations based on data available in the literature; the modification of a nozzle optimization procedure based on the method of characteristics, which has already been developed by United Aircraft Corporation, to allow inclusion of

B910056-12

finite reaction rates for multicomponent systems; and the experimental measurement of axial and radial concentrations in a two-dimensional test nozzle to check the analytical procedures based on the method of characteristics with finite reaction rates.

TASK I - RELATIVE IMPORTANCE OF EQUILIBRATION PROCESSES

The objective of this task was to determine for selected propellant combinations the relative effects of the various equilibration processes in high expansion ratio nozzles. The large number of processes and systems investigated in Task I limited the analysis to order-of-magnitude calculations which could be performed within the scope of this program. Although several of the nonequilibrium processes occur simultaneously for the propellants under study, the investigations leading to order-of-magnitude results assumed no interaction between the various processes so each process could be investigated at a prescribed temperature-pressure condition such as exists at local equilibrium.

The propellants considered were:

1. Hydrogen-Oxygen ($H_2 - O_2$)
2. Hydrogen-Fluorine ($H_2 - F_2$)
3. Diborane-Oxygen fluoride ($B_2H_6 - OF_2$)
4. Hydrazine-Nitrogen tetroxide ($N_2H_4 - N_2O_4$)
5. Beryllium-Hydrogen-Oxygen ($Be - H_2 - O_2$)
6. Hexane-Oxygen fluoride ($C_6H_{14} - OF_2$)

The combustion products of the above propellant combinations were considered for recombination and thermodynamic nonequilibrium at varying initial pressure and area ratio. The $Be - O_2 - H_2$ system was studied for velocity and thermal lags owing to high weight fractions of BeO , with pressure and particle size as parameters and thrust level and area ratio as variables. The combustion products of $B_2H_6 - OF_2$ propellant combination were considered for probable formation of condensable (B_2O_3) early in the expansion process which could possibly detract from the potential performance capabilities. Exact calculations were performed for the recombination of $H_2 - O_2$ propellant system in lieu of the order-of-magnitude calculations. The results are presented in a later section (TASK II). The $H_2 - O_2$ system was also considered for the effect of chemical nonequilibrium in the nozzle boundary layer on heat transfer to the nozzle wall.

The thrust levels for which the investigations of the various equilibration processes were performed were 5000 lbs at 60 psia chamber pressure, and 200,000 lbs at 1000 psia chamber pressure.

Chemical Recombination

It is well known that if a fuel is burned a large proportion of the chemical energy released may be used to dissociate chemical species into atomic species and radicals. If the combustion products are expanded through a supersonic nozzle, the chemical energy absorbed in dissociating the combustion products is not available for conversion to kinetic energy unless the absorbed energy is first made available to the gas mixture through recombination of the dissociated species. Therefore, the performance of convergent-divergent nozzles through which highly dissociated gases are accelerated depends greatly on the extent to which these gases are chemically recombined during the expansion process.

Significant losses caused by reaction and recombination lags are to be expected only when both of the following conditions exist:

- A. The chemical relaxation time is of the same order as, or longer than the flow time.
- B. The amount of enthalpy involved in the departure from equilibrium is a significant fraction of the total enthalpy change through the nozzle.

In general, high temperature gases undergoing expansion in a supersonic nozzle will never be in true chemical equilibrium. However, if the elementary chemical reactions in the system are able to proceed at a rate much greater than the rate composition change required to satisfy the local equilibrium constant, the system will be very close to true equilibrium. Calculations of the properties of an equilibrium flow involve the simultaneous solution of the equations of motion and chemical equilibrium for the system. Such solutions are well known and may be obtained easily by the use of computer techniques even for systems with complex chemistry.

It is not possible under all flow conditions for the elementary reactions to proceed at a rate fast enough to keep the flow in equilibrium. The reaction rates are exponential functions of density and temperature. Hence, as the flow expands through the nozzle, the reaction rates fall rapidly. If the reactions are only able to proceed at a rate much slower than the rate required to keep the system in equilibrium, the composition of the system will hardly change during the flow time. In this case the flow is said to be frozen.

Between the equilibrium and frozen flow limits there will be a region of increasing departure from equilibrium. An exact analysis of this transition region

must consider not only the equations of motion and chemical equilibrium but also the kinetic equations describing the rates of chemical reactions which are taking place. This complex system of equations does not permit a simple analytic solution and, in general, numerical methods together with high speed digital computers are required. Numerical solutions have been obtained for the nonequilibrium flow of air (Refs. 1 and 2) and hydrogen air combustion products (Ref. 3). For the propellants under consideration in this study, the exact analysis of the complex chemistry of the reaction mechanism would require extensive time and machine computations. The time and costs for such computations could not be justified within the scope of this investigation. Therefore, the study was limited to order-of-magnitude calculations for the region of increasing departure from equilibrium.

Because the reaction rates are very sensitive to changes in density and temperature, it is reasonable to expect that the transition from equilibrium to frozen flow may take place very quickly. If only small fractional changes in composition, density, temperature and velocity occur in the transition region, an approximation would be to treat the problem in the following manner. The flow is taken to be in complete equilibrium up to some station in the nozzle, the freezing point, whose location will be determined. Beyond the freezing point the flow is considered to be completely frozen; i.e., no further composition change takes place. The validity of this approximation, together with a method of locating the freezing point in the flow, is discussed in Appendix I. A brief description of the sudden freezing approximation is presented below.

Sudden Freezing Approximation

The idea that the transition from equilibrium to frozen flow occurs within a small region in the nozzle was originally discussed by Bray (Ref. 2), who constructed an approximate solution based on the assumption that freezing occurs instantaneously at a particular point.

In the equilibrium region the net rate of an elementary reaction is equal to the rate required to keep the reaction in equilibrium, R_F , but is much smaller than either of the forward, r_F , or reverse rates of reaction. That is, (c.f. Eq I-(12) of Appendix I)

$$R_F \ll r_F \quad (1)$$

When the flow has frozen, however, both the forward and reverse rates of reaction are much smaller than the rate, R_F , required to keep the flow in equilibrium (c.f. Eq. I-(13), Appendix I)

$$R_F \gg r_F \quad (2)$$

Somewhere in the freezing region, therefore, R_F and r_F must be of the same order of magnitude. It is assumed that at the freezing point

$$R_F = \kappa r_F \quad (3)$$

where κ is a constant of order unity. Since up to the freezing point the flow is in equilibrium, r_F may be evaluated at equilibrium conditions and the freezing point equation becomes

$$R_F = \kappa (r_F)_{eq} \quad (4)$$

where the subscript eq denotes equilibrium. Bray found that the value $\kappa = 1$ gave satisfactory agreement between the sudden freezing approximation and exact numerical solutions to the flow of partially dissociated air under a wide range of conditions (Ref. 1). The exact and approximate solutions were found to agree very closely in the regions where the flow was near equilibrium or frozen while small differences were observed in the transition region. The sudden freezing calculations were not critically dependent on the value chosen for the constant, κ . A comparison by Lordi (Ref. 8) for oxygen and hydrogen nozzle flows also shows excellent agreement between the exact and approximate solutions with $\kappa = 1$.

A sudden freezing approximation solution may be readily obtained for the flow of a partially dissociated diatomic gas or other system in which only one chemical reaction involves an appreciable amount of energy. When the combustion products of a typical rocket-propellant system are expanded through a nozzle, several chemical reactions must take place in order to maintain chemical equilibrium. In general, more than one of these reactions may involve a significant fraction of the total enthalpy change through the nozzle. Usually only two or three over-all reactions need be considered, but these in turn will each consist of several elementary steps and may be coupled together. Each system must be analyzed individually as there are no satisfactory general methods.

If sufficient information is available for a detailed analysis of the chemistry, it is frequently found that a major portion of the chemical energy release in the flow is controlled by one or two elementary reactions. When there is only one controlling reaction, or when all the controlling reactions have nearly the same freezing point it is possible to apply the sudden freezing method directly. When the freezing points of the controlling reactions are widely separated, the sudden freezing method may be used to establish limits on the flow variables.

An exact numerical solution for the nozzle flow of a high-temperature gas containing CO , CO_2 , H_2 , H , H_2O , and OH has been obtained by Westenberg and Favin (Ref. 4). It was found that the three-body recombination of H and OH is the rate-limiting

process which controls the significant portion of the chemical energy release. The sudden freezing approximation could, therefore, be applied to this system, and was found to give good agreement with the numerical solution.

Several systems involving complex chemistry were studied in this program and are discussed below. In all of the systems for which kinetic data were available or could be estimated, it was possible to find a single rate controlling reaction and apply the sudden freezing method.

Performance Calculations

H₂-F₂ Propellant System

The loss in vacuum I_{sp} resulting from chemical nonequilibrium in the nozzle was calculated for the H₂-F₂ system using the sudden freezing approximation. The calculations were done for the equilibrium optimum mixture ratio, O/F = 15.0, and for chamber pressures of 1000 and 60 psia. The nozzle shape was typical, consisting of a circular throat contour with radius of curvature equal to the throat diameter, joined by a tangent cone with a 15 degree half-angle. The throat diameters and corresponding thrust levels used in the calculation at each pressure level are shown below

Thrust Levels and Throat Diameters Used in Calculations

<u>Chamber Pressure, psia</u>	<u>Throat Diameter, in.</u>	<u>Approximate Thrust Level, lb</u>
1000	11	200,000
60.0	7	5,000

Calculated values of vacuum I_{sp} (labeled kinetic) are shown in Figures 1 and 2 for the two cases along with the equilibrium and frozen values. As shown, the losses are small for the high pressure case, but become significant at the lower pressure.

For the H₂-F₂ system it was possible to find a single rate-determining reaction which controlled all of the chemical energy release in the flow. The entire composition shift taking place in the nozzle is due to the recombination of H and F atoms to form both HF and H₂. An analysis of the chemical kinetics of this system

revealed that in both cases the predominant mechanism for the formation of HF was the direct three-body recombination



while H_2 was formed primarily from the two-step process



It was found that the rate of Reaction (6) was very much greater than that of Reaction (5) so both processes are controlled by Reaction (5). The freezing point, therefore, was taken as that point in the flow where the forward rate of Reaction (5) was just large enough to satisfy both the equilibrium increase in HF plus the amount of HF required for conversion to H_2 by Reaction (6).

All of the elementary reactions considered in the kinetic analysis together with the rate constants are shown in Table 1. Experimental data were available only for the three-body recombination of H atoms. Rate constants for the other reactions shown in Table 1 were estimated from experimental data on $\text{H}_2\text{-Cl}_2$, $\text{H}_2\text{-Br}_2$ and $\text{H}_2\text{-I}_2$ systems (Refs. 10, 11, 12) using classical reaction rate theory. All thermodynamic data were taken from the JANAF tables (Ref. 13).

$\text{N}_2\text{H}_4\text{-N}_2\text{O}_4$ Propellant System

The loss in vacuum I_{sp} resulting from chemical nonequilibrium in the nozzle was calculated for the $\text{N}_2\text{H}_4\text{-N}_2\text{O}_4$ system using the sudden freezing approximation. The calculations were done for the equilibrium optimum mixture ratio, $\text{O/F} = 1.40$, and for chamber pressures of 1000 and 60 psia. The assumed nozzle shape, the throat diameters used at each pressure level, and the corresponding thrust levels were identical to those used for the $\text{H}_2\text{-F}_2$ system.

Calculated values of vacuum I_{sp} (labeled kinetic) are shown in Figs. 3 and 4 for this system at the two chamber pressures. As in the case of the $\text{H}_2\text{-F}_2$ system, the losses are small at the high chamber pressure but become significant at the lower pressure.

For the $\text{N}_2\text{H}_4\text{-N}_2\text{O}_4$ system it was possible to find a single rate-determining reaction which controlled the major portion of the chemical energy release in the flow. The entire composition shift in the nozzle is caused by the conversion

of NO to N_2 , O, and O_2 together with the formation of H_2O from the available OH, O, O_2 , H, and some of the excess H_2 . A thermo-chemical analysis of this situation showed that the conversion of NO did not contribute a large amount of chemical energy directly to the flow, and was not a significant source of O and O_2 for the subsequent formation of H_2O . It was found that under the conditions existing in the nozzle for both chamber pressures that the formation of H_2O was controlled by the three-body recombination of H and OH given by



The freezing point was located by equating the forward rate of this reaction to the equilibrium rate of formation of H_2O in the system.

All of the elementary reactions considered in the kinetic analysis together with the selected rate data used in these calculations are shown in Table 2. All thermodynamic data were taken from the JANAF tables.

C₆H₁₄-OF₂ Propellant System

The loss in vacuum I_{sp} resulting from chemical nonequilibrium in the nozzle was calculated for the C_6H_{14} -OF₂ system using the sudden freezing approximation. The calculations were done for the equilibrium optimum mixture ratio, O/F = 4.50, and for chamber pressures of 1000 and 60 psia. The assumed nozzle shape, the throat diameters used at each pressure and corresponding thrust levels were identical to those used for the H_2 -F₂ system.

Calculated values of vacuum I_{sp} (labeled kinetic) are shown in Figs. 5 and 6 for this system at the two chamber pressures. As for the two systems discussed previously, the losses are small at the high chamber pressure but become appreciable at the lower pressure.

The entire composition shift in the nozzle for the C_6H_{14} -OF₂ system is owing to the formation of HF from free fluorine atoms and hydrogen available as H, H_2 , OH, and H_2O , and the conversion of CO to CO_2 which uses all of the oxygen available as O_2 , O, OH, and H_2O . A thermochemical analysis showed that each of these two over-all reactions contributes about half of the total chemical energy release in the flow. From an analysis of the mechanism and kinetics of the chemical reactions taking place, it was determined that each of these over-all reactions was controlled by a separate rate-determining step. The conversion of CO to CO_2 was controlled by the reaction



and, as in the H_2-F_2 system, the series of reactions leading to the formation of HF was controlled by the three-body recombination



When the freezing points for both Reactions (8) and (9) were located, they were sufficiently close together to permit the use of a single freezing point to describe the flow.

The elementary reactions considered in the kinetic analysis of the $C_6H_{14}-OF_2$ system included those used for the two systems discussed previously, which are given in Tables 1 and 2. In addition, several reactions involving CO and CO_2 were considered. From a study of the work of Fenimore and Jones on hydrocarbon flames (Refs. 18 and 19) it was concluded that the only reaction of this type which was of importance in the present analysis was Reaction (8).



with forward rate constant

$$K_f = 3 \times 10^{12} \exp \left[-10/RT \right] \text{ cm}^3 \text{ mol}^{-1} \text{ sec}^{-1}$$

where the activation energy is given in Kcal/mol and T is in °K. All thermodynamic data were taken from the JANAF tables (Ref. 13).

$B_2H_6-OF_2$ Propellant System

A reliable calculation of the performance loss to be expected from chemical nonequilibrium effects in the $B_2H_6-OF_2$ system was not possible because of a lack of sufficient chemical kinetic data. From an analysis of the equilibrium solution, however, it is possible to deduce several reactions which are likely to be important in determining the performance losses. These reactions are probable subjects for future research.

Neglecting reactions of little significance, the composition shift taking place during the nozzle expansion of this system may be represented by the overall reactions shown in Table 3. The number of moles ΔN_i of each reaction which must take place in equilibrium flow between the chamber and $A/A^* = 400$ per 100 grams of mixture is shown, together with the heat of each reaction, ΔH_{r_i} . The chemical enthalpy which will be released in equilibrium flow by each of the reactions, $\Delta h_i = \Delta N_i \cdot \Delta H_{r_i}$, is also shown, along with the total chemical enthalpy change resulting from the equilibrium composition shift

$$\Delta h_{\text{total}} = \sum_{\text{reactions}} \Delta h_i \quad (10)$$

The quantity Δh_{total} is equal to the enthalpy which would be lost if the flow were frozen at the chamber composition.

The reactions shown in Table 3 fall naturally into three categories: those forming BF^*_3 , those forming BOF, and the direct recombination of atomic H. The major contributions to the total recombination enthalpy are from BOF forming reactions and the formation of H_2 . In order to locate the freezing point for this system, it is necessary to establish rate-determining steps in the series of elementary reactions leading to the formation of BOF and H_2 . Although enough is known about the recombination of H_2 to permit analysis, no information is available on any of the elementary reactions which are of importance in BOF formation. Elementary reactions may be postulated which are likely to be significant in the formation of BOF, such as the two-body processes



or the three-body recombinations



Satisfactory estimates of the rates of such reactions are not possible, because even definitive information on the structure of boron compounds such as BOF are lacking. Until further kinetic data are available it is not possible to make a valid estimate of the chemical nonequilibrium losses in this system.

Thermodynamic Relaxation

The energy stored in the excited states of a system is redistributed during the thermodynamic relaxation processes at some finite rate until the population of the energy levels is at equilibrium for the environmental temperature and pressure. If equilibrium of the excited levels is not attained at each of the pressure and temperature conditions established during nozzle expansion, the specific heat or sensible enthalpy of the gases is not correctly defined by the equilibrium temperature condition. The loss in sensible enthalpy, as a result of energy stored in excited states, cannot be converted into directed kinetic energy and rocket thrust.

During the progress of expansion in the nozzle, molecular collisions must occur in order to redistribute the energy of excited molecules. Typically, liquid propellant combustion might yield products at 2500° K and 20 atm pressure with nozzle residence times of the order of 1 millisecond. Chemical propellants do not yield temperatures and pressures in thrust chambers which allow electronic excitation, but translational, rotational and vibrational degrees of freedom can all be excited. Translational equilibrium is produced within several molecular collisions, and rotational equilibrium within about five collisions. Times for such equilibration correspond to 10^{-9} to 10^{-11} seconds, and these relaxations may be considered instantaneous. On the other hand, vibrational relaxation times may be orders of magnitude larger (Ref. 20) and the relaxation time may be of significance. In view of the shortness of relaxation times relative to chemical reaction times, it is frequently assumed (Refs. 21, 22, and 23) that vibrational equilibrium is obtained; however, this may not be the case for all conditions and propellants, especially in very high expansion nozzles.

Theoretical treatments of the relaxation process have been developed (Refs. 20, 24, 25, and 26), but these require detailed quantum-mechanical steps. The problem is further complicated when thermodynamic relaxation and chemical kinetics occur simultaneously in exhaust nozzles.

One of the first attempts at coupling the chemical and vibrational processes was that of Hammerling et al (Ref. 27) who sought to determine the change in dissociation rates behind a normal shock wave due to a departure from vibrational equilibrium in the dissociating specie. The method of analysis employed was based on the assumptions (1) that dissociation can proceed with equal probability from any vibrational level and (2) that throughout the relaxation process, the fraction of molecules in any particular vibrational level remains in a Boltzmann distribution about the local vibrational temperature. Using this model, the rate of dissociation from any particular level is proportional to the product of the population in that level and the rate of collision with particles having sufficient energy to cause dissociation from that level. Thus any lag in vibrational equilibration would have the effect of reducing the rate of dissociation because of the lack of highly excited (i.e., easily dissociable) molecules.

More recently, Treanor and Marrone (Refs. 28 and 29) have modified the above treatment in two important ways. In Ref. 28, an accounting was made of the reduction in the average vibrational energy of the molecules which accompanies dissociation (i.e., loss of the most energetic vibrators). In Ref. 29, an investigation was made of the possibility that dissociation proceeds preferentially from the higher vibrational levels of the molecule.

Each of the above treatments demonstrated that the rate of dissociation was appreciably reduced by the lack of vibrational energy equilibration. However, none of these treatments is directly applicable to coupled vibrational relaxation and recombination such as would occur in nozzle flows. While the general methods of analysis are applicable, there exists some serious question as to which vibrational levels would be populated first upon recombination and how vibrational de-excitation occurs from these levels. Further, the degree of uncertainty in both the measurement of the recombination rates and the vibrational relaxation times hardly justifies incorporation of the coupled mechanisms into the treatment of nonequilibrium nozzle flows at this time.

A less sophisticated approach would be to assume no interdependence between the specific reaction rates and vibrational relaxation. It would then be possible to solve the reaction rate equations which describe a recombination scheme simultaneously with the uncoupled vibrational relaxation of the specified radicals or molecules. This, however, is still a costly approximation since extensive IBM computations would be required.

Alternative useful relationships have been developed which correlate well with experimental results (Refs. 6, 7, 30, and 31). Significant losses in nozzles caused by vibrational relaxation lags are to be expected only when both of the following conditions exist:

1. The vibrational relaxation time at a pressure and temperature condition is of the same order of magnitude as or longer than the actual residence time at the same conditions.
2. The sensible enthalpy involved in the departure from equilibrium is a significant fraction of the total enthalpy change throughout the nozzle; i.e., the composition of species which lag in thermodynamic relaxation is large.

Vibrational relaxation effects in rocket nozzles are secondary to dissociation effects. Consequently, for order of magnitude analysis refined calculations of vibrational relaxation processes are not warranted unless they are coupled to the dissociation and recombination effects.

A technique similar to the Bray "freezing criterion" for chemical recombination (Ref. 1) is assumed satisfactory to establish the significance of the combustion products species in nonequilibrium vibrational relaxation. An outline of the "freezing point" analysis for vibrational relaxation appears in Refs. 6 and 7 and is presented in Appendix II. The criterion was developed to establish when departures from molecular vibrational equilibrium in the flow are likely to occur. The usefulness of the

criterion is based on the agreement between vibrational temperature distributions determined from exact calculations in a nonreactive gas.

The criterion takes the form

$$Q = \left[(T/\tau) / v \frac{dT}{d[A/A^*]} \right] \left(\frac{2 \tan 15}{r_t} \right) \left(1 + \frac{\tan 15}{r_t} x \right) \quad (15)$$

for a steady flow and expansion in a divergent nozzle with a 15 degree half-angle. The value, Q , must be significantly greater than 1 for vibrational equilibrium to occur. It has been suggested that Q equal 20 satisfied vibrational equilibrium for air expansion in hypersonic tunnels (Ref. 7). When Q is significantly less than 1 the vibrational relaxation can be considered frozen. The applicability of the "freezing point" techniques is dependent on the availability of a temperature-pressure profile for a specific propellant and nozzle such as may be obtained from equilibrium or kinetic calculations as well as vibrational relaxation data such as exists in the literature (Refs. 32, 33, 34, 35, 36, and 37). When vibrational relaxation data are lacking over the temperature range of interest application of the relationship $\log \tau$ vs $T^{-1/3}$ is a straight line is assumed (Ref. 8).

The above criterion was utilized with nozzle equilibrium calculations for each of the propellants being considered in Task I. The gradient, $dT/d(A/A^*)$, was obtained by graphical differentiation of equilibrium temperature vs. area ratio curves for each propellant and chamber condition. The throat radius, r_t , was sized at 5000 lbs thrust, 60 psia chamber pressure and 200,000 lbs thrust, 1000 psi chamber pressure for each propellant combination. The values for relaxation times of the individual molecules were obtained from the literature, and corrected for temperatures and pressure when it was necessary to do so. However, the values for relaxation times of the individual molecules were not corrected for third-body efficiencies, impurities, and multicomponent mixtures. In general, evidence exists that the relaxation times of diatomic molecules can be reduced considerably by the presence of third bodies especially the presence of water (Ref. 35). For the calculations performed in this study, the point of view was taken that as long as vibrational relaxation effects are secondary in terms of energy losses relative to chemical recombination losses, the most conservative values of relaxation time would be used. If the use of conservative values indicates that freezing of the vibrational modes is negligible, then any corrections for third bodies or impurities would only make the conclusion more optimistic. A case in point is the O_2 molecule whose relaxation time with no impurities can be reduced by a factor of 10^3 when water is present. See Table IV of Ref. 37.

Performance Calculations

The results of the calculations performed are listed below for each propellant combination studied.

N₂H₄-N₂O₄ Propellant System

The combustion products of the N₂H₄-N₂O₄ propellant system at the equilibrium optimum O/F ratio which have been considered for possible vibrational relaxation lags are N₂, O₂ and H₂O. The results tabulated below indicate the estimated freezing point area ratios (downstream of the throat) for the two cases considered.

N₂H₄-N₂O₄ System

$$O/F = 1.4$$

Chamber Pressure psia	Thrust Level lbs	Throat Radius inches	Vibrational Freezing Area Ratio		
			N ₂	O ₂	H ₂ O
60	5,000	3.58	2	10	300
1000	200,000	5.60	10	50	300

For this system the N₂ molecule is the only one of significance because of its high concentration and its possible freezing very near to the throat. The O₂ molecule, although it freezes relatively early in the divergent section, is present in such low concentrations that it may be neglected. The H₂O molecule does not have any tendency to freeze in this system even at area ratio of 300.

It can be seen that the vibrational relaxation freezing point is very sensitive to pressure level. This is to be expected since the number of collisions that a given molecule undergoes is directly proportional to the density of the gases and consequently the relaxation times are reduced proportionately. The data used for the relaxation times of the individual molecules N₂, O₂ and H₂O were obtained from Refs. 36 and 37 respectively and assumed no impurities or third body corrections.

C₆H₁₄-OF₂ Propellant System

The combustion products of the C₆H₁₄-OF₂ propellant system which have been considered for possible vibrational relaxation lags are H₂O, O₂, CO₂, CO and HF. The estimated freezing point area ratios (downstream of the throat) are given below.

C₆H₁₄-OF₂ System

O/F = 4.75 @ 60 psia

4.5 @ 1000 psia

Chamber Pressure psia	Thrust Level lbs	Throat Radius inches	Vibrational Freezing Area Ratio				
			H ₂ O	O ₂	CO ₂	CO	HF
60	5,000	3.56	> 350	20	> 300	6-10	> 100
1000	200,000	5.57	> 350	85	> 300	20	> 100

For this system the CO and HF molecules are the significant molecules because of the large concentrations relative to H₂O, O₂ and CO₂. It is felt that the freezing areas presented may be conservative because no attempt was made to correct the relaxation times of the species for multicomponent systems. The presence of other species such as H₂O tend to reduce the relaxation times considerably. Because of the lack of data for both CO and HF, especially the latter for which no data were available, little absolute significance can be placed on the freezing point area ratio except to deduce some trends. The vibrational freezing areas occur far enough downstream of the throat for most species so the energy stored in vibrational states beyond this point may be neglected relative to energy lost as a result of freezing the chemical species.

It should be noted that relaxation times for CO were not available over the entire range of interest. The data were extended by utilizing the relationship of log time vs. $T^{-1/3}$ (Ref. 32). The relaxation times for HF were assumed to be of the same order of magnitude as Cl₂ because data for F₂ or HF are not available. The data used for the relaxation times of the molecules H₂O, O₂, CO₂, CO and HF/Cl₂ were obtained from Refs. 32, 36 and 37.

H₂-O₂ Propellant System

The combustion products of the H₂-O₂ system at the equilibrium optimum O/F ratio which have been considered for possible vibrational relaxation lags are H₂O and O₂. Presented below are the estimated freezing point area ratios (downstream of the throat) for the two cases considered.

H_2-O_2 System

O/F = 5 @ 60 psia

= 6 @ 1000 psia

Chamber Pressure psia	Thrust Level lbs	Throat Radius inches	Vibrational Freezing Area Ratios	
			H_2O	O_2
60	5,000	3.6	> 400	10
1000	200,000	5.54	> 400	75

For this system the H_2O molecule is the only one of significance because of its high concentration throughout the nozzle and it showed no tendency to freeze. The concentrations of O_2 and OH are so extremely small at near optimum O/F ratios that if freezing of the vibrational states occurred so little energy would be involved that the vibrational lags may be neglected. Although H_2 is present in significant concentrations, no relaxation data are available. It is expected, however, that the vibrational relaxation time is considerably faster than that of O_2 and therefore should not freeze readily (Refs. 38, 39, and 40). As in previous systems the freezing area is very sensitive to temperature and pressure levels because of the large variations of relaxation times. The data used for relaxation times of O_2 and H_2O were obtained from Refs. 36 and 37 respectively.

 H_2-Be-O_2 Propellant System

The combustion products of H_2-Be-O_2 propellant system at equilibrium O/F ratio which should be considered for possible vibrational lags are BeO and H_2 . However, no vibrational relaxation data are available for these molecules. Because of the lack of data, the calculations were performed utilizing the relaxation times for O_2 and H_2O since O_2 and H_2O represent molecules whose vibrational relaxation characteristics span the range from slow to rapid vibrational relaxation rates. It is assumed that as long as O_2 and H_2O do not freeze readily under the conditions of pressure and temperature encountered in the nozzle for H_2-Be-O_2 , then H_2 and BeO should also not depart significantly from equilibrium. This should be correct at least for the H_2 molecule since its relaxation time is considerably less than that of O_2 (Refs. 38, 39 and 40). The estimated freezing area ratios (downstream of the throat) for the two cases considered are given below.

H₂-Be-O₂ System

$$O/F = 0.29$$

Chamber Pressure psia	Thrust Level lbs	Throat Radius inches	Vibrational Freezing Area Ratio	
			O ₂	H ₂ O
60	5,000	3.5	1.0	> 300
1000	200,000	5.46	50	> 300

It is readily seen that the conservative use of the relaxation time for O₂ for the pressure and temperature conditions encountered in the nozzle of the H₂-Be-O₂ propellant combination leads to vibrational freezing areas well beyond the throat. Since the relaxation time of H₂ is expected to be considerably less than that of O₂ (Refs. 38, 39 and 40), it is believed that the tendency to freeze should also occur considerably downstream of the throat. If this is correct the vibrational nonequilibrium energy losses should be negligible relative to the possible losses as a result of chemical recombination lags.

H₂-F₂ Propellant System

The combustion products of H₂-F₂ at equilibrium O/F ratio which should be considered for possible vibrational lags are H₂ and HF. However, no vibrational relaxation times are available for these molecules. Because of the lack of data the calculations were performed utilizing the relaxation times for Cl₂. It is assumed that the relaxation time of H₂ is at least faster than that of Cl₂, and the relaxation time of HF is of the same order of magnitude as that of Cl₂. The estimated freezing area ratio downstream of the throat for the Cl₂ molecule (under the conditions of pressures and temperatures produced by the H₂-F₂ propellant system) are presented below.

H₂-F₂ System

$$O/F = 15$$

Chamber Pressure psia	Thrust Level lbs	Throat Radius inches	Vibrational Freezing Area Ratio	
			F ₂ /Cl ₂	
60	5,000	3.56	150	

Because the area ratio at which the vibrational freezing of Cl_2 occurs is considerably downstream of the throat, the nonequilibrium vibrational relaxation losses should be negligible for the combustion products of H_2 and F_2 systems. Calculations were not performed for the high pressure and thrust level conditions because it is obvious that nonequilibrium vibrational processes are less significant than at low pressure and thrust level.

The data used for the relaxation times of the Cl_2 molecule were obtained from Ref. 36.

$\text{B}_2\text{H}_6\text{-OF}_2$ Propellant System

Very little data on vibrational relaxation times are available for the combustion products of the $\text{B}_2\text{H}_6\text{-OF}_2$. The molecules that make up the major combustion products include boron oxides and fluorides along with small concentrations of many combinations of hydrogen, oxygen and fluorine. Because of the lack of data for the major constituents and previous estimates presented for the vibrational relaxation process of the minor constituents O_2 , H_2O , F_2 and HF (the latter two approximated through relaxation times of Cl_2) it was felt that calculations for this system were not warranted. From previous calculations it can be safely concluded that H_2O , F_2 and HF would not freeze readily. Oxygen probably would tend to freeze at an area ratio near 10 for low chamber pressures (60 psia). However, its concentrations are small so the energy losses would be negligible.

Two-Phase Flow in Rocket Nozzles

The use of metal fuels such as aluminum and beryllium results in the formation of small metal oxide particles upon combustion. Thermal energy of the particle phase is converted to directed kinetic energy by virtue of heat and momentum exchange with the gas phase. As the gas-particle mixture expands through a nozzle, heat transferred from the particles causes the gas to accelerate and the gas, in turn, imparts kinetic energy to the particles by virtue of drag forces. If the particles lag the gas in temperature and velocity these transfer processes are irreversible and result in decreased nozzle efficiency. The percentage decrease in specific impulse from the two-phase equilibrium flow value increases with both the magnitude of the particle lags and with the condensed phase mass fraction.

The degree of thermal lag is determined by the rate of decrease in particle temperature due to heat transfer compared to the temperature gradients in the gas flow. Similarly, the velocity lag depends on the particle acceleration due to drag forces compared to the velocity gradients in the gas flow. Heat transfer rates and drag forces depend on the physical properties of the gas and the particles, while

the gas temperature and velocity gradients are determined largely by the nozzle size and shape. For example, it has been shown (Ref. 5) that the particle-to-gas velocity ratio, $\phi = u_p/u_g$, at the throat of a conventional nozzle is dependent on a characteristic Reynolds number for the particle, which determines the drag coefficient, and the parameter

$$\frac{(\gamma+1) \mu \sqrt{R y_t}}{a_{g c} \rho_p r_p^2}$$

This latter parameter is the ratio of two time constants:

$$\frac{\sqrt{R y_t}}{a_{g c}}$$

which represents the gas residence time, and

$$\frac{\rho_p r_p^2}{\mu}$$

which represents the particle residence time. Thus, an increase in throat radius of curvature, throat diameter, or gas molecular weight increases the gas residence time and promotes velocity equilibrium; while an increase in particle density or radius or a decrease in gas viscosity increases the particle residence time and promotes greater velocity lag.

One-Dimensional Two-Phase Flow Calculations

The one-dimensional motion of two-phase flow in a rocket nozzle has been analyzed by many authors (Refs. 5, 41-45). Although machine computation is required to find the flow throughout an arbitrary nozzle shape, it has been possible to find a relatively simple analytic description for the case in which particle velocity and temperature lags are assumed constant. Calculations with particle weight fractions up to 50 percent show that the assumption of constant lag from the chamber gives accurate predictions of the flow throughout the throat region of most conventional nozzles (Refs. 5, 41, 44). This is a result of the lags being essentially constant near the throat, where a major portion of the conversion from thermal to kinetic energy occurs. Thus, the c^* efficiency, which is influenced by particle lags upstream of the sonic line, can be readily determined analytically for a wide variety of input conditions.

Specific impulse is related to c^* by the relation

$$I_{sp} = c^* C_F \quad (16)$$

where

$$c^* = \frac{P_c A_t}{\dot{m}_g + \dot{m}_p}$$

and

$$C_F = \frac{F}{P_c A_t}$$

Examination of numerous numerical calculations for aluminized propellant systems indicates that the decrease in c^* caused by particle lags generally constitutes the major portion of the loss in specific impulse. That is, for given chamber conditions, the thrust is less sensitive to particle lags than is the mass flow rate.

In view of the above results for aluminized propellants, it is expected that a good first order estimate of performance losses in the Be-O₂-H₂ system can be obtained analytically from the prediction of constant lag formula for the decrease in c^* due to particle lags.

The constant lag equations used to calculate c^* data are given in Appendix III for the Be-O₂-H₂ system.

Performance Calculations for the Be-O₂-H₂ System

The following summarizes the results of calculations for the performance losses due to particle lag in the Be-O₂-H₂ system. All calculations are for the combination 27.9 percent Be, 49.6 percent O₂, and 22.5 percent H₂ by weight, giving essentially 77.5 percent liquid BeO particles and 22.5 percent partially dissociated H₂ after combustion. This combination gives optimum specific impulse over a wide range of area ratios for two-phase and chemical equilibrium. The bulk of the calculations consist of the decrease in c^* from the two-phase equilibrium value, as a function of particle radius and thrust level or nozzle size. Since lack of information about the particle radius of BeO prevents definitive performance estimates at this time, these calculations of c^* are based on the constant particle lag approximation for which analytic solutions are available. As discussed previously, it is expected that these calculations should yield first order estimates of c^* efficiency and that the losses in both c^* and I_{sp} should be comparable. These predictions were verified by numerically computing c^* and I_{sp} for one case.

The results for c^* losses are presented in Figs. 7 and 8 for chamber pressures of 1000 and 60 psia, respectively. These curves show the relative decrease in c^* from the two-phase equilibrium value as a function of Ry_t , or thrust level, with

particle radius as a parameter. The variable Ry_t , upon which velocity gradients depend, incorporates the influence of both nozzle size and throat configuration. The thrust-level scale is derived from Ry_t for the typical values $R/y_t = 2$ and $C_F = 2$.

The performance losses are large for the relatively low thrust levels and show a strong dependence on particle radius. As thrust level and nozzle size increase, the losses decrease and particle size has less effect. For a given nozzle size (Ry_t) and particle radius performance losses are increased by lowering the chamber pressure. This reflects the lower particle drag and heat transfer due to the increasing importance of rarefied flow effects as the chamber pressure is decreased. With $P_c = 60$ psia the gas mean free path at the nozzle throat is approximately 0.4 microns.

Potential losses in performance for the Be-O₂-H₂ system under consideration are intensified by the low molecular weight and viscosity of H₂, as well as by the high weight fraction of BeO particles.* Unfortunately, the particle radius for BeO has not yet been determined and performance decrements caused by particle lag can only be determined within a range corresponding to the uncertainty in particle size. On the basis of Al₂O₃ particle sizes (Ref. 46) one would expect BeO to lie somewhere in the range from 0.5 to 5.0 microns in diameter, depending on chamber pressure.

Chamber pressure influences lags in two ways. First, a decrease in chamber pressure decreases Reynolds number and increases Knudsen number. Except for the continuum Stokes flow regime, both of these effects reduce particle drag and heat transfer and therefore promote greater lags. Secondly, based on the results for Al₂O₃ particle formation, particle size is expected to decrease with decreasing chamber pressure. This tends to reduce particle lags, and in the case of aluminized propellants appears to be the dominant effect (Ref. 41). Knowledge of the particle radius-chamber pressure variation for BeO is important in establishing definitive design criteria for space engine applications of the Be-O₂-H₂ propellant system.

*The theoretical equilibrium vacuum I_{sp} at infinite area ratio continually increases with the weight fraction of BeO formed. However, the equilibrium I_{sp} achieved with a given area-ratio exhibits a maximum with increasing weight fraction of BeO. This happens because of the opposing effects of an increasing total thermal energy per unit mass and a slower rate of conversion from thermal to kinetic energy as the particle weight fraction increases. For a wide range of practical area-ratios, equilibrium flow calculations indicate that the best I_{sp} is achieved with 77.5 per-cent BeO (Be and O₂).

The ultimate variation of performance with chamber pressure will, of course, depend on the variation of particle size with pressure. For Al_2O_3 the particle radius has been reported to vary from $2.4\ \mu$ at 1000 psia to $0.25\ \mu$ at 90 psia (Ref. 46), and performance for aluminized propellants theoretically increases with decreasing chamber pressure (Ref. 41). Although similar behavior would be expected in the $\text{Be-O}_2\text{-H}_2$ system, performance losses cannot be precisely estimated until after the particle size of BeO and its variation with pressure are determined.

A machine calculation was made to determine the loss in specific impulse as a function of area ratio for a nozzle having an exit cone half-angle of 22.9° , $R = 17.8$ cm, $y_t = 8.9$ cm, and a chamber pressure of 60 psia. The particle radius was $1.5\ \mu$. The relative decrease in vacuum specific impulse from the two-phase equilibrium value is presented as a function of area-ratio in Fig. 9. The loss in I_{sp} is approximately 14 percent, nearly independent of the exit area ratio. c^* was found to be 18 percent below the equilibrium value from this calculation. Thus, the losses in c^* and I_{sp} are comparable, as expected. Also, the constant lag prediction of a 15 percent loss in c^* for this case (Fig. 8) agrees reasonably well with the numerically calculated value of 18 percent.

The problem of numerically integrating for the two-phase flow throughout an arbitrary nozzle shape is complicated by two factors. First, the upstream starting velocity necessary to produce choked flow is not known a priori. If the chosen starting velocity is too low, the flow will remain subsonic throughout the nozzle while too high a value produces a physically impossible solution. Thus, it is necessary to iterate for the proper starting velocity by observing the character of the solution as a function of the assumed starting velocity.

The second difficulty arises because of the singular point which exists when the gas Mach number reaches unity. In practice the calculation for gas velocity becomes unstable near $M_g = 1$ and it is necessary to extend the velocity through the singular region based on the last computed stable slope. For moderate weight fractions, the region of calculational instability caused by the singular point is very narrow and negligible error is introduced by approximating the velocity with the above method. However, for the high particle weight fraction of the $\text{Be-O}_2\text{-H}_2$ system ($Z = 3.45$), the unstable region became so wide that the above method of forcing a stable velocity behavior was considerably in error. For the present purposes, this difficulty was overcome by modifying the nozzle shape to agree with an assumed velocity distribution.

Variations of gas Mach number, $\phi = u_p/u_g$ and $\theta = T_c - T_p / T_c - T_g$ are given in Fig. 10 for the above case. It is interesting to note that the particles are in free molecular flow throughout most of the exit cone. Thus, the low drag and heat transfer rates result in decreasing values for ϕ and θ as the gas expands to high area-ratios.

The preceding calculations demonstrate that at low thrust levels particle lag may cause appreciable performance losses, even for submicron particles. On the other hand, at very high thrust levels the losses become appreciable only for particle sizes larger than one micron.

Chemical nonequilibrium losses in the nozzle were not computed for the Be-O₂-H₂ system. Estimates of the magnitude of these losses show them to be of second order compared to the probable losses arising from particle lags. When further information on BeO particle size enables accurate performance predictions to be made, it may be desirable to compute the chemical nonequilibrium losses more exactly.

Condensation Losses

The presence of condensable species in the combustion products of propellants can introduce limitations to their performance capabilities. Of the propellant systems under study, it was concluded that the combustion products of B₂H₆-OF₂ propellant combination might produce condensables early in the expansion process to detract seriously from the potential performance capabilities.

Preliminary calculations based on chemical equilibrium expansion to area ratios equal to 500 indicated that at all stations the partial pressure of the B₂O₃ was less than the vapor pressure. This is shown in Figs. 11 and 12 for chamber pressures of 1000 psia and 60 psia. However, if it is assumed that the flow expansion is completely frozen from the outset, then it can be shown that the vapor pressure and partial pressure curves intersect at area ratios approximately equal to ten for the two cases presented in Figs. 11 and 12. The realistic situation is intermediate between the frozen and equilibrium results. Because the realistic situation would lead to either no condensation or possible small amounts of condensation considerably downstream of the throat, it was concluded that condensation of B₂O₃ in the B₂H₆-OF₂ propellant combination would not produce serious performance losses.

Nonequilibrium Boundary Layer Effects on Nozzle Heat Transfer

The viscous flow equations for the flow of a reacting gas mixture over a surface are complicated by the inclusion of finite reaction kinetics. The main differences between the reacting gas case and the classical boundary layer problem are: (1) the reacting gas is not homogeneous but is a mixture of atomic and molecular species whose composition varies from point to point in the boundary layer; and (2) the composition is not a function of the state variables alone (equilibrium flow) but due to gas phase recombination in the flow and catalytic recombination at the surface, is a function of both average transit times for a particle to pass through

the boundary layer and the number of particles striking the wall. The heat transfer rate to the surface is then composed of two parts: the usual viscous heat transfer due to molecular convection and the heat transfer due to recombination of the atomic species which diffuse towards the wall and recombine upon striking the wall. The total heat transfer is the sum of these two heat transfer rates.

Analytical solutions to the problem of nonequilibrium heat-transfer rates to a catalytic surface have been obtained for the case of the flow about a blunt body in the vicinity of the stagnation point (see, for example, Refs. 47 and 48) and for the case of laminar flow over a flat plate neglecting hypersonic interaction effects (Ref. 49). There are, however, no known solutions for the case of turbulent flow such as would be encountered in a rocket nozzle. An approximate method for extending the solutions of Refs. 48 and 49 to the case of a turbulent boundary layer is presented herein and is used to predict the heat transfer rates to the walls of a hypothetical nozzle configuration.

Nonequilibrium flow has two effects on the heat transfer rate: (1) the slope of the enthalpy profile through the boundary layer, and hence at the wall, is changed from its equilibrium composition value by the composition gradients which exist through the boundary layer; and (2) there is an additional heat transfer to the wall due to recombination of the atomic species upon striking the wall. It is then argued that for low atomic species concentrations in the free-stream, both of these effects would be necessarily small and that a reasonable value for the local heat transfer rate may be computed by assuming that the flow in the boundary layer is frozen at the free-stream composition and neglecting the effects of catalytic recombination at the surface. The concentrations of the various species of H_2/O_2 ($O/F=5$) combustion products in the free-stream of a hypothetical 5000 lb thrust configuration with a chamber pressure of 60 psia are presented in Fig. 13 as a function of distance from the nozzle throat for the case of equilibrium flow in the nozzle. It is seen from this reference that the atomic species concentrations in the free-stream are on the order of 1 percent or less at all points in the nozzle, thus satisfying the condition of low free-stream atomic species concentrations.

The heat transfer rate for frozen flow in the turbulent boundary layer may be computed from a modification of the laminar flow theory presented in Ref. 49. This method shows that for a frozen laminar flow, the heat transfer rate is proportional to the slope of the velocity profile at the wall. It is then argued that since the laminar sublayer is the controlling phenomena in turbulent skin-friction and heat transfer, a reasonable first approximation to the turbulent flow case may be obtained by rewriting the heat transfer rate in terms of the slope of the velocity profile at the wall and then replacing this slope with the slope of the turbulent profile. The values of the slope of the turbulent velocity profile may then be

determined from turbulent skin-friction data. This analysis is presented in APPENDIX IV where it is shown that for laminar frozen flow the convective heat transfer rate to the wall may be expressed as:

$$q_c = - \frac{\mu_w}{2Pr} \sqrt{\frac{\rho_{w,o} u_\delta}{\mu_w x}} \rho_{*w} I_{w,o} \left(\frac{\partial I_*}{\partial \eta} \right)_w \quad (17)$$

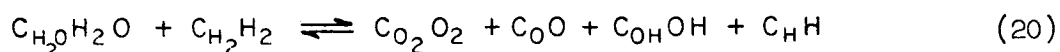
where η is the dimensionless y coordinate and the stars denote quantities non-dimensionalized with respect to the same quantity evaluated at the wall temperature. The corresponding expression for turbulent flow may be written as:

$$q_c = \frac{C_f}{2Pr} \rho_\delta u_\delta I_{w,o} \left[1 - \frac{i_{M\delta}}{I_{w,o}} - \frac{u_\delta^2}{2 g J I_{w,o}} \right] \quad (18)$$

There is some difficulty in interpreting Eq. (18) for use in the flow in a hydrogen-oxygen rocket system. Equation (17) was derived for a two-phase system such that the reaction could be written:



For the purpose of utilizing the same type of reaction scheme, the following reaction was assumed for the hydrogen-oxygen rocket system.



and the terms on the left were considered to constitute the "molecular" phase while the terms on the right constituted the "atomic" phase. This relation was used to determine the reference enthalpy, $I_{w,o}$, and the heat of recombination, h_R , which is used in the following analysis. The skin-friction coefficient, C_f , was determined from the empirical log form of the skin-friction law based on the von Kármán mixing hypothesis (see Ref. 50). The heat transfer rates calculated by this method for the hypothetical nozzle configuration of Fig. 13 are presented as the dashed curves in Fig. 14 for two different values of wall temperature. The Prandtl number associated with each wall temperature is also indicated on the figure. It can be seen that the heat transfer rate drops very rapidly from a moderately high value at the throat to low values near the exit of the nozzle.

The heat transfer rate discussed in the preceding paragraphs may be considered to be a lower limit for heat transfer in a nonequilibrium boundary layer. An upper

limit for the heat transfer rate may be obtained by considering the effect of a highly catalytic wall surface such that every atom which reaches the wall recombines upon striking it. The additional heat released to the wall by the recombination reaction is called the dissociated heat transfer, q_D , and may be added to the convective heat transfer to yield the total heat transfer to the wall, q_W . The dissociated heat transfer may be computed as:

$$q_D = h_R j_W \quad (21)$$

where h_R is the heat of recombination and j_W is the flux of atoms striking the wall. The atom flux may be written

$$j_W = k_W c_W \rho_W \quad (22)$$

if it is assumed that the wall is cool and there is a first-order catalytic reaction at the wall. If the atom concentration at the wall, c_W , is then normalized with respect to the free-stream concentration such that

$$z(y) = \frac{c}{c_\delta} \quad (23)$$

then

$$c_W = c_\delta z(0) \quad (24)$$

and Eq. (21) may be written

$$q_D = h_R k_W \rho_W c_\delta z(0) \quad (25)$$

All that now remains is to evaluate the dimensionless concentration through the boundary layer, and hence at the wall. This is carried out in APPENDIX IV by modifying the method of Ref. 48 and assuming a linear variation of free-stream velocity with distance from the throat of the nozzle. The resulting expression for the heat transfer rate may be written:

$$q_D = 0.836 (2\beta \rho_W \mu_W)^{1/2} Sc^{-2/3} h_R c_\delta \phi \quad (26)$$

where

$$\phi = \frac{1}{1 + \frac{0.836 (2\beta \rho_W \mu_W)^{1/2} Sc^{-2/3}}{\rho_W k_W}} \quad (27)$$

is the catalytic activity parameter and β is the velocity gradient parameter. It should be noted that the catalytic activity parameter, ϕ , is the same as that determined by Goulard in Ref. 48 and that this term is equal to 1 for $k_w > 10^3$. In the calculated results which follow, it was assumed that $\phi = 1.0$.

The total heat transfer rate, q_w , is also shown in Fig. 14 for two wall temperatures. It can be seen from this figure that except in the immediate region of the throat there is no difference between q_w and q_c . The ratio q_c/q_w is plotted as a function of area ratio in Fig. 15. From this figure it is seen that the catalytic contribution to the total heat transfer is greatest upstream of the throat and constitutes only 5% of the total heat transfer at the throat. These calculations were performed for only one chamber pressure, 60 psia. Calculations at higher chamber pressures would result in even lower percentages of heat transfer due to catalytic action at the wall surface since the "atomic" species concentration in the free-stream would be considerably lower for these cases.

TASK II - FINITE KINETICS NOZZLE FLOW MACHINE PROGRAMS

In the sections which follow under Task II brief discussions are made of the machine computational programs developed for analysis of one-dimensional and two-dimensional flow systems incorporating a treatment of finite chemical reaction rates. In addition, a review is included of the reaction mechanism and thermodynamic data for the hydrogen-oxygen system and the results of analyses using this information in the machine programs are discussed. The analyses include principally investigations of the effects of subsonic and supersonic area contours on thrust, brief examinations of possible alternative freezing point criteria, exploratory calculations to assess the general effects of scaling, vibrational nonequilibrium and combustion inefficiency on nozzle thrust and finally calculations to yield a family of modified perfect nozzles with internally axisymmetric flow of a recombining mixture of combustion products.

The One-Dimensional Finite Reaction Rate Analysis in Flow Systems

A machine procedure for the calculation of one-dimensional flow in exhaust nozzles incorporating the reaction kinetics of the gas has been developed to increase the accuracy and speed of this computation. The machine program numerically integrates the system of reaction kinetic, gas dynamic, and state equations to calculate all of the variables of interest in both subsonic and supersonic flow passages of varying cross-sectional area. The integration is performed by utilizing Hamming's modification of Milne's Predictor-Corrector (Ref. 51) integration procedure. The Runge-Kutta method is used for starting the machine computations. For nozzles the convergent-divergent area distribution can be introduced in tabular form or as a parabolic function of axial position. The prescribed area distribution controls the integration unless modified as described below. For the computations it is assumed that the gas mixture is ideal, the flow is steady, adiabatic, and one-dimensional. Also it is assumed that the effects of diffusion, heat conduction and viscosity are negligible, and that equilibrium among the internal energy states is maintained. Error control in this integration is incorporated in the usual way by specifying upper and lower error bounds.

The generalized equations which govern the nature of the flow and a discussion of the difficulties associated with the integration are presented in Appendix V.

There is a considerable amount of flexibility in the deck with respect to combustion chamber-nozzle combinations. A subsonic or supersonic combustion chamber may be followed by a variety of convergent-divergent or divergent nozzles. If desired, a nozzle calculation can be initiated from a set of prescribed conditions without calculating a combustion chamber, including starting directly from equilibrium. In order to include combustion chambers of varying degrees of efficiency, the combustion chamber size can be controlled by fixing its length or by prescribing the final slope of the temperature distribution.

In the convergent-divergent nozzle integrations, the transonic region is solved directly in the program, without iteration or restart, in the following manner. During the integration through the subsonic section, both the Mach number and the rate of change of the Mach number with distance are checked at each step. If the Mach number exceeds $1 - \epsilon_1$, (ϵ_1 & ϵ_2 are arbitrary, small positive quantities) or if the slope becomes negative, the control of the differential equation system is switched from area to Mach number, and a linear Mach number distribution is prescribed. The Mach number control is maintained until the Mach number exceeds $1 + \epsilon_2$. At this point both the new area (\tilde{A}) and the new area slope (\tilde{A}') are compared to the original input quantities (A, A'). If they are both sufficiently close, the control of the differential equation system is returned to the area and the input area distribution is modified by the relation,

$$\tilde{A} = \tilde{A}_b (A/A_b)^{\Delta'/\Delta} \quad (28)$$

where

$$\Delta' = \tilde{A}'_b/A'_b, \quad \Delta = \tilde{A}_b/A_b \quad (29)$$

and b refers to conditions at the transition point. If the comparisons are not sufficiently close, the Mach number is kept in control and the integration is terminated at a subsequent prescribed Mach number.

The deck can also be used to study the effect of various throat contours. As the equations are integrated through the nozzle, information is stored at a prescribed location in the convergent section. After the initial nozzle is calculated, the program returns to the stored position and determines a hyperbolic Mach number distribution using the Mach number and the slope of the Mach number at this position and a prescribed supersonic Mach number at different downstream locations. The equation system is then integrated using the Mach number distributions to control.

The running time of the deck depends on many variables: the number of reactions and species involved, the maximum errors allowed, the mode of operation and the proximity to equilibrium. The time for one complete step with the 6 species - 6 reaction hydrogen-oxygen system (Table 4) is approximately 0.35 seconds. In areas where equilibrium is maintained under changing environmental conditions, the rates of change of composition are very large, and for accuracy it is necessary to take small steps, thus increasing the total running time. As the reactions slow down, the step size increases and the running time reduces accordingly.

The integration procedure can solve a maximum matrix of twenty by twenty (that is, twenty species and twenty reaction equations) and a minimum of two by one.

Reaction Mechanism and Thermodynamic Data for the Hydrogen-Oxygen System

The selection of a reaction mechanism and reaction rates to be considered in the hydrogen-oxygen recombination scheme is a difficult matter. While considerable information is available concerning the species found and mechanisms likely to occur in hydrogen-oxygen and hydrogen-air reactions taking place at pressures near atmospheric, (Refs. 3 and 52), very little information can be found for reactions occurring at high pressures. Even in the low-pressure reactions where agreement exists on the species and mechanisms, the specific reaction rates are open to question. For example, the effects of different third bodies and temperatures have not been fully determined in the majority of reactions which are likely to be important in the study of nonequilibrium nozzle flows.

The species, mechanisms and reaction rates finally employed in this study were selected consistent with the reactions reported in Ref. 52 (based on consultation with Dr. T. M. Sugden of the Physical Chemistry Department of Cambridge University and Dr. J. P. Appleton of the University of Southampton).

The recombination model is represented by 6 reactions involving 6 species. The species are O, H, O₂, H₂, OH, and H₂O. The reactions and their rates which pertain to this study are listed in Table 4. The reactions utilized include most of those reported in recent ignition-delay and recombination studies involving the hydrogen-oxygen system (Refs. 38, 58, and 54). Although the species listed above are believed to be the important species, others could be written for the hydrogen-oxygen system at equilibrium. Several of the above will be present in such small quantities that they may be thermodynamically unimportant. However, kinetically, the species may be extremely important because of the role which they play in reactions which involve thermodynamically important species.

The thermochemical data utilized for these calculations are values consistent with JANAF thermochemical tables (Ref. 13). Specific heats of constituents are entered in tabular form and fitted so as to yield good derivatives and integrals. A base temperature of 1800° R is presently used for heats of formation although this may be changed by input if desired. The equilibrium constants, K_c and specific reaction rates, k_f , are in the form:

$$K_c = D_c T^{E_c} \exp (F_c/T) \quad (30)$$

$$k_f = D T^E \exp (F/T) \quad (31)$$

where D, E, and F are constants depending upon the reactions.

In order to obtain a comparison between the results that are calculated by using the reaction mechanism and specific reaction rates for the elemental reaction proposed in this program, a calculation was performed for the conditions which existed during experiments reported in Ref. 59. The results shown in Fig. 16 show good agreement which tends to corroborate the assumptions utilized in the analysis as well as the reaction rate data. The results of later experiments at slightly different conditions (Ref. 60) by Lezberg indicate much improved agreement. These results are also shown in Fig. 16.

One-Dimensional Performance Calculations

The computation procedure (described previously and in Appendix V) was used to investigate in a preliminary fashion for the low-pressure hydrogen-oxygen system the effect of finite reaction times on nozzle calculations. In particular, it was desired to investigate the effects of subsonic and transonic contours on thrust and the question of freezing. This calculation procedure was also used to provide input information for the two-dimensional and axisymmetric design and performance calculations discussed in following sections.

Three basic nozzle contours were used for most of the calculations. The first nozzle (I), designed for 150-pound thrust, had a conical convergent section with a 30° half angle followed by a throat section with a radius of curvature equal to twice the throat radius and ended with a 15° half-angle cone. The second nozzle (II), also designed for 150-pound thrust, had a 30° half-angle cone convergent section but this was followed by a throat section with a curvature ratio of 1/2 and a divergent cone with a 20° half angle. The third nozzle (III) was designed for 5000 pounds thrust by a linear scaling of nozzle I. Nozzles I and III were not exact duplicates because of the problem associated with scaling discussed below. Fig. 17 shows the three basic nozzles. In addition to these, other contour variations were introduced in the analysis of particular problems.

The chamber conditions for the nozzles were 60 psia pressure and an oxidizer-fuel ratio of 5.0. The resulting gases were expanded in equilibrium to a contraction ratio of 2. All the subsequent calculations with the kinetic deck started from this

point where the static pressure was 56.7 psia, the static temperature 5510° R and the mass fractions were: $H_2 = 0.060963$, $H = 0.0044507$, $O_2 = 0.0061517$, $O = 0.004279$, $OH = 0.040878$ and $H_2O = 0.883577$.

The results of the three basic nozzles along with equilibrium and frozen calculations are tabulated in Table 5 and Figs. 18, 19, and 20. As would be expected, the higher the value of the mean molecular weight at exhaust the higher the vacuum specific impulse. This is because the more recombination achieved in the nozzle the more energy available for thrust and the extent of recombination is reflected by the mean molecular weight.

It is interesting to note here that the sonic point generally is not at the minimum area. This fact has been discussed previously in the literature and the cause can best be seen by looking at the equation (developed in Appendix V as Eq. V - (11)) describing the temperature slope,

$$T' = \frac{2(H_0 - H) \left(\frac{A'}{A} - \frac{\sum \sigma_i'}{\sum \sigma_i} \right) + \left(\frac{2(H_0 - H)}{T \sum \sigma_i C_{p_i}} + M^2 - 1 \right) \sum h_i \sigma_i'}{(1 - M^2) \sum C_{p_i} \sigma_i} \quad (32)$$

The temperature decreases continuously throughout a critical nozzle. When the sonic point is reached, the denominator in the above equation vanishes and the numerator must vanish at the same time. This will occur when

$$\frac{A'}{A} - \frac{\sum \sigma_i'}{\sum \sigma_i} + \frac{\sum h_i \sigma_i'}{T \sum \sigma_i C_{p_i}} = 0 \quad (33)$$

It is not generally the case that this condition is satisfied when $A' = 0$, the minimum area point, as is the case for equilibrium and frozen flow. (For frozen flow, the σ_i' are zero and the sonic point must be at the minimum area location.)

The fact that the kinetic flow may not become sonic until after the contour has started to diverge has some interesting ramifications in the two-dimensional and axisymmetric studies. The starting conditions for these supersonic calculations must be carefully chosen since it is possible at the initiation of the axisymmetric calculation to encounter a situation in which the flow speed decreases even though the stream tube area is increasing.

Freezing Point

The concept of freezing has played an important part in the kinetic flow literature to date. The freezing point is the location in the nozzle from which further expansion does not produce any further sensible changes in composition. If the transition from equilibrium flow to frozen flow were to take place very quickly in a small section of the nozzle, the performance to be expected from kinetic flow could be predicted by assuming that the flow was in equilibrium up to some freezing point and frozen thereafter. This idea was originally put forth by K. N. Bray and with Bray's method for locating the freezing point, it has gained wide acceptance and use. A preliminary investigation has raised questions concerning the general applicability of this approach.

It is apparent that the flow never reaches a point beyond which the composition remains fixed. The rates of change of composition, however, do become very small, and for engineering purposes the flow can be assumed to be frozen. In order to measure the departure from frozen composition, two methods were employed. In the first method the process γ_p , $\gamma_p = \partial \ln p / \partial \ln \rho$ was compared to the frozen γ , $\gamma = (\partial \ln p / \partial \ln \rho)_{s, \sigma_1, \dots, \sigma_n}$. When the ratio of process γ_p to the frozen γ was within a prescribed tolerance of unity, the flow was considered frozen. In the second method, the mean molecular weight at a given location was compared to the weight at exhaust. When the ratio was sufficiently close to unity the flow was again considered frozen. Table 6 shows the results of this calculation (see also Fig. 20).

While it appears in some cases that the Bray criterion may give good results because the transition from equilibrium to frozen is contained in a small section of the supersonic portion of the nozzle, it is also evident that in some cases the flow deviates significantly from equilibrium by the time the throat is reached. Use of the Bray criterion here gives an over-optimistic performance prediction. Nozzle III had a mean molecular weight at the throat of 11.66 while nozzle II had a value of 11.62. An equilibrium value at the throat is approximately 11.68. Nozzle II was also run kinetically to the sonic point and then frozen to exhaust (see Figs. 18 and 19). The vacuum specific impulse in this case was 461 sec as compared to the all-kinetic value of 464 sec.

At the outset of this work, it was conjectured that it might be possible to increase the thrust of a nozzle significantly by suitably contouring the transonic region. It was anticipated that the freezing point might be moved farther downstream. Numerous reasonable throat contours were examined without any apparent increase in vacuum specific impulse. As a last resort a 1° divergent cone was attached to nozzle II at a Mach number of 1.003 and continued to a Mach number of 1.23 and then the flow was expanded rapidly into a 20° conical section. The exhaust mean molecular weight in this case was 11.75 and the vacuum specific impulse

increased from 464 sec to 470. Considering the length of the 1° section, it would seem that the effects of friction would probably cancel the resulting increase in performance. It would appear from these results that a more critical analysis of the Bray criterion is warranted. It also appears that a significant improvement in performance cannot be achieved by contouring in the neighborhood of the throat alone.

Scaling

The effects of scaling can be seen by comparing results for nozzles I and III. If both flows were calculated using equilibrium or frozen composition, they would have given identical results. However, with kinetic flow this was not the case. Nozzle I had a mean molecular weight at exhaust of 11.725 and a vacuum specific impulse of 467 sec, while nozzle III had an exhaust molecular weight of 11.863 and a vacuum specific impulse of 473 sec.

This departure can best be explained by considering the implications of equilibrium and frozen composition. For a flow assumed to be in equilibrium, the rates of reaction are infinite and therefore, the amount of time that the gases are at given conditions is not significant. In frozen flow, the reaction rates are zero and again it does not matter how long the gases are at given conditions. When finite reaction rates are used, the rate of change of the physical environment of the gas is of prime importance. In other words the nozzle residence time determines how close the kinetic flow will be to either equilibrium or frozen flow. Increasing the residence time by linearly scaling up a nozzle will allow the flow to remain close to equilibrium for a longer time and as a result have a higher impulse as is shown by the results.

The effect of residence time accounts for the fact that nozzles I and III are not identical even though III was designed originally by scaling up I. Since, in kinetic flow, the throat size of a nozzle cannot be prescribed simultaneously with the mass flow, the throat dimension is modified slightly to accommodate the change in mass flow. If the conditions in the two nozzles were identical at the minimum area, as they would be in frozen or equilibrium flow, the same throat height would have been calculated for both. In spite of the difference in contours some measure of the effect of scaling can be obtained by plotting properties against area ratios. It can be seen from the results that the main effect of this scaling is felt by the impulse and temperature. It should be noted that the pressure is not very sensitive to residence time and that experimental measurements of this quantity would probably not indicate differences (Figs. 21 and 22).

The effect of residence time can also be seen by comparing the results of nozzles I and II. Nozzle II had a shorter subsonic section and therefore a shorter residence

time. As would be expected, the mean molecular weight in nozzle I was greater and the specific impulse was higher (see Figs. 20 and 23).

Entropy was calculated in all the work done in this section and the increase was always less than one percent throughout a nozzle. It would appear, then, that isentropic flow assumptions would give good engineering answers if there is any need to use them.

Vibrational Non-Equilibrium

An order-of-magnitude effect on vibrational energy freezing was checked by assuming in nozzle II that the vibrations would freeze at the throat and therefore that specific heats would remain constant. Since the water contains most of the energy in this system and it is known to relax faster than the chemical composition, this assumption is very pessimistic. The vacuum specific impulse was within 5 percent of the kinetic value with equilibrium vibrational energy, and it is believed for the hydrogen-oxygen system that vibrational non-equilibrium can be ignored.

Combustion Efficiency

The effect of combustion efficiency on performance for nozzle II is indicated in Figs. 24 and 25. In this case, the deviation from 100% combustion efficiency is indicated by a temperature rise which is some fraction of the maximum possible temperature rise in the combustion chamber. From the results shown in Fig. 24, it is seen that no significant differences occur between vacuum specific impulses developed along the nozzle for the two different combustion efficiencies of 98% and 100%. However, the results of Fig. 25 show that small differences exist between the temperature profiles. When the combustion chamber efficiency is less than 100%, the reaction is still in progress toward equilibrium at the entrance to the nozzle. In this case, the temperature rises slightly during the early stages of the subsonic expansion until a temperature is reached which is about the same as that prevailing for 100% efficiency. Both sets of temperatures remain nearly constant as reaction and expansion effects essentially balance. Then the expansion effect becomes dominant and the temperature drops sharply just ahead of the throat.

The kinetic temperature profiles corresponding to the two chamber efficiencies begin to diverge in the supersonic portion of the exhaust nozzle with the curve representing the lower combustion efficiency maintaining a slightly higher temperature during the expansion. The small differences in temperature for this single calculation do not justify an unequivocal conclusion regarding the effect of combustion inefficiency. However, future studies may show that freezing of a lesser amount of dissociated gas mixture occurs when a combustion efficiency somewhat less than 100% is maintained.

General Description of Construction of the Two-Dimensional/Axisymmetric Nozzle Decks

A general description of the structure of the performance and design decks for the two-dimensional and axisymmetric nozzles is presented herein. The specific details of the numerical procedures employed are presented in Appendices VI and VII.

A significant aspect of the construction is the modification of the method of characteristics employed. Part of the standard procedure involves integrating the reaction kinetics equations along the segment of streamline employed in the construction of a mesh point. Repeated integration over such a segment is required for the iterative determination of such a point. Such repeated integrations are extremely costly, and when the flow is close to equilibrium the machine running time required is very large.

To obviate these difficulties, the integration of the reaction kinetics equations is restricted to so called "principal streamlines." These are approximately equally spaced (radially) across the flow field, usually about one streamline for each four Mach net points. Properties derivable from the constituent concentrations which are essential to the Mach net construction are then obtained by interpolation with a spline fit between principal streamline locations (Ref. 67).

When a particular Mach line has been established at each Mach net point on this line, $x, y, p, t, \rho, q, \psi, c^2$ will be known. In addition, the concentrations σ_i along with $x, y, p, t, \rho, q, \gamma$ are known at each principal streamline point, and spline fits of x, ρ, q, p, c^2 and X (a basic term in the characteristic equations) are available for interpolation purposes. A provisional determination of the next Mach line is made using frozen composition ($X = 0$). This is in turn used to determine provisional locations and directions for the principal streamlines. At this point, the reaction kinetic equations are integrated forward along principal streamlines, and temporary values of γ and X at these principal streamline positions fitted against the dimensionless stream function ψ . A second determination of the new Mach line is carried out taking the reaction kinetics into account.

This determination of the new Mach line is now an iterative process, but the process is rapidly convergent and two or three steps suffice to give results of sufficient accuracy.

When the criterion for freezing is satisfied (see page 39), the flow is assumed to be frozen and a frozen-composition construction is used to complete the calculation of the flow field or the determination of the nozzle contour. Henceforth, the concentrations at each of the principal streamlines are taken to be fixed, the quantity

γ determined at the principal streamline locations (dependent upon temperature T) and spline fitted between these streamline locations on the new Mach line.

There are two-dimensional/axisymmetric decks which have been developed in connection with this contract. The first of these, the so-called "performance deck" is used to determine the flow field associated with a given supersonic nozzle contour and prescribed conditions for the flow entering at the throat. The second deck, the so-called "design deck", is used to determine a family of modified perfect nozzles from which optimum nozzle contours are selected by truncation in the manner described in Ref. 61.

These modified perfect nozzles are nozzles having axial exit flow but not necessarily uniform speed (in view of the different residence times for the various principal streamlines). Once the exit Mach number has been reached on the axis by the characteristic construction method described above, successive down Mach lines are constructed backward from the exit Mach line in much the same manner of the conventional construction of perfect nozzles. The reaction kinetics integration is performed along principal streamlines as before, the principal modification being in the exit Mach line construction and constructions related directly to it. These are described in detail in APPENDIX VII.

Both of the two-dimensional/axisymmetric decks have been completed. The "performance deck" has been employed repeatedly in connection with the N_2O_4 system studied in Task III. The operation of this deck has provided considerable insight into the properties of the flow field construction and as a result, a variety of significant problem areas common to both axisymmetric decks has been exposed. Extensive analyses of these findings have been performed and modification of the calculation procedures have been incorporated. These problem areas and the modifications necessary are discussed below.

Step Control for the Runge-Kutta Integration Procedure

This control is essential for the integration of the reaction equations along the principal streamlines. Conventional step control methods employ concurrent calculation for a double step and require an additional expenditure of machine time which can be as much as 40% of the total computing time. Since time is critical, effort has been expended in devising a control procedure involving only a negligible amount of additional machine time (less than 1%). Such a procedure has now been developed. This step control procedure is quite comparable to that used in predictor-corrector schemes currently being employed in the one-dimensional kinetics deck (c.f. APPENDIX V).

Starting Conditions for Supersonic Calculations

The two-dimensional/axisymmetric supersonic decks were originally coded to start from uniform flow conditions (including axial direction for the flow) at the nozzle throat. Appreciable difficulty was encountered in starting both the N_2O_4 and H_2-O_2 calculations from these conditions. The source of the difficulty can be seen in Eqs. VI-(46), APPENDIX VI and VII-(3), APPENDIX VII. For uniform thermodynamic properties across the nozzle in the supersonic regime, the inclination, $\tan t$, of the flow increases with radial distance. This effect is directly associated with the fact that the sonic point occurs downstream of the minimum area section in one-dimensional flow. Physically and mathematically, the change in the inclination is sufficient to require that initial conditions consistent with Eq. VI-(46), APPENDIX VI be employed. The introduction of such a consistent set of initial conditions has in fact eliminated the starting problem.

Stability of Calculation Procedures

In the course of working with the two-dimensional "performance deck", it became apparent that integration of high precision is essential along the principal streamlines. Unless a careful control on error of the reaction kinetics equations is maintained, aberrations occur which have a significant effect upon the characteristic net construction. In addition to these purely local difficulties which occur between successive down Mach lines, there occurs under some situations an over-all instability having a period of one or two Mach line spacings. This is again controllable by the tolerance imposed in the principal streamline integrations.

It may be remarked parenthetically in view of these considerations that methods already published which purport to integrate the flow field equations using a reaction kinetic integration step of length approximately equal to the characteristic net gauge are open to serious question when conditions appreciably removed from freezing are encountered (c.f. Ref. 62).

Criterion for "Freezing"

The construction of the supersonic flow field is changed to a "frozen composition" construction when the γ_p/γ is sufficiently close to unity. Experience in working with these decks has shown that the effect of changing to frozen composition construction is more adequately measured by the quantity $[(\gamma_p/\gamma) - 1]$ than by the size of the concentration derivatives themselves.

Optimization Map

The design deck was used to construct an optimization map for H_2-O_2 (see Fig. 26). The subsonic-transonic section was taken from nozzle I and the axisymmetric characteristics construction was initiated at a Mach number of 1.005. The radius of curvature to throat radius was 2.0.

This map may be used to select nozzles of maximum thrust for prescribed length, exit area ratio, or surface area when surface area curves are added. Its use in these and other extremal problems is described in Ref. 61.

The minimum length nozzle chosen is the nozzle contour on the map terminated at point A . Its contour and thermodynamic properties are given in Table 7. During the design of these nozzles, the flow became sufficiently frozen to switch the calculation procedure to the frozen mode. The Mach line along which the change was made is indicated on the map.

TASK III - EXPERIMENTAL PROGRAM

In order to test the utility of the performance calculation procedure, it is necessary to compare the concentration profiles which are analytically predicted for a reacting gas flow in a converging-diverging nozzle of specified wall contour with those experimentally determined in a nozzle of identical scale and geometry.

Although experimental studies of the chemical kinetic behavior of various reacting mixtures in de Laval nozzles have been reported in the literature (e.g., Refs. 59 and 63), the investigations were restricted to the one-dimensional flow model. As the flow fields investigated in this program are either two- or three-dimensional in nature, it was necessary to design and execute an experiment comprised of measurements of the behavior of a chemically reacting mixture in a two-dimensional converging-diverging nozzle.

Method of Approach

The applicability of the nozzle flow reactor as a tool for the study of reaction kinetics was demonstrated conclusively in Ref. 63. The experimental program described herein is, for the most part, an extension of the techniques employed in Ref. 63 to provide for the measurement of reacting mixture compositions in two dimensions.

The flow of a reacting gas mixture through an adiabatic, two-dimensional converging-diverging nozzle can be completely described through measurement of the stagnation conditions and the axial and transverse distribution of any of the parameters of static pressure, reactant concentration, temperature or velocity. The choice of the optimum set of measurements for the study of reaction kinetics must be governed by a measurement error analysis as described in Ref. 64. On this basis, the measurement of concentration profiles was chosen as being most meaningful for this investigation.

The reaction system investigated in this program consists of a dilute mixture of nitrogen tetroxide (N_2O_4) and nitrogen dioxide (NO_2) carried in dry nitrogen gas. This system is characterized by the balanced reaction equation



and was selected for the following reasons:

1. The chemical kinetics and thermodynamic properties of the reactants are well known.
2. The system is characterized by a single reaction.
3. The reaction occurs at moderate temperatures ($810 > T > 360^\circ \text{R}$).
4. Of the three chemical species present in the reaction system, only one, NO_2 , is opaque to visible radiation at about 4000 \AA (Ref. 65).

The first of these items provides a sound basis for the comparison between the experimental and analytical results of the program. The second and third items provide means for avoiding the experimental complications associated with a study of the high temperature, multiple reaction systems which characterize the exhaust gases of most reaction propulsion devices. The single reaction feature is desirable in that a knowledge of the concentration of only one of the reacting species determines the state of the entire system under given conditions of temperature and pressure. This characteristic of the system is maintained so long as that temperature level ($\sim 810 \text{ R}$) above which significant dissociation of the nitrogen dioxide occurs is not exceeded in the flow reactor. Finally, the fourth item permits the use of well-established photometry techniques for the determination of specie concentration in the flow field.

The light transmitted through a homogeneous mixture of N_2 , N_2O_4 , NO_2 can be related to the concentration of the absorbing constituent, NO_2 , through the Beer-Lambert Law,

$$\sigma = \frac{I}{I_i} = e^{-BD[\text{NO}_2]} \quad (35)$$

The NO_2 molar extinction coefficient, B , has been shown to be independent of temperature within the range of interest of this experiment (Refs. 63 and 66) and, therefore, the ratio of the concentration of nitrogen dioxide at any station in a two-dimensional nozzle of constant width to the concentration at the nozzle throat can be determined as follows:

$$\frac{\ln \sigma}{\ln \sigma_t} = \frac{[\text{NO}_2]}{[\text{NO}_2]_t} \quad (36)$$

Implicit in Eq. (36) is the assumption that uniform reactant concentrations exist along the optical path between and normal to the nozzle side walls. This assumption is justified if the side wall boundary layers, which contain high concentrations of the dissociated specie due to the high static temperature near the wall, represent a small fraction of the transmitted light beam path length. Also, knowledge of the displacement on the top and bottom walls of the test nozzle is necessary so the experimental and analytical results can be compared on the common basis of the inviscid area ratio versus length profile. For these reasons, calibration of the test nozzle to determine boundary layer displacement thickness was necessary.

Several additional requirements had to be satisfied in the design of the test apparatus. These were as follows: (a) to provide stable regulation of reaction system temperature and pressure; (b) to provide a means for accurate determination of the location of the absorption paths within the test nozzle; (c) to allow for a sufficiently high test nozzle aspect ratio in order to minimize secondary flow effects in the two-dimensional flow channel; (d) to incorporate nozzle wall configurations which minimize heat loss from the reacting gas stream; and (e) to construct a nozzle contour such that the flow field is free of shocks and freezing of the chemical reaction occurs within the supersonic portion of the test nozzle.

Apparatus

A detailed description of the major test components appears in APPENDIX VIII. In the presentation which follows, a brief discussion of the test apparatus is included. Figure 27 shows a schematic diagram of the test apparatus. Dry gaseous nitrogen was supplied to the flow reactor from a high-pressure storage manifold. The N_2 discharge pressure was controlled in two stages by dome-loaded regulators and the flowrate of N_2 was metered by an ASME long radius flow nozzle. Liquid nitrogen tetroxide was displaced from its shipping container by means of dry nitrogen pressurization and was injected into the carrier gas stream between the two stages of the heater system. The reactant flowrate was controlled by a vernier throttling valve and measured by an accurately calibrated rotameter. The heater system served to raise the temperature of the N_2 /reactant gas stream to the level at which essentially complete dissociation of the nitrogen tetroxide is achieved and the second stage heater provided more than sufficient duct length for complete turbulent mixing of the reactants. After heating, the gas mixture passed through a calming section which contained a screen filter bed to decrease the level of turbulence and to remove particulate foreign matter prior to its entrance to the test section. The test section (Figs. 28 and 29) comprised a two-dimensional, converging-diverging half-nozzle having a constant width (2.5 in.), an area contraction ratio of 6.385, a blended throat of 2.5 in. radius, and an area expansion ratio of 2.013. The convergence angle was 30° and the divergence angle was 14° .

The nozzle aspect ratio was 4 at the plane of the throat. The nozzle side walls included optically flat pyrex windows to facilitate the absorption measurements. A fixed geometry, two-dimensional, supersonic diffuser was provided to ensure shock-free flow in the supersonic portion of the test nozzle and an air powered ejector provided low back pressure at the diffuser exit. Diluent air was mixed with the ejector exhaust to minimize the toxicity hazard associated with the handling of the NO_2 and N_2O_4 . All tunnel components upstream of the test nozzle which were subject to exposure to the chemical reactants were fabricated of stainless steel. Teflon gaskets were employed between the flanges of these components.

A special five-beam absorption photometer (Figs. 30 and 31) was mounted on a traversing mechanism which was held in fixed relationship to the test nozzle axis. This instrument permitted measurement of the absorption of the reacting gas mixture on five absorption paths equally spaced 0.250 in. apart in the vertical direction and at any horizontal position along the nozzle axis.

A photograph of the main portion of the tunnel is presented in Fig. 32 . A calibration model having an internal scale and geometry identical to the test nozzle and an external configuration suitable for mounting in an existing wind tunnel was designed and fabricated. This nozzle was thoroughly instrumented with pressure taps to permit determination of the characteristics of the internal flow field. The wind tunnel test section was equipped with a traversing mechanism to facilitate the measurement of pitot pressure profiles between the top and bottom walls at various axial locations in the supersonic portion of the calibration nozzle. It was possible to adjust the probe mechanism to make vertical traverses off the nozzle centerline but transverse profiles could not be obtained with this mechanism.

Test Procedure

The calibration model was installed in a continuous-flow wind tunnel and measurements of centerline and transverse static pressure profiles were made at various locations along the nozzle axis. Also, pitot pressure traverses of the nozzle boundary layer were made at selected axial locations on the centerline of the top and bottom wall of the nozzle. In addition to the centerline measurements in the nozzle exit plane, a vertical traverse was made at a distance of 0.040 in. from the side wall of the nozzle. The flowing medium during these tests was air and the temperature and pressure of the gas were adjusted so that the calibration Reynolds numbers were similar to those expected for the test nozzle during experiments with the reacting gas system.

A series of preliminary tests were made to determine the stability of temperature, pressure and reactant mixture regulation of the gas stream in the flow reactor

under conditions of continuous flow. Operation of the reactor during the final series of experiments was as follows:

1. The temperature controllers on the eutectic bath heater were preset to the desired level and the alloy allowed to reach an equilibrium temperature.
2. The ribbon-filament light source and the regulated photomultiplier power supply were turned on and allowed to equilibrate.
3. All system thermocouples were calibrated with a Technique Associates, Inc., Pyrotest (model 9B) and all pressure transducers were calibrated against Heise Laboratory Test gages or mercury manometers, depending on pressure range.
4. The air supply to the tunnel exhaust system was initiated.
5. A flow of 100 psi steam was initiated in the preheater and the temperature controller which governed the position of the steam inlet valve was set to maintain the desired nitrogen temperature at the heater outlet.
6. The nitrogen tetroxide supply system was purged with dry nitrogen and the expellant nitrogen pressure regulator was set for the desired delivery pressure.
7. Nitrogen flow was initiated in the tunnel and adjusted to yield the desired pressure and temperature at the test section entrance.
8. Nitrogen tetroxide flow was initiated and adjusted to the preselected flowrate.
9. The recording instrumentation was started and an optical traverse of the test nozzle from the entrance plane to the exit plane was made.
10. Measurements of the intensity of the light transmitted through the test nozzle windows with no reactant in the test section were made and recorded before and after each run with reactants.

The pertinent parameters which were measured and recorded during a test run were:

1. Nitrogen flow nozzle upstream pressure

2. Nitrogen flow nozzle differential pressure
3. Nitrogen temperature at flow nozzle
4. Nitrogen tetroxide flowrate
5. Nitrogen tetroxide temperature at flowmeter entrance
6. Test nozzle entrance temperature
7. Test nozzle entrance pressure
8. Test nozzle exit pressure
9. The output of the five photomultipliers of the photometer system
10. Axial location of the photometer system relative to the test nozzle

All of the above parameters were recorded simultaneously and continually during a test run at a sampling rate of ten scans per second on an Epsco high-speed data recording system having an accuracy of $\pm 0.33\%$.

Results and Discussion

The results of the flow calibration of the test nozzle configuration are summarized in Figs. 33 through 35. Figure 33 shows the variations of Mach number and pressure ratio with axial distance from the throat along the top and bottom walls of the calibration nozzle. The pressure distribution measured on the centerline of the top wall of the test nozzle under conditions of temperature and pressure representative of those experienced during reaction experiments is in good agreement with that measured during air flow tests of the calibration nozzle. This agreement is an indication of the similarity of the flow fields in the two nozzles. The Mach number profiles calculated on the basis of the measured static pressure profiles (on the top and bottom walls of the calibration nozzle) are compared with those predicted from theoretical analysis of the two-dimensional flow field in the test nozzle for temperatures and pressures similar to those experienced during the reaction experiments. This comparison indicates that the flow field in the test nozzle was free of shocks.

The fact that the gas flow was one-dimensional in the transverse direction is demonstrated by the measured static pressure distributions shown in Fig. 34 and by pitot pressure ratio curves shown in Fig. 35. The static pressure measurements

describe flat distribution profiles in the direction normal to the side wall at various axial locations on the top and bottom walls of the nozzle. The pitot pressures measured in the nozzle exit plane were essentially invariant from the nozzle centerline to near the nozzle side wall. This last result indicates that the side wall boundary layers occupy less than 3.2% of the test nozzle width.

The results of vertical pitot pressure traverses made at various axial locations along the nozzle centerline were employed in calculation of the boundary layer displacement thickness on the top and bottom walls of the nozzle. Because the boundary layers were quite thin, the pitot probe thickness represented an appreciable fraction of the boundary layer thickness and considerable scatter of the test data resulted. However, the displacement thicknesses calculated from these measurements were in general agreement with those predicted from theory (Fig. 36). Based on these results, the theoretically predicted boundary layer displacement thickness profiles were used in subsequent calculation of the effective nozzle area versus length profile for inviscid, two-dimensional flow in the test nozzle.

Three entirely independent tests were run for comparison with the analytical predictions of the two-dimensional "performance deck". The experiments and the analytical predictions were made with the following nominal operating conditions at the test nozzle entrance:

Total Pressure	33.0 psia
Total Temperature	770 R
Total Mass Flow Rate	1.0 lb/sec
NO ₂ Mole Fraction	0.03

Deviations from the above values were less than 2% for all three experiments.

Values of the transmitted light intensity ratios, σ , were obtained as functions of distance from the nozzle throat along each of the five light beam traverse paths for each test run. The transmitted light intensity ratios for each traverse path were then averaged with values from the other tests at corresponding locations in the supersonic portion of the test nozzle to obtain five curves of average σ versus axial distance from the nozzle throat. Finally, the logarithms of the averaged values of σ at selected axial locations were divided by the logarithm of the averaged value of σ at the nozzle throat on the same traverse path to determine the desired nitrogen dioxide concentration ratios, $[NO_2] / [NO_2]_t$. For the cases where no throat value of σ existed, (i.e., for the two traverse paths farthest from the bottom wall of the nozzle) the value of the average σ at the throat on the third traverse path from the bottom wall was used as the reference in the calculations.

Because the side wall boundary layers occupied less than 3.2% of the light beam path length at the nozzle exit and were even thinner at all other axial locations in the supersonic portion of the test nozzle, any attempt to correct the measured absorption of the gas stream for nonhomogeneity caused by reactant dissociation in the boundary layers was not justified by the experimental measurement accuracy and, therefore, no such attempts were made.

The experimentally determined values of the concentration ratios at various distances from the test nozzle throat for each of the five light beam traverse paths are presented in Fig. 37 and are compared with the analytical predictions in Fig. 38. With the exception of the region near the bottom wall of the nozzle, the experimental measurements are in good agreement with the predicted results. The disagreement near the nozzle wall is most probably due to the discrepancy between the Mach number profile which existed at the test nozzle throat and that which was assumed as a starting condition for the two-dimensional "performance deck". The shape of the sonic line in the test nozzle was not described by the experimental measurements. However, it is certain that it was two-dimensional and that speed and concentration were not uniform across the throat of the nozzle as was assumed in the analytical procedures. Thus, the locations of the concentration ratios predicted analytically tend to differ from those described experimentally due to the slight mismatch between the values of the throat concentrations employed as the reference in each case. The fact that the region near the bottom wall is most sensitive to such a mismatch can be demonstrated through reference to the analytical results which are presented in Fig. 39. As shown, the predicted concentration ratio gradients along the streamline nearest the top wall at the nozzle throat are much steeper than those near the bottom wall. If the curves are displaced vertically (which would be the case if a different throat concentration were used as the reference) the axial location of a given concentration ratio is shifted by a greater amount near the bottom wall than it is near the top wall. This is the effect noted in Fig. 38.

Another item of interest which is demonstrated by the results of the kinetic calculations is that, contrary to the one-dimensional predictions afforded by Bray Criterion analysis, the approximate region of "chemical freezing" is two-dimensional. The location of this region, which is shown in Fig. 38, was determined by observing the point on each of the streamlines (Fig. 39) at which a marked decrease in the magnitude of the NO_2 concentration gradients occurred. Upstream of the abrupt change in the gradients the concentrations (as measured on a volume basis) vary through the combined mechanisms of chemical reaction and volumetric expansion of the flow, whereas, downstream of the abrupt change the concentrations vary principally through flow expansion.

The generally good agreement between the theoretical calculations and the experimental results throughout the two-dimensional flow field tends to corroborate the rate constants used in the computations and offers firm evidence of the utility of the calculation procedure.

LIST OF REFERENCES

1. Bray, K. N. C.: Journal of Fluid Mechanics, Vol. 6, No. 1, 1959.
2. Hall, J. G., A. Q. Eschenroeder, and P. V. Marrone. Inviscid Hypersonic Airflows with Coupled Nonequilibrium Processes. Cornell Aeronautical Laboratory Report No. AFl413A2, May, 1962.
3. Sarli, V. J., A. W. Blackman, and R. F. Buswell: Kinetics of Hydrogen-Air Flow Systems II. Calculations of Nozzle Flows for Ramjets. Presented at Ninth Symposium (International) on Combustion, Ithaca, New York, August 1962.
4. Westenberg, A. A., and S. Favin: Nozzle Flow with Complex Chemical Reaction. Applied Physics Laboratory Report No. CM-1013, March 1962.
5. Dynamics of Two-Phase Flow in Rocket Nozzles. Fourth Quarterly Technical Progress Report, United Technology Corporation, No. 2005 QT4, May 26, 1962. Contract No. NOW-61-0760-c.
6. Stollery, J. L., and J. E. Smith: A Note on the Variation of Vibrational Temperature Along a Nozzle. Journal of Fluid Mechanics, Vol. 13, 1962, p. 226.
7. Musgrove, P. J., and J. P. Appleton: On Molecular Vibrational Relaxation in Flow of Chemical Reacting Gas. University of Southampton, Department of Aeronautics and Astronautics, June 1961 (AD 267761).
8. Lordi, J. A.: ARS Journal, Vol. 32, No. 1285, 1962.
9. Sutton, E. A.: Journal of Chemical Physics, Vol. 36, No. 2923, 1962.
10. Benson, S. W.: The Foundations of Chemical Kinetics. New York: McGraw-Hill, 1960.
11. Frost, A. A., and R. G. Pearson: Kinetics and Mechanism. New York: Wiley, 1953.
12. Gilbert, M., and D. Altman: The Chemical Steady State in HBR Flames, I and II. Jet Propulsion Laboratory, Progress Reports No. 20-276 and 20-277, June 1955.
13. JANAF Interim Thermochemical Tables. The Dow Chemical Company, 1960.

LIST OF REFERENCES
(Cont.)

14. Duff, R. E.: Journal of Chemical Physics, Vol. 28, No. 1193, 1958.
15. Fenimore, C. P., and G. W. Jones: Journal of Physical Chemistry, Vol. 65, No. 993, 1961.
16. Fenimore, C. P., and G. W. Jones: Journal of Physical Chemistry, Vol. 63, No. 1154, 1959.
17. Wray, K. L., J. D. Teare, et al: Eighth Symposium (International) on Combustion, Baltimore, Maryland: Williams and Wilkins, 1962, p. 328-339.
18. Fenimore, C. P., and G. W. Jones: Journal of Physical Chemistry, Vol. 62, No. 1598, 1958.
19. Fenimore, C. P., and G. W. Jones: Journal of Physical Chemistry, Vol. 65, No. 2200, 1961.
20. Shuler, K. E.: Relaxation of an Isolated Ensemble of Harmonic Oscillators. Journal of Chemical Physics, Vol. 32, 1960, p. 1692 (and references cited therein).
21. Heims, S. P.: Effect of Oxygen Recombination on One-Dimensional Flow at High Mach Numbers. NACA TN-4144, January 1958.
22. Hall, J. Gordan, and A. L. Russo: Studies of Chemical Nonequilibrium in Hypersonic Nozzle Flow. AFOSR TN-59-100, November 1959.
23. Li, T. Y.: Nonequilibrium Flow in Gas Dynamics. AFOSR TN-59-389, May 1959.
24. Brout, R.: Rotational Energy Transfer in H_2 . Journal of Chemical Physics, Vol. 22, 1954, p. 934.
25. Schwartz, R. N., and K. Herzfeld: Vibrational Relaxation in Gases. Journal of Chemical Physics, Vol. 22, 1954, p. 767.
26. Tanczos, F. I.: Journal of Chemical Physics, Vol. 25, 1956, p. 439.
27. Hammerling, P., J. D. Teare and B. Kivel: Theory of Radiation from Luminous Shock Waves in Nitrogen. The Physics of Fluids, Vol. 2, 1959, p. 422.

LIST OF REFERENCES
(Cont.)

28. Treanor, C. E., and P. V. Marrone: Effect of Dissociation on the Rate of Vibrational Relaxation. *The Physics of Fluids*, Vol. 5, 1962, p. 1022.
29. Marrone, P. V., and C. E. Treanor: Chemical Relaxation with Preferential Dissociation from Excited Vibrational Levels. Cornell Aero. Laboratory Report, QM 1626-A-10, February 1963.
30. Herzfeld, K.: Relaxation Phenomena in Gases. Section H of *Thermodynamics and Physics of Matter*. F. D. Rossini, Ed., Princeton University Press, 1955.
31. Patch, R. W.: Prediction of Composition Limits for Detonation of Hydrogen-Oxygen Diluent Mixtures. *ARS Journal*, Vol. 31, 1962, p. 46.
32. Blackman, V.: Vibrational Relaxation in Oxygen and Nitrogen. *Journal of Fluid Mechanics*, Vol. 1, 1956, p. 61.
33. Parker, J. G.: Rotational and Vibrational Relaxation in Diatomic Gases. *Physics of Fluids*, Vol. 2, 1959, p. 449.
34. Lambert, J. D., R. Salter, and B. Warburton: Temperature Dependence of Vibrational Relaxation Times. *Proceedings of the Royal Society of London, Series A*, Vol. 244, 1954, p. 212.
35. Edmonds, R. D., and J. Lamb: Vibrational Relaxation Times of a Number of Polyatomic Gases Derived from Measurements of Acoustic Absorption. *Proceedings of the Physical Society*, Vol. 72, 1958, p. 940 (and references cited therein).
36. Dickins, P. G., and A. Ripamonti: Calculation of Vibrational Relaxation Times in Gases. *Transaction of the Faraday Society*, Vol. 57, 1962, p. 735.
37. Morris, J. F.: *Physics-Chemical Reactions During Nozzle Flow*. The Chemistry of Propellants, Pergamon Press, 1960.
38. Patch, R. W.: Shock Tube Measurement of Dissociation Rates of Hydrogen. *Journal of Chemical Physics*, Vol. 36, April 1962.
39. Montroll, E. W., and K. E. Shuler: *Journal of Chemical Physics*, Vol. 26, 1957, p. 454.

LIST OF REFERENCES
(Cont.)

40. Bayley, N. W., et al: Journal of Chemical Physics, Vol. 28, 1958, p. 700.
41. Dynamics of Two-Phase Flow in Rocket Nozzles. (U) Sixth Quarterly Technical Progress Report, United Technology Corporation, No. 2005QT6, November 30, 1962. Contract No. NOW-61-0760-c. (Confidential).
42. Kliegel, J. R., and G. R. Nickerson: Flow of Gas Particle Mixtures in Axially Symmetric Nozzles. ARS Preprint No. 1713-61. Presented at ARS Propellants, Combustion and Liquid Rockets Conference, April 26-28, 1961.
43. Kliegel, J. R.: One-Dimensional Flow of a Gas Particle System. IAS Paper No. 60-5, 28th Annual Meeting, New York, New York, January 25-27, 1960.
44. Dynamics of Two-Phase Flow in Rocket Nozzles. Second Quarterly Technical Progress Report, United Technology Corporation, No. 2005QT2, November 1961. Contract No. NOW-61-0760-c.
45. Dynamics of Two-Phase Flow in Rocket Nozzles. Fifth Quarterly Technical Progress Report, United Technology Corporation, No. 2005QT5, August 30, 1962. Contract No. NOW-61-0760-c.
46. Sehgal, R.: An Experimental Investigation of a Gas-Particle System. JPL Technical Report No. 32-238, Pasadena, California, March 16, 1962.
47. Fay, J. A., and F. R. Riddell: Theory of Stagnation Point Heat Transfer in Dissociated Air. Journal of the Aeronautical Sciences, Vol. 25, No. 2, February 1958.
48. Goulard, R.: On Catalytic Recombination in Hypersonic Stagnation Heat Transfer. Jet Propulsion, November 1958.
49. Sziklas, E. A., and O. L. Anderson: Analysis of the Hypersonic Nonequilibrium Boundary Layer. UAC Research Laboratories Report R-1720-1, March 1961.
50. Turbulent Flows and Heat Transfer. C. C. Lin, Editor, High Speed Aerodynamics and Jet Propulsion, Vol. 5, Princeton University Press, 1959.
51. Hamming, R. W.: Stable Predictor Corrector Methods for Ordinary Differential Equations. Journal Association Computing Machinery, Vol. 6, 1959.

LIST OF REFERENCES
(Cont.)

52. Montchiloff, I. N., E. D. Taback, and R. F. Buswell: Kinetics of Hydrogen-Air Flows Systems I. Calculation of Ignition Delays for Hypersonic Ramjets. Ninth Symposium (International) on Combustion, Cornell University, Ithaca, New York, August 27 - September 1, 1962.
53. Semenov, N. N.: Some Problems of Chemical Kinetics and Reactivity, Vol. 2, Pergamon Press, London, 1959. (Quoted in Ref. 54).
54. Bray, K. N. C., and J. P. Appleton: Atomic Recombination in Nozzles: Methods of Analysis for Flows with Complicated Chemistry. University of Southampton, A.A.S.U. Report No. 166, April 1961.
55. Karmilova, L. V., and R. V. Lorentso: Zhurnal fizicheskoi Khimii, Vol. 24, 1950, p. 207. (Quoted in Ref. 54).
56. Clyne, N. A., and B. A. Thrush: Nature, Vol. 189, 1961, p. 4759. (Quoted in Ref. 54.)
57. Mathews, D. L.: Physics of Fluids, Vol. 2, 1959, p. 2.
58. Schott, G. L., and J. L. Kinsey: Journal of Chemical Physics, Vol. 29, No. 5, pp. 1177-1182, 1958.
59. Lezberg, E. A., and R. B. Lancashire: Recombination of Hydrogen-Air Combustion Products in an Exhaust Nozzle. NASA TN NASA D-1052, 1961.
60. Lezberg, E. A., and L. C. Franciscus: Effects of Exhaust Nozzle Recombination on Hypersonic Ramjet Performance. AIAA-ASME Hypersonic Ramjet Conference, Naval Ordnance Laboratory, White Oak, Maryland, April 23-25, 1963.
61. Ahlberg, J. H., S. Hamilton, D. Migdal, and E. N. Nilson: Truncated Perfect Nozzles in Optimum Nozzle Design. ARS Journal, pp. 614-620, May 1961.
62. Schainblatt, A. H.: Numerical Calculation of Chemically Reacting Hypersonic Flow Fields, Convair, San Diego, June 1961. Army Rocket and Guided Missile Agency DA-04-495-ORD-3112, AD 269543.
63. Wegener, P. P., J. Morte, and C. Thiele: Study of Supersonic Flows with Chemical Reactions. Measurement of Rate Constants of the Reaction $N_2 + N_2O_4 \rightleftharpoons N_2 + 2NO_2$ at Low Reactant Concentrations. Jet Propulsion Laboratory, Progress Report No. 20-349, June 1958.

LIST OF REFERENCES
(Cont.)

64. Bray, K. N. C., and J. P. Appleton: The Choice of an Optimum Set of Measurements to Study the Atomic Recombination in Nozzles. University of Southampton, Aeronautics and Astronautics Report No. 120, November 1959.
65. Hall, T. C., Jr., and F. E. Blaset: Separation of Absorption Spectra of NO_2 and N_2O_4 in the Range of 2400 - 5000 \AA . Journal of Chemical Physics Vol. 20, p. 1745, November 1952.
66. Rosser, W. A., and H. Wise: Gas Phase Oxidation of Ammonia by Nitrogen Dioxide. Jet Propulsion Laboratory, Progress Report No. 20-273, September 1955.
67. Walsh, J. L., J. H. Ahlberg, and E. N. Nilson: Best Approximation Properties of the Spline Fit. Journal of Mathematical Mechanics II, 1962, pp. 225-234.
68. Ahlberg, J. H., and E. N. Nilson: Convergence Properties of the Spline Fit. Journal of the Society of Industrial and Applied Mathematics, Vol. 11, No. 1, March 1963.
69. ASME Power Test Codes. Supplement on Instruments and Apparatus, Part 5, Chapter 4, February 1959.

LIST OF SYMBOLS

A	Area (APPENDIX VI) Tangent of Mach angle (APPENDIX I) Reactant species (APPENDIX I)
a	Stoichiometric coefficient of reactant (APPENDIX I) Speed of sound (APPENDIX III)
A*	Throat area
B	Molar extinction coefficient for NO ₂ (TASK III) Product species (APPENDIX I)
b	Stoichiometric coefficient of product (APPENDIX I)
C	Concentration (APPENDIX I)
C _D	Drag coefficient
C _F	Thrust coefficient
C _f	Coefficient of friction
C _p	Specific heat
C _{Tg}	Gross thrust coefficient
c	Velocity of sound
c	Concentration of atomic species (APPENDIX IV)
c*	Characteristic velocity
D	Diffusion coefficient (APPENDIX IV) Forward rate constant coefficient (TASK II)
D _c	Equilibrium constant coefficient (TASK II)
E	Forward rate constant coefficient (TASK II)
E _c	Equilibrium constant coefficient (TASK II)

LIST OF SYMBOLS
(Cont.)

F	Thrust Forward rate constant coefficient
F_c	Equilibrium constant coefficient
f	Blasius function (APPENDIX IV)
ΔG°	Standard Gibbs free energy change
g	Gravitational constant
H	Enthalpy
$\Delta H_R, h_R$	Heat of reaction
h	Specific enthalpy
I	Total enthalpy (APPENDIX IV) Intensity, photomultiplier output (TASK III)
I_0	Reference intensity, photomultiplier output (TASK III)
I_{sp}	Vacuum specific impulse
i	Index
i	Enthalpy
J	Mechanical energy equivalent of heat energy
J	Flux of atomic species (APPENDIX IV) Index
K_C, K_P	Equilibrium constants in concentration units and pressure units
K_f, K_b k_f, k_b }	Specific reaction rate constants, forward reactions and reverse reactions
k	Index

LIST OF SYMBOLS
(Cont.)

L	Parameter in characteristic equations (APPENDIX VII)
e	Ratio, $\rho u / \rho_w u_w$ (APPENDIX IV)
M	Mach number Symbol representing all species (APPENDIX V)
\bar{m}	Molecular weight (APPENDIX I)
\dot{m}	Mass flow rate
N	Number of moles per unit mass (APPENDIX I) Parameter in characteristic equations (APPENDIX VI)
Nu	Nusselt number
n	Polytropic exponents for gas particle mixture (APPENDIX III) Total number of reactions
P, p	Pressure
P_c	Chamber pressure
Pr	Prandtl number
Q	Vibrational relaxation parameter
q	Speed
q_c	Convective heat transfer rate (APPENDIX IV)
q_D	Heat transfer due to recombination (APPENDIX IV)
q_w	Total heat transfer (APPENDIX IV)
R	Radius of curvature of nozzle throat (APPENDICES I & III)
R	Gas constant
\mathcal{R}	Gas constant (APPENDICES I & III)

LIST OF SYMBOLS
(Cont.)

r	Reaction rate (APPENDIX I)
r_p	Particle radius
r_t	Throat radius
S	Entropy
Sc	Schmidt number
s	Length of arc (APPENDIX VI) Transformation function (APPENDIX IV)
T	Temperature
t	Slope of streamline (APPENDIX VI) Time coordinate (APPENDIX I)
u	Velocity coordinate
V	Velocity (APPENDIX V)
v	Velocity coordinate
W	Molecular weight
w	Weight flow-rate fraction of particles (APPENDIX III)
X	Parameter in characteristics equation (APPENDIX VII, Eq. (3))
x	Distance coordinate
y	Distance coordinate
Z	Particle-to-gas mass-flow-rate ratio (APPENDIX III)
α	Mach angle

LIST OF SYMBOLS
(Cont.)

a_{ij}', a_{ij}''	Stoichiometric coefficient of the i th species in the j th reaction, reactants and products respectively
α_F	Mass fraction at freezing point (APPENDIX I)
β	Velocity gradient parameter (APPENDIX IV)
β_{ij}	Number of atoms of i th atomic species in the j th molecular species
γ	Ratio of specific heats
ϵ	0 and 1 for plane and axisymmetric flow respectively (APPENDICES VI & VII)
ζ	Reaction parameter in axisymmetric flow (APPENDIX VI)
η	Modified variable Dorodnitsyn (APPENDIX IV)
η	Axis normal to streamline
θ	Vibration temperature (APPENDIX II) Temperature lag $(T_c - T_p)/(T_c - T_q)$ (APPENDIX III) Angle of inclination of the streamline relative to axis of symmetry (APPENDIX VI)
κ	Constant in Bray criterion (APPENDIX I)
λ_j	Variables defined in APPENDIX V, Eq. (20)
μ	Viscosity (APPENDIX IV) Radius ratio (APPENDIX VIII, Eq. (16))
ν	Change in number of moles of gas (APPENDIX I)
ξ	Axis along streamline (APPENDIX VI & VII)
ρ	Density
σ	Concentration: mass fraction divided by molecular weight Transmitted light intensity ratio (TASK III)

LIST OF SYMBOLS
(Cont.)

τ Vibrational relaxation time (APPENDIX II)
Shear stress (APPENDIX IV)

ϕ Axial velocity ratio (APPENDIX III)
Characteristic function (APPENDIX VI)

ψ Stream function

Subscripts

c Chamber

d Denotes down Mach line (APPENDIX VIII)

e Exhaust

g Gas

i Index

Index

k Index

M Quantity evaluated for the mixture of atomic and molecular species (APPENDIX IV)

n_a Number of atomic species

n_r Number of reactions

p Particle (APPENDIX III)

u Denotes up Mach line (APPENDIX VIII)

w Quantity evaluated at wall temperature (APPENDIX IV)

$w,0$ Quantity evaluated at wall temperature for condition of zero (APPENDIX IV)
atomic species concentration

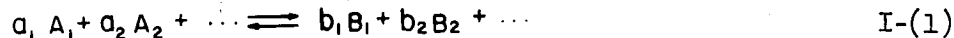
LIST OF SYMBOLS
(Cont.)

- δ Denotes edge of boundary layer (APPENDIX IV)
- * Dimensionless quantity (APPENDIX IV)

APPENDIX I

DEPARTURE FROM EQUILIBRIUM IN ROCKET NOZZLES

Consider one of the many reversible elementary reactions which may take place as the combustion products are expanded through a rocket nozzle:



The forward and reverse rates of this elementary reaction are conventionally expressed as follows (Ref. 10):

$$r_F = k_F(T) C_{A_1}^{a_1} C_{A_2}^{a_2} \dots \quad \text{I-(2)}$$

$$r_R = k_R(T) C_{B_1}^{b_1} C_{B_2}^{b_2} \dots \quad \text{I-(3)}$$

where r_F and r_R are respectively the forward and reverse rates of reaction in a unit volume of reacting mixture; C_{A_1} , C_{A_2} , ..., C_{B_1} , C_{B_2} , ..., are molar concentrations of the reacting species; and $k_F(T)$, $k_R(T)$, are the temperature-dependent specific rate constants for the forward and reverse directions. Most elementary reactions are characterized by interactions of two species, occasionally three, in simple encounters. Thus the coefficients a_i and b_i rarely exceed unity. The net rate of reaction

$$r = r_F - r_R \quad \text{I-(4)}$$

is related to the disappearance of individual reactants and appearance of products by

$$r = -\frac{\rho}{a_1} \frac{dN_{A_1}}{dt} = -\frac{\rho}{a_2} \frac{dN_{A_2}}{dt} = \dots = \frac{\rho}{b_1} \frac{dN_{B_1}}{dt} = \frac{\rho}{b_2} \frac{dN_{B_2}}{dt} = \dots \quad \text{I-(5)}$$

where N_{A_1} , N_{A_2} , ..., N_{B_1} , N_{B_2} , ... represent the number of moles of A_1 , A_2 , ..., B_1 , B_2 , ... per unit mass of the mixture.*

*When the reaction proceeds at constant density, $\rho \frac{dN_i}{dt} = \frac{dC_i}{dt}$, and I-(5) may be written in the more familiar form

$$r = -\frac{1}{a_1} \frac{dC_{A_1}}{dt} = -\frac{1}{a_2} \frac{dC_{A_2}}{dt} = \dots = \frac{1}{b_1} \frac{dC_{B_1}}{dt} = \frac{1}{b_2} \frac{dC_{B_2}}{dt} = \dots$$

Since nozzle flows are not constant density processes, the more general form of Eq. (5) must be used.

The specific rate constants, k_F and k_R , are related in the following way. At equilibrium, the compositions must satisfy the equation

$$K_C(T) = \frac{C_{B_1}^{b_1} C_{B_2}^{b_2} \dots}{C_{A_1}^{a_1} C_{A_2}^{a_2} \dots} \quad \text{I-(6)}$$

and the forward and reverse rates of reaction are equal; that is,

$$r_F = r_R \quad \text{I-(7)}$$

hence, from I - (2), (3) and (6)

$$K_C(T) = \frac{k_F(T)}{k_R(T)} = \frac{C_{B_1}^{b_1} C_{B_2}^{b_2} \dots}{C_{A_1}^{a_1} C_{A_2}^{a_2} \dots} \quad \text{I-(8)}$$

Combining I - (2), (3), (4) and (8) gives an expression for the net reaction rate

$$r = k_F(T) \left[\frac{C_{A_1}^{a_1} C_{A_2}^{a_2} \dots}{K_C(T)} - \frac{C_{B_1}^{b_1} C_{B_2}^{b_2} \dots}{K_C(T)} \right] \quad \text{I-(9)}$$

Specific rate constants for many of the elementary reactions of interest are known or can be estimated to within an order of magnitude. The equilibrium constant, $K_C(T)$, may be calculated from the standard free-energy change of the reaction according to

$$K_C(T) = (RT)^{-\nu} K_p(T) = (RT)^{-\nu} \exp \left[\frac{-\Delta G^\circ(T)}{RT} \right] \quad \text{I-(10)}$$

where $\Delta G^\circ(T)$ is the standard Gibbs-free-energy change per mole and ν is the change in total number of moles

$$\nu = b_1 + b_2 + \dots - (a_1 + a_2 + \dots) \quad \text{I-(11)}$$

In general, high temperature gases undergoing expansion in a supersonic nozzle will never be in true chemical equilibrium as defined by I - (6) and (7) written for all possible elementary reactions. Because of changing temperature and pressure through the nozzle, a composition change may also be required in order to satisfy I - (6). This is inconsistent with I - (7), however, which implies a zero net rate for each reaction, and therefore constant composition. However, if the elementary chemical reactions in the system are able to proceed at a rate much greater than the rate of composition change required to satisfy I - (6), the system will be very close to true chemical equilibrium. In this case I - (6) and (7) will be very closely satisfied and

$$r_F \approx r_R \gg r \quad \text{I-(12)}$$

for each reaction in the system. For all practical purposes such a flow may be regarded as being in equilibrium, and will remain in equilibrium as long as Eq. I-(12) is satisfied.

If the reactions are only able to proceed at a rate much slower than the rate required to keep this system in equilibrium, the composition of the system will hardly change during the flow time. In this case the flow is said to be frozen, and for a reaction of the form of I - (1) written in the exothermic direction

$$R_F \gg r \approx r_F \gg r_R \quad \text{I-(13)}$$

where R_F is the reaction rate required to keep the flow in equilibrium.

Performance Calculation

The performance loss to be expected from chemical nonequilibrium effects in the nozzle may be predicted using the sudden-freezing approximation. Starting with an equilibrium solution of the flow which has been obtained using a suitable computer program, the calculation involves locating the freezing point and a subsequent frozen-flow calculation from that point on. Details of the calculation used in this study are presented below.

Over-all chemical reactions which are significant from an energy standpoint are selected using the equilibrium flow solution and suitable thermodynamic data. A detailed analysis of reaction mechanisms and kinetic data is then carried out using whatever information is available in order to find the elementary reaction step, or steps, which are rate controlling. The difficulties involved in doing this and locating the freezing point have been discussed. Assuming that a single rate-determining step can be found, the freezing point is then located from I - (4)

from the section, Sudden Freezing Approximation (page 5), presented in the body of the report where $(r_F)_{eq}$ is calculated from I - (2) written for the rate-determining step using equilibrium concentrations and temperature. The reaction rate required to keep the flow in equilibrium, R_F , is simply the rate at which any product of the rate-determining reaction is accumulating in the flow plus the rate at which the product is being consumed in any other reaction taking place. That is

$$R_F = \rho \left[\left(\frac{dN_p}{dt} \right)_{Flow} + \sum_{Reactions} \left(\frac{dN_p}{dt} \right) \right] \quad I-(14)$$

Since compositions are usually given as functions of area ratio, A/A^* , in equilibrium flow solutions, it is convenient to rewrite I - (14) introducing the velocity, $u = \frac{dx}{dt}$, and the rate of change of area ratio with axial distance, $\frac{A/A^*}{dx}$

$$R_F = \rho u \left(\frac{d(A/A^*)}{dx} \right) \left[\left(\frac{dN_p}{d(A/A^*)} \right)_{Flow} + \sum_{Reactions} \left(\frac{dN_p}{d(A/A^*)} \right) \right] \quad I-(15)$$

The required derivatives of composition with respect to area ratio may be computed from the equilibrium solution by graphical differentiation.

Because the chemical reaction rates are strong functions of temperature, $(r_F)_{eq}$ falls very rapidly through the nozzle and typically intersects the value of R_F at a large angle. The exact location of the freezing point and subsequent frozen flow calculation is thus quite insensitive to uncertainties in the kinetic rate data used. An uncertainty of a factor of five in the kinetic data will usually lead to an uncertainty of about one percent in the calculated gas velocity and I_{sp} values.

Once the freezing point has been located as described above, the solution is extended to higher area ratios by an exact frozen-flow calculation taking into account the variable gas specific heat. Such a calculation may be easily done by hand using available tables of thermodynamic data if temperature is chosen as the independent variable. A temperature T_1 is first chosen, which is the temperature at station 1, some point downstream from the freezing point. The gas velocity at station 1, u_1 , is calculated from the integrated form of the energy equation

$$u_1 = \sqrt{2 \left[h_0 - \sum a_{Fi} h_i(T_1) \right]} \quad I-(16)$$

where h_0 is the stagnation enthalpy, the a_{Fi} are frozen mass fractions, and the $h_i(T_1)$ are enthalpies of the species at temperature T_1 . The vacuum specific impulse is given by

$$I_{sp} = u_1 + \frac{\bar{R} T_1}{\bar{m} u_1} \quad \text{I-(17)}$$

where \bar{m} is the frozen molecular weight and \bar{R} is the universal gas constant. The pressure at station 1, P_1 , is calculated from an integrated form of the combined momentum and energy equations

$$\ln \frac{P_1}{P_F} = \frac{\bar{m}}{\bar{R}} \sum a_{Fi} \int_{T_F}^{T_1} \frac{c_{pi} dT}{T} \quad \text{I-(18)}$$

where the subscript F refers to freezing point conditions, and the c_{pi} are heat capacities at constant pressure of the species on a mass basis. The integrals in I - (18) may be evaluated most conveniently by taking differences in tabulated values of the standard entropies of the species. Written in terms of standard entropies, I - (18) becomes

$$\ln \frac{P_1}{P_F} = \frac{1}{\bar{R}} \sum x_{Fi} [S_i^0(T_1) - S_i^0(T_F)] \quad \text{I-(19)}$$

where the x_{Fi} are mole fractions at the freezing point, and $S_i^0(T)$ is the standard entropy of the i^{th} species at the temperature T . Knowing the temperature, pressure and velocity, the area ratio at station 1, $(A/A^*)_1$, is calculated from the continuity equation, which may be rearranged to give

$$(A/A^*)_1 = (A/A^*)_F \left(\frac{u_F}{u_1} \right) \left(\frac{P_F}{P_1} \right) \left(\frac{T_1}{T_F} \right) \quad \text{I-(20)}$$

Using the method described above, it is possible to calculate all the properties of the flow at any point downstream from the freezing point.

APPENDIX II

CRITERION FOR DEPARTURE FROM MOLECULAR VIBRATIONAL EQUILIBRIUM

The basic assumptions embodied in the analysis are:

1. The energy associated with the vibrational mode of the molecules is a small proportion of the total internal energy of the gas. Thus, variations in the energy of vibration will not significantly alter such properties as pressure, density and static temperature.
2. The vibrational energy of the molecules can be characterized by a temperature θ , the net rate of change of which is given by the equation:

$$\frac{d\theta}{dt} = \frac{T - \theta}{\tau} \quad \text{II-(1)}$$

where τ is a characteristic time for vibration.

3. There is no coupling between the rates of atomic recombination and molecular vibrational relaxation.

Certain other assumptions are implicit in II-(1). These are that the specific heat for the vibrational mode remains constant, and θ is equal to T when molecular vibration is fully adjusted. It is also assumed that the experimental values of τ , the relaxation time, reported in the literature (Refs. 32, 33, 34, 35, 36 and 37) can be corrected for temperature by application of the relationship $\log \text{time vs } T^{-1/2}$ is a straight line (Ref. 30).

From II-(1) it is seen that molecular vibration can never be completely adjusted because of such gradients as dT/dt , etc. and finite values of τ . Near equilibrium, however, the right-hand side of II-(1) is equal to the small difference between two large quantities. Thus for molecular vibration to be near equilibrium the following relationship must hold.

$$\left| \frac{d\theta}{dt} \right| \ll \frac{T}{\tau} \quad \text{II-(2)}$$

Well downstream of the nozzle throat where large discrepancies from vibrational equilibrium would occur it is expected that

$$T \ll \theta$$

$$\text{and} \quad \frac{d\theta}{dt} \approx - \frac{\theta}{\tau} \quad \text{II-(3)}$$

$$\text{or} \quad \left| \frac{d\theta}{dt} \right| \gg \frac{\tau}{\tau} \quad \text{II-(4)}$$

These two criteria can be summarized by defining a parameter

$$Q = \left| \frac{\tau/\tau}{d\theta/dt} \right| \quad \text{II-(5)}$$

where $Q \gg 1$ for vibrational equilibrium and $Q \ll 1$ at conditions well removed from equilibrium. It follows that significant departures from equilibrium are likely to occur when Q is of order unity. It has been suggested (Ref. 7) that Q is equal to 20 for a similar criterion to indicate when departures from chemical equilibrium are likely to occur in a reacting gas nozzle flow. The criterion given by II - (5) has also been evaluated with Q equal to 20 to indicate freezing of the vibrational modes. This criterion has been found satisfactory with Q equal to 20 and assuming

$$\frac{d\theta}{dt} = \frac{dT}{dt} \quad \text{II-(6)}$$

which is approximately true close to equilibrium.

Because vibrational relaxation effects are secondary to dissociation effects, refined calculations of vibrational equilibration are not warranted unless the recombination equilibrations are also included in the calculations. The recombination calculations would, of course, require the solution of a complex system of differential equations which describes the reactions in a flow system.

The criterion suggested above should give a suitable indication of whether or not vibrational effects are important for the expansion of combustion products. Since the vibrational modes are in equilibrium at the entrance to the nozzle, departures from equilibrium are at the least negligible up to the throat (Refs. 6 and 7). Therefore, the above criterion (II - (3)) can be applied with equilibrium conditions starting at the throat.

The II - (5) which expresses the criterion for freezing of vibrational relaxation is transformed to

$$Q = \left[(\tau/\tau) / v \left(\frac{dT}{d[A/A^*]} \right) \right] \left(\frac{2 \tan 15}{r_t} \right) \left(1 + \frac{\tan 15}{r_t} x \right) \quad \text{II-(7)}$$

B910056-12

for a steady flow and expansion in a conical nozzle with a 15 deg half-angle.

It will be noted from the above equations that all variables can be obtained from nozzle equilibrium calculations. The gradient, $dT/d[A/A^*]$, must be obtained by graphical differentiation of temperature vs area ratio curves.

APPENDIX III

CONSTANT VELOCITY AND THERMAL LAGS IN TWO PHASE FLOW

Neglecting radiation and variations in composition or specific heats and wall heat transfer and friction, and assuming noninteracting particles of negligible volume and uniform size, the equations of motion can be integrated for constant $\phi = u_p/u_g$ and $\theta = T_c - T_p/T_c - T_g$. The solution may be written (Refs. 5, 41 and 44)

$$\frac{A}{A_t} = \frac{A}{A^*} = \frac{1}{M} \left[\frac{2}{n+1} \left(1 + \frac{n-1}{2} \bar{M}^2 \right) \right]^{\frac{n+1}{2(n-1)}} \quad \text{III-(1)}$$

$$\frac{T_g}{T_c} = \left[1 + \frac{n-1}{2} \bar{M}^2 \right]^{-1} \quad \text{III-(2)}$$

$$\frac{P}{P_c} = \left[1 + \frac{n-1}{2} \bar{M}^2 \right]^{\frac{-n}{n-1}} \quad \text{III-(3)}$$

where

$$\bar{M}^2 = \frac{\gamma(1+Z\phi)}{n} M_g^2 \quad \text{III-(4)}$$

and

$$n = \left[1 - \frac{\gamma-1}{\gamma} \frac{(1+Z\phi^2)}{(1+Zr\theta)(1+Z\phi)} \right]^{-1} \quad \text{III-(5)}$$

The temperature ratio, θ , is uniquely related to ϕ by the equation*

$$\theta = \left[1 + \frac{1-\phi}{\phi} \frac{C_p Re}{4 Nu} Pr r \right]^{-1} \quad \text{III-(6)}$$

* It is necessary that $C_p Re / Nu$ be constant for θ to be constant as assumed. This is the case for Stokes flow and is also very nearly realized over a wide range of conditions encountered in rocket nozzles.

and the particle-gas velocity ratio, ϕ , is related to the nozzle throat geometry by the relation

$$Ry_t = \left(\frac{2}{n+1} \right)^2 \frac{n}{\gamma} \frac{a_{g_c}}{1+Z\phi} \left[\frac{16}{3} \frac{\rho_p r_p^2 \phi^2}{\mu_t (C_D Re)_t (1-\phi)} \right]^2 \quad \text{III-(7)}$$

The drag coefficient and Nusselt number for spherical particles is dependent on the particle Reynolds number and Mach number. For the present calculations the relations given in Ref. 41 were employed. Particle Reynolds number and Mach number in constant lag flow are given by

$$Re = \frac{\rho_g u_g (1-\phi) (2r_p)}{\mu}$$

$$= \frac{\rho_{g_c} a_{g_c} (1-\phi) (2r_p)}{\mu_c} \left(\frac{2}{n+1} \right)^{\frac{n+1}{2(n-1)}} \left[\frac{n}{\gamma(1+Z\phi)} \right]^{1/2} \frac{\mu}{\mu_c} \cdot \frac{1}{\epsilon} \quad \text{III-(8)}$$

$$M_p = M_g (1-\phi) = \bar{M} \left[\frac{n}{\gamma(1+Z\phi)} \right]^{1/2} (1-\phi) \quad \text{III-(9)}$$

For a given set of chamber conditions, particle properties, and throat geometry, the solution of III-(7) for ϕ is found by guessing values of ϕ until the calculated value of Ry_t is correct.

Finally, the decrease in c^* from the equilibrium value ($\phi = 1$) is related to ϕ by the equation

$$\frac{c_{eq}^* - c^*}{c_{eq}^*} = \frac{\Delta c^*}{c_{eq}^*} = 1 - \frac{\left[n^{1/2} \left(\frac{2}{n+1} \right)^{\frac{n+1}{2(n-1)}} \right]_{\phi=1}}{n^{1/2} \left(\frac{2}{n+1} \right)^{\frac{n+1}{2(n-1)}}} \left[\frac{1+Z\phi}{1+Z} \right]^{1/2} \quad \text{III-(10)}$$

APPENDIX IV

ANALYSIS OF HEAT TRANSFER RATES TO NOZZLE SURFACES
WITH FROZEN BOUNDARY LAYER FLOW

The problem of heat transfer to rocket nozzle walls is analyzed by considering the heat transfer rate to be the sum of two parts, the convective heat transfer rate, q_c , and the heat transfer due to recombination, q_D . For the case of the frozen boundary layer with low free-stream atomic species concentration, each of the heat transfers q_c and q_D may be computed independently and then added to obtain the total heat transfer

$$q_w = q_c + q_D \quad \text{IV-(1)}$$

The calculation of q_c and q_D is not as straightforward, however, since the concentration of atomic species in the boundary layer changes the enthalpy profile through the boundary layer and hence affects the calculation of q_c while the velocity profile affects the flux of atomic species toward the wall and hence affects the calculation of q_D . Each part of the total heat transfer is now considered in turn.

Convective Heat Transfer

A solution for the case of the laminar boundary layer on a flat plate with a catalytic wall is reported in Ref. 49. The solution is first obtained for a frozen flow, and the flow for a catalytic wall is then obtained by means of a series expansion about the frozen flow solution in terms of the concentration gradient at the wall. The general solution is necessarily nonsimilar due to the boundary conditions on the concentration gradient and hence is not easily extended to cases involving turbulent flow. The frozen flow solution is, however, a similar solution (i.e., the heat transfer and skin friction are not functions of distance along the plate but are determined solely from conditions within the profile) and hence should remain valid for turbulent flow when the proper values for the slope of the velocity and enthalpy profiles at the wall surface are substituted into the expression for the heat transfer rate. This is the approach employed in this analysis.

The heat transfer rate for a laminar frozen boundary layer is given in Ref. 49 as

$$q_c = - \frac{\mu_w}{2Pr} \sqrt{\frac{\rho_{w,0} u_\delta}{\mu_w x}} \rho_{*w} I_{w,0} \left(\frac{\partial I_*}{\partial \eta} \right)_w \quad \text{IV-(2)}$$

$$\rho_* = \frac{\rho}{\rho_{w,0}}$$

$$I_* = \frac{I}{I_{w,0}}$$

and η , the modified Dorodnitsyn variable, is given by

$$\eta = \frac{1}{2} \sqrt{\frac{\rho_{w,0} u_\delta}{\mu_w x}} \int_0^\infty \rho_* dy \quad \text{IV-(3)}$$

and the subscript $w,0$ denotes that the quantity is evaluated for the molecular species at the wall enthalpy and pressure for the condition of zero atomic species concentration. The frozen flow solutions for the slopes, enthalpy, and velocity profiles at the wall presented in Ref. 49 may be written as

$$\left(\frac{\partial I_*}{\partial \eta} \right)_w = - \left[1 - \frac{i_{M\delta}}{I_{w,0}} - \frac{u_\delta^2}{2gJ I_{w,0}} \right] \left(\frac{f_0''(\eta)}{2} \right)_w \quad \text{IV-(4)}$$

$$\left(\frac{\partial u}{\partial y} \right)_w = \frac{u_\delta}{2} \sqrt{\frac{\rho_{w,0} u_\delta}{\mu_w x}} \rho_{*w} \left(\frac{f_0''(\eta)}{2} \right)_w \quad \text{IV-(5)}$$

where f_0 is the Blasius function with η as defined by IV-(3). When $f_0''(\eta)$ is eliminated between IV-(4) and (5) and the resulting expression for the slope of the enthalpy gradient is substituted into IV-(2), the following result is obtained for the heat transfer rate:

$$q_c = \frac{\mu_w}{Pr} \frac{I_{w,0}}{u_\delta} \left[1 - \frac{i_{M\delta}}{I_{w,0}} - \frac{u_\delta^2}{2gJ I_{w,0}} \right] \left(\frac{\partial u}{\partial y} \right)_w \quad \text{IV-(6)}$$

The wall shearing stress for turbulent flow may now be written:

$$\tau_w = \frac{1}{2} C_f \rho_\delta u_\delta^2 = \mu_w \left(\frac{\partial u}{\partial y} \right)_w \quad \text{IV-(7)}$$

Hence:

$$\left(\frac{\partial u}{\partial y}\right)_w = \frac{C_f}{2} \left(\frac{\rho_\delta u_\delta^2}{\mu_w}\right) \quad \text{IV-(8)}$$

Equation IV-(8) is substituted into IV-(6) to yield the final expression for convective heat transfer in turbulent frozen flow:

$$q_c = \frac{C_f}{2Pr} \rho_\delta u_\delta I_{w,0} \left[1 - \frac{i_{M\delta}}{I_{w,0}} - \frac{u_\delta^2}{2gJI_{w,0}} \right] \quad \text{IV-(9)}$$

The skin friction coefficient in this expression is evaluated from the empirical logarithmic law using the Reynolds number based on the free-stream density and velocity and the viscosity evaluated at the wall temperature.

Heat Transfer Due to Wall Catalysis

The heat released to the wall due to catalytic recombination at the surface may be written

$$q_D = h_R j_w \quad \text{IV-(10)}$$

where h_R is the heat of recombination and j_w is the flux of atomic species at the wall. For a first order catalytic reaction (i.e., a cool wall), the flux of atomic species at the wall may be written:

$$j_w = \rho_w D_w \left(\frac{\partial c}{\partial y}\right)_w = k_w c_w \rho_w \quad \text{IV-(11)}$$

where D_w is the diffusion coefficient and k_w is the catalytic efficiency of the wall. If a dimensionless concentration is defined:

$$z(y) = \frac{c(y)}{c_\delta} \quad \text{IV-(12)}$$

the heat transfer rate may be written:

$$q_D = h_R k_w \rho_w c_\delta z(0) \quad \text{IV-(13)}$$

The dimensionless atomic species concentration must now be evaluated from the equation of continuity for the atomic species. This may be written:

$$\rho \left(u \frac{\partial z}{\partial x} + v \frac{\partial z}{\partial y} \right) = \frac{\partial}{\partial y} \left(\rho D \frac{\partial z}{\partial y} \right) \quad \text{IV-(14)}$$

If now a modified Dorodnitsyn transformation is introduced such that:

$$\eta = \frac{u_\delta(x)}{s^{1/2}} \int_0^y \rho dy \quad s = \int_0^x \rho_w \mu_w u_\delta(x) dx \quad \text{IV-(15)}$$

In addition a stream function, ψ , is introduced such that:

$$\rho u = \frac{\partial \psi}{\partial y} \quad \rho v = - \frac{\partial \psi}{\partial x} \quad \text{IV-(16)}$$

and a dimensionless stream function is then defined as

$$f(\eta, s) = \psi s^{-1/2} \quad \text{IV-(17)}$$

When the above substitutions are made in the continuity of species equation, the following equation is obtained:

$$s f' \frac{\partial z}{\partial s} - \frac{f}{2} \frac{\partial z}{\partial \eta} - \frac{\partial}{\partial \eta} \left[\frac{\ell}{Sc} \frac{\partial z}{\partial \eta} \right] = 0 \quad \text{IV-(18)}$$

where $f(\eta)$ is the dimensionless stream function which is equal to u/u_δ , the velocity profile, Sc is the Schmidt number, and ℓ is the ratio $\rho\mu/\rho_w\mu_w$.

Now, if flow with c_δ very small is considered, then the term $\frac{\partial z}{\partial s}$ may be dropped and the continuity equation may be written:

$$\frac{Sc}{2\ell} f z' + z'' = 0 \quad \text{IV-(19)}$$

so that f is independent of s and a similar solution is obtained. The solution may be obtained by defining

$$\lambda = \frac{\partial z}{\partial \eta} = z' \quad \text{IV-(20)}$$

and integrating twice to obtain:

$$1 - z(0) = z'(0) \int_0^{\infty} e^{-\frac{Sc}{2\lambda}} \int_0^{\lambda} f(\gamma) d\gamma d\lambda \quad \text{IV-(21)}$$

The integral has been evaluated by Pohlhausen as:

$$\int_0^{\infty} e^{-k \int_0^{\lambda} f(\gamma) d\gamma} d\lambda = 0.664 K^{1/3} \quad \text{IV-(22)}$$

when f is the Blasius function. The final solution may then be written:

$$z'(0) = 0.664 \left(\frac{Sc}{2\lambda} \right)^{1/3} [1 - z(0)] \quad \text{IV-(23)}$$

The boundary condition at the wall (IV-(11)) may now be written:

$$C_{\delta} \left(\frac{\partial z}{\partial y} \right)_w = \frac{k_w C_{\delta}}{D_w} z(0) \quad \text{IV-(24)}$$

which in the (η, s) coordinate system may be written:

$$z'(0) = \frac{s^{1/2}}{u_{\delta}} \frac{k_w}{\rho_w D_w} z(0) \quad \text{IV-(25)}$$

If the flow in the rocket nozzle is approximated by a linear velocity distribution such that

$$u_{\delta} = \beta x \quad \text{IV-(26)}$$

then:

$$s = \int_0^x \rho_w \mu_w u_{\delta}(x) dx = \rho_w \mu_w \frac{\beta x^2}{2} \quad \text{IV-(27)}$$

and the boundary condition becomes

$$z'(0) = \left(\frac{\rho_w \mu_w}{2\beta} \right)^{1/2} \frac{k_w}{\rho_w D_w} z(0) \quad \text{IV-(28)}$$

and hence from IV-(23)

$$z(0) = \frac{1}{\frac{1}{0.664} \left(\frac{Sc}{2\ell} \right)^{1/3} \left(\frac{\rho_w \mu_w}{2\beta} \right)^{1/2} \frac{k_w}{\rho_w D_w} + 1} \quad \text{IV-(29)}$$

Substituting the above expression into IV-(13), rearranging terms, and noting that for a cool wall $\ell \approx 1$, the heat transfer rate may be written:

$$q_D = 0.836 (2\beta \rho_w \mu_w)^{1/2} Sc^{-2/3} h_R C_\delta \phi \quad \text{IV-(30)}$$

where:

$$\phi = \frac{1}{1 + \frac{0.836 (2\beta \rho_w \mu_w)^{1/2} Sc^{-2/3}}{\rho_w k_w}} \quad \text{IV-(31)}$$

is the catalytic activity parameter. This term has the same form as that obtained in Ref. 48 where it is shown that for $k_w > 10^3$, $\phi \approx 1.0$.

APPENDIX V

EQUATION SYSTEM FOR THE FLOW OF A REACTING
GAS MIXTURE IN A ONE-DIMENSIONAL PASSAGE

The basic assumptions in the formulation of the physical model and equations that govern the nature of the flow of a reacting gas mixture in a one-dimensional passage are:

1. The mixture is one of thermally perfect gases.
2. The flow is inviscid throughout.
3. Transport properties can be neglected.
4. The internal energies are those pertaining to thermal equilibrium.
5. The law of mass action applies throughout.

The Gas Dynamic Equations

$$\text{Total mass conservation:} \quad \rho VA = \dot{m} \quad V-(1)$$

$$\text{Total energy conservation:} \quad H + \frac{v^2}{2gJ} = H_0 \quad V-(2)$$

$$H = \sum_{i=1}^n h_i \sigma_i \quad * \quad V-(2a)$$

$$h_i = \int_{T_b}^T c_{p_i} dT + (H_{f_i})_b \quad V-(2b)$$

$$\text{Momentum conservation:} \quad VV' + \frac{g}{\rho} P' = 0 \quad ** \quad V-(3)$$

$$\text{Equation of state:} \quad P = \rho RT \sum_{i=1}^n \sigma_i \quad V-(4)$$

* Unless noted, all summations are from $i = 1, \dots, n$.

** Prime values are derivatives with respect to h .

Speed of sound:
$$c = \sqrt{g \left(\frac{\partial P}{\partial \rho} \right)_{s, \sigma_1 \dots \sigma_n}} = \sqrt{g R T \sum \sigma_i \gamma}$$
 V-(5)

where γ is defined as:

$$\gamma = \frac{J \sum c_{p_i} \sigma_i}{J \sum c_{p_i} \sigma_i - R \sum \sigma_i}$$
 V-(5a)

Differentiate V-(4) and eliminate p' from V-(3)

$$V V' + \frac{g}{\rho} \left[\rho' R T \sum \sigma_i + \rho R T' \sum \sigma_i + \rho R T \sum \sigma_i' \right] = 0$$
 V-(6)

Differentiate V-(2) and from V-(3) and V-(4)

$$g J \left[\sum h_i \sigma_i' + T' \sum c_{p_i} \sigma_i \right] + V V' = 0$$
 V-(7)

Differentiate V-(1) and eliminate ρ'/ρ from V-(6)

$$V V' + g R T' \sum \sigma_i + g R T \sum \sigma_i' - g R T \sum \sigma_i \left(\frac{A'}{A} + \frac{V'}{V} \right) = 0$$
 V-(8)

Eliminate V' between V-(7) and V-(8)

$$T' = \frac{\frac{A'}{A} - \frac{\sum \sigma_i'}{\sum \sigma_i} + J \sum \sigma_i' h_i \left(\frac{1}{R T \sum \sigma_i} - \frac{g}{V^2} \right)}{J \sum c_{p_i} \sigma_i \left(\frac{g}{V^2} - \frac{1}{R T \sum \sigma_i} \right) + \frac{1}{T}}$$
 V-(9)

Define Mach number: $M^2 = \frac{V^2}{c^2}$ V-(10)

Combine Eqs. V-(10), V-(9), V-(2) and V-(5a)

$$T' = \frac{2(H_0 - H) \left(\frac{A'}{A} - \frac{\sum \sigma_i'}{\sum \sigma_i} \right) + \left(\frac{2(H_0 - H)}{T \sum \sigma_i c_{p_i}} + M^2 - 1 \right) \sum h_i \sigma_i'}{(1 - M^2) \sum c_{p_i} \sigma_i}$$
 V-(11)

The Reaction Kinetics Equations

Let n_r designate the total number of chemical reactions of the form:



Let n designate the total number of chemical species such as M_i of which n_a are the atomic species and $n - n_a$ are the number of molecular species, n_m . It follows that:

a'_{ij}, a''_{ij} are the stoichiometric coefficients of the i th species in the j th reaction, reactants and products, respectively.

k_{fj}, k_{bj} are the specific reaction rates of the forward and backward chemical changes in the j th reaction of the chemical system.

$j = 1, 2, \dots, n_r$ where n_r is the total number of chemical reactions.

Of the n_r chemical reactions the first n_m are independent, i.e., the matrix

$$\lambda = \left\{ \begin{array}{l} a''_{n_a+1,1} - a'_{n_a+1,1}, \dots, a''_{n,1} - a'_{n,1} \\ a''_{n_a+1,2} - a'_{n_a+1,2}, \dots, a''_{n,2} - a'_{n,1} \\ a''_{n_a+1,n_m} - a'_{n_a+1,n_m} \quad a''_{n,n_m} - a'_{n,n_m} \end{array} \right\} \quad V-(13)$$

is nonsingular. The remaining sets of stoichiometric coefficient differences may be expressed as linear combinations of these sets.

The atomic species continuity equations are given by:

$$\sigma_i + \sum_{j=n_a+1}^n \beta_{ij} \sigma_j = \text{constant} \quad (i = 1, 2, \dots, n_a) \quad V-(14)$$

where β_{ij} is the number of the i th atomic species in the j th molecular species.

The molecular species continuity equations are given by:

$$\rho v \sigma'_i = \sum_{j=1}^{n_r} (a''_{ij} - a'_{ij}) \left[K_{fj} \prod_{k=1}^n (\rho \sigma_k)^{a'_{kj}} - K_{bj} \prod_{k=1}^n (\rho \sigma_k)^{a''_{kj}} \right] \quad V-(15)$$

$i = n_0+1, n_0+2, \dots, n$

Equations V-(1), V-(2), V-(4), V-(10), V-(14), and V-(15) along with an area function can be integrated to specify the flow. There are certain numerical difficulties associated with the integration of this system which are discussed below.

Numerical Techniques

Two major difficulties exist in integrating the system of equations through a convergent-divergent nozzle that is flowing choked. These arise from the necessity of integrating through the sonic location and from the significant figure loss when the flow is near equilibrium.

The first problem is that integration through the throat involves a singularity in the flow equations. This can be seen in V-(11). In order for the temperature gradient to remain negative throughout the nozzle, the numerator must pass through zero at the same time as the denominator (at the sonic point). In general this point cannot be determined a priori, and if the calculation is allowed to proceed at will, either the nozzle will not choke or will not be able to contain the flow. In order to handle this problem directly on the machine, a second set of equations is used in the transonic region.

Equation V-(2) can be written

$$2gJ(H_0 - H) = M^2 \gamma g R T \sum \sigma_i \quad V-(16)$$

Differentiating this, and using V-(2a) and V-(2b), gives

$$T' = \frac{- \left(\frac{\sum h_i \sigma'_i}{H_0 - H} + \frac{2M'}{M} + \frac{\gamma \sum \sigma'_i}{\sum \sigma_i} - (\gamma - 1) \frac{\sum c_{p_i} \sigma'_i}{c_{p_i} \sigma_i} \right)}{\frac{1}{T} - (\gamma - 1) \frac{\sum c_{p_i} \sigma'_i}{\sum c_{p_i} \sigma_i} + \frac{2}{\gamma - 1} \frac{1}{TM^2}} \quad V-(17)$$

Combining V-(6) and (7) and solving for ρ'/ρ from

$$\frac{\rho'}{\rho} = \frac{T'}{T} \left(\frac{1}{\gamma-1} \right) - \frac{\sum \sigma_i'}{\sum \sigma_i} + \frac{J \sum h_i \sigma_i'}{RT \sum \sigma_i} \quad V-(18)$$

by specifying the Mach number distribution through the transonic region, and using V-(17) and (18) along with V-(1), (4), (14), and (15) the singularity problem is averted and a tool for multi-throat design is incorporated into the procedure.

The second difficulty encountered is in the expression for σ_i as given in V-(15). This equation introduces the possibility of serious loss in significant figures for any reaction which is nearly in equilibrium. In particular, the factor

$$K_{fJ} \prod_{k=1}^n (\rho \sigma_k)^{a'_{kJ}} - K_{bJ} \prod_{k=1}^n (\rho \sigma_k)^{a''_{kJ}} \quad V-(19)$$

will here involve the difference of two quantities of significant size whose difference is very small.

To avoid this loss in significant figures and to permit the initiation of the integration at equilibrium if desired, the variables λ_j are introduced, where

$$\lambda_j = K_{cJ} \prod_{i=1}^n (\rho \sigma_i)^{a'_{iJ} - a''_{iJ}} - 1 \quad j = 1, 2, \dots, n_r \quad V-(20)$$

and $K_{cJ} = K_{fJ} / K_{bJ}$ is the equilibrium constant for the j th reaction.

The reaction equations are separated into a (mathematically) independent set and a set dependent upon these. The quantities λ_j associated with the independent reactions are now introduced as dependent variables replacing quantities σ_j , associated with molecular species.

The differential equations (primes indicate differentials) for the reactions are replaced, for $j = 1, 2, \dots, n_m$ by

$$\frac{\lambda'_j}{1 + \lambda_j} = \frac{\rho'}{\rho} \sum_{i=1}^n (a'_{iJ} - a''_{iJ}) + \sum_{i=1}^n (a'_{iJ} - a''_{iJ}) \frac{\sigma'_i}{\sigma_i} + \frac{1}{K_{cJ}} \frac{dK_{cJ}}{dT} T' \quad V-(21)$$

$$j = 1, 2, \dots, n_m$$

where σ' is determined from

$$\rho \vee \sigma'_i = \sum_{j=1}^{n_r} (\alpha''_{ij} - \alpha'_{ij}) k_{bj} \prod_{k=1}^n (\rho \sigma_k)^{\alpha''_{kj}} \left(\rho \sum_{k=1}^n \sigma_k \right)^{\alpha''_{n+1,j}} \lambda_j \quad V-(22)$$

and

$$i = n_0 + 1, \dots, n$$

$$\sigma'_i = - \sum_{j=n_0+1}^n \beta_{ij} \sigma'_j, \quad i = 1, 2, \dots, n_0 \quad V-(23)$$

In order to capitalize upon the advantage afforded by the use of these dependent variables, a multistep integration procedure was employed which adjusts the integration step length to conform to a prescribed level of accuracy in the numerical solution. Thus the step is lengthened when the going is easy, shortened when the going is difficult.

Hamming's Predictor-Corrector Method (Ref. 51) was chosen because of its excellent stability and relative stability characteristics. The algorithm is as follows (Ref. 51) for the matrix differential equation

Predictor:

$$p_{n+1} = y_{n-3} + \frac{4h}{3} (2y'_n - y'_{n-1} + 2y'_{n-2}) \quad V-(24)$$

Modifier:

$$\begin{aligned} m_{n+1} &= p_{n+1} - \frac{112}{121} (p_n - c_n) \\ m'_{n+1} &= f(x_{n+1}, m_{n+1}) \end{aligned} \quad V-(25)$$

Corrector:

$$c_{n+1} = \frac{1}{8} [9y_n - y_{n-2} + 3h(m'_{n+1} + 2y'_n - y'_{n-1})] \quad V-(26)$$

Final Value:

$$y_{n+1} = c_{n+1} + \frac{9}{121} (p_{n+1} - c_{n+1}) \quad V-(27)$$

It is to be noted that, in addition to giving an estimate of error in the form of $P_n - C_n$, the method involves only two substitutions (evaluations of $f(x, y)$ per integration step as contrasted with the four required for the Runge-Kutta Fourth Order Method. This property by itself reduces the running time by one-half. Important additional checks on accumulated error are provided by the departure of the sum of the mass fractions from unity and the change in the mass flow rate. These parameters are quite sensitive to errors in the calculation.

The starting integration (the method requires initially four consecutive points on the solution curve to start) is performed by the Runge-Kutta Method. Simplified flow charts describing the machine program are shown on the following pages.

1-D-D SUBSONIC PROGRAM

(FIRST D.E. SYSTEM USED UNLESS OTHERWISE SPECIFIED)

I. THE COMBUSTION CHAMBER CONTOUR IS A STRAIGHT LINE, THE NOZZLE CONTOUR IS AN ARC OF A PARABOLA OR A SPLINE-FITTED CURVE. SEE PAGE 29. THE LENGTH OF THE COMBUSTION CHAMBER IS CONTROLLED BY INPUT AND TEMPERATURE GRADIENT.

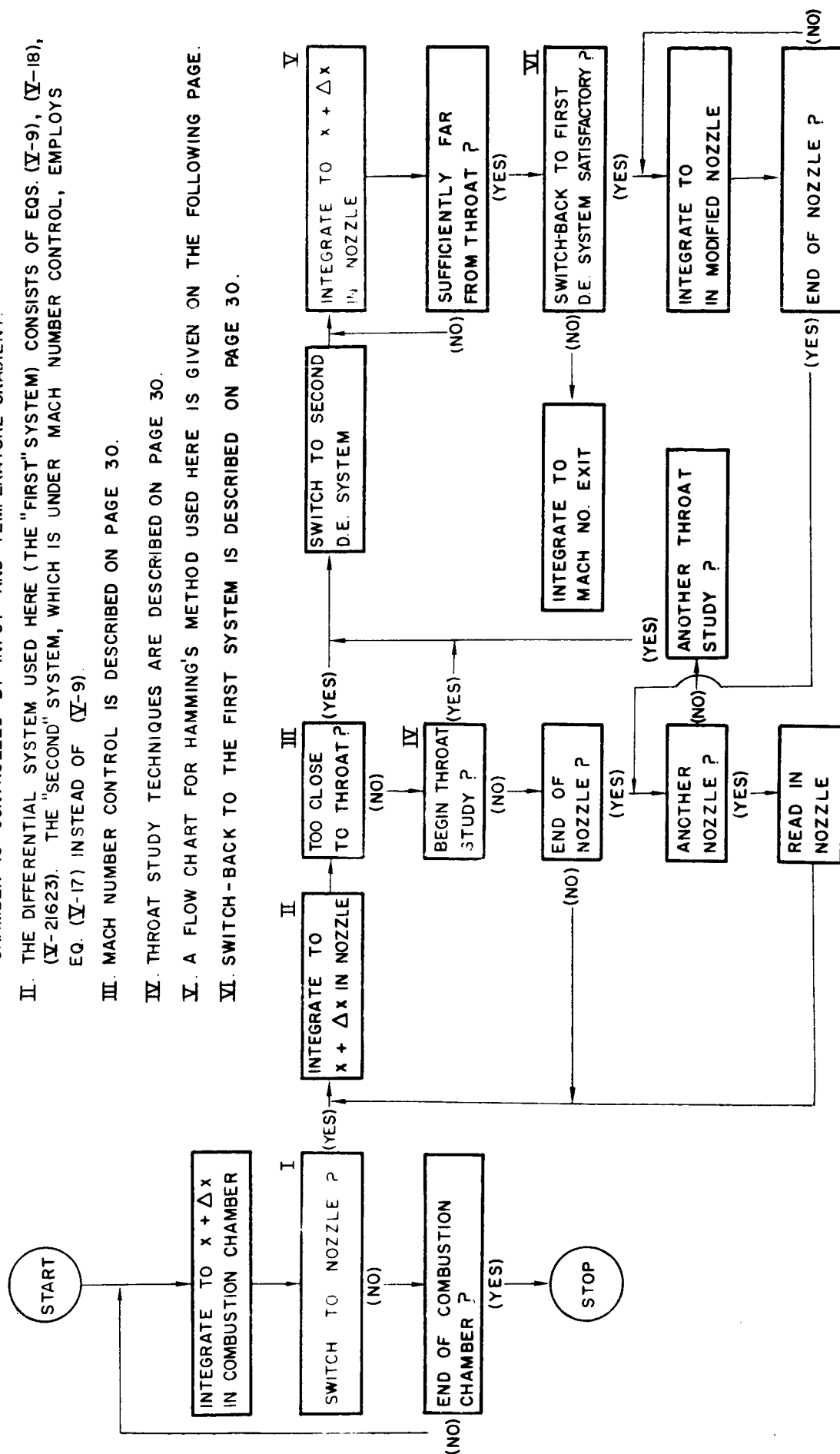
II. THE DIFFERENTIAL SYSTEM USED HERE (THE "FIRST" SYSTEM) CONSISTS OF EQS. (V-9), (V-18), (V-21623). THE "SECOND" SYSTEM, WHICH IS UNDER MACH NUMBER CONTROL, EMPLOYS EQ. (V-17) INSTEAD OF (V-9).

III. MACH NUMBER CONTROL IS DESCRIBED ON PAGE 30.

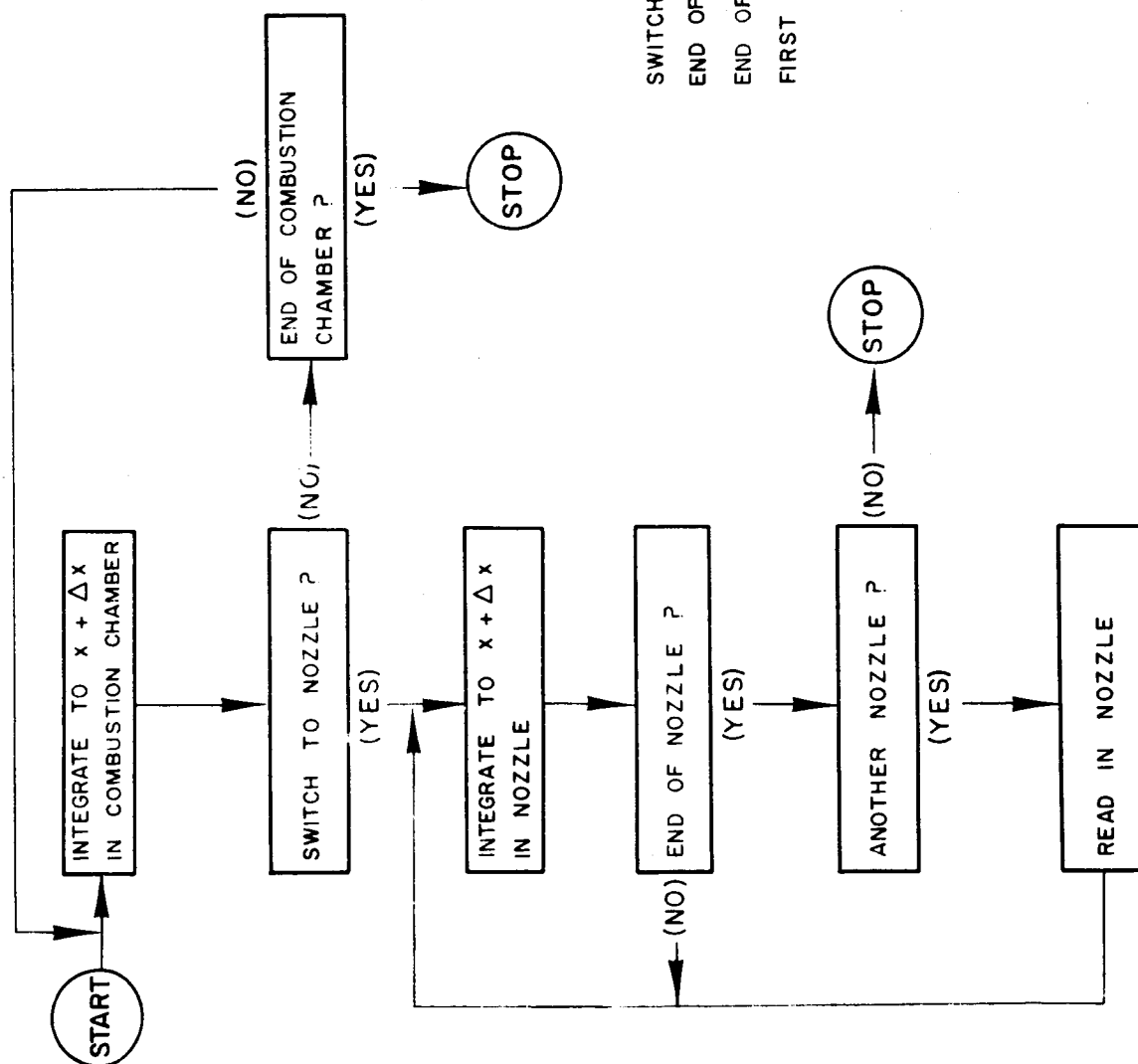
IV. THROAT STUDY TECHNIQUES ARE DESCRIBED ON PAGE 30.

V. A FLOW CHART FOR HAMMING'S METHOD USED HERE IS GIVEN ON THE FOLLOWING PAGE.

VI. SWITCH-BACK TO THE FIRST SYSTEM IS DESCRIBED ON PAGE 30.

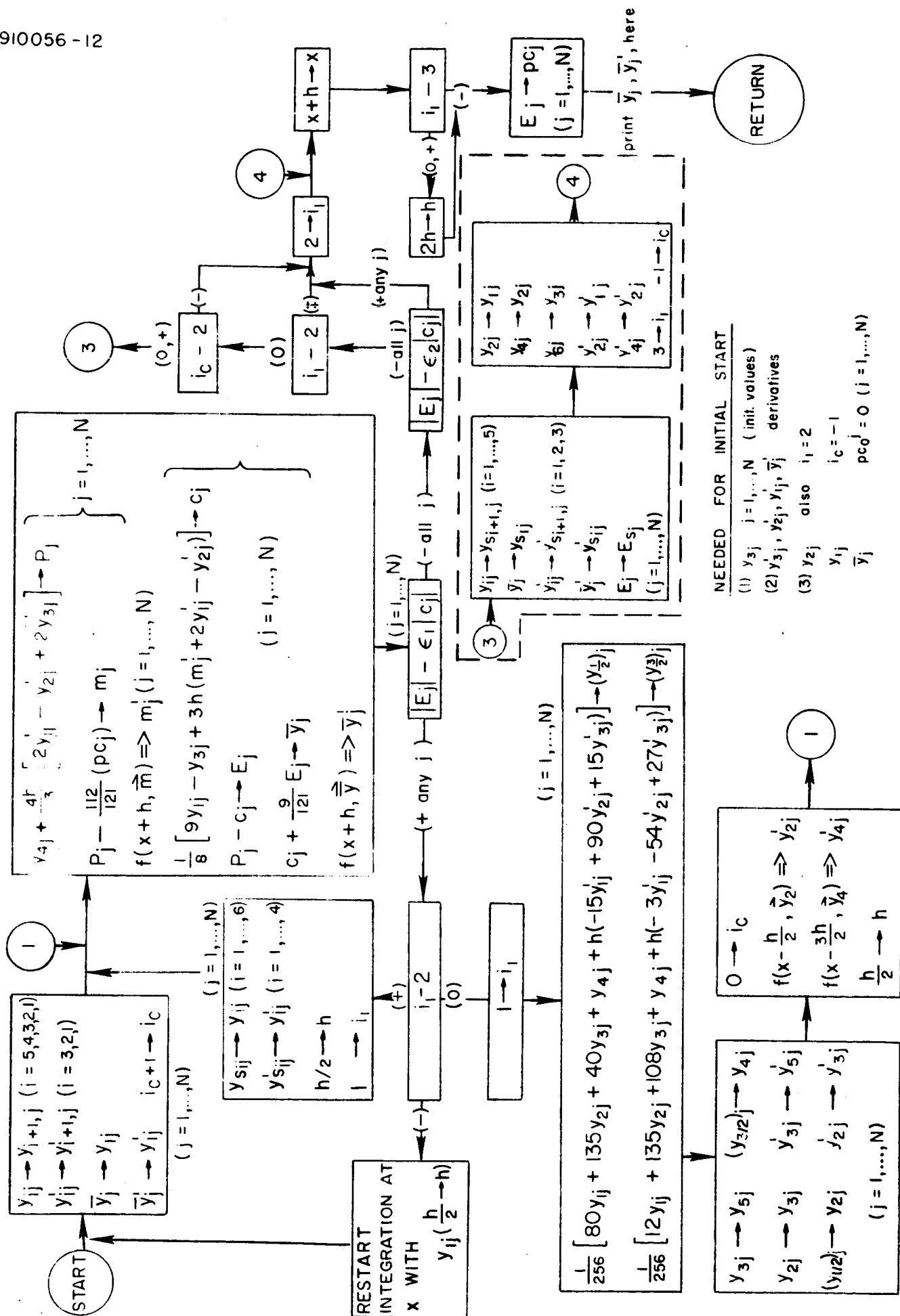


I-D SUPERSONIC PROGRAM



SWITCH TO NOZZLE CONTROLLED BY x , dt/dx
 END OF COMBUSTION CHAMBER CONTROLLED BY x, M
 END OF NOZZLE CONTROLLED BY x, M
 FIRST D.E. SYSTEM IN AT ALL TIMES

HAMMING'S METHOD



APPENDIX VI

THE METHOD OF CHARACTERISTICS FOR STEADY TWO-DIMENSIONAL
OR AXISYMMETRIC FLOW OF A REACTING GAS

The Equation System

Momentum:

$$u \frac{\partial u}{\partial x} + v \frac{\partial u}{\partial y} + \frac{g}{\rho} \frac{\partial p}{\partial x} = 0 \quad \text{VI-(1)}$$

$$u \frac{\partial v}{\partial x} + v \frac{\partial v}{\partial y} + \frac{g}{\rho} \frac{\partial p}{\partial y} = 0 \quad \text{VI-(2)}$$

Continuity:

$$\frac{1}{\rho} \left(u \frac{\partial \rho}{\partial x} + v \frac{\partial \rho}{\partial y} \right) + \frac{\partial u}{\partial x} + \frac{\partial v}{\partial y} + \epsilon \frac{v}{y} = 0 \quad \text{VI-(3)}$$

where $\epsilon = 0$ for plane flow, $\epsilon = 1$ for axisymmetric flow.

Energy:

$$H_t = H + \frac{1}{2} \frac{q^2}{gJ} \quad \text{VI-(4)}$$

where H_t is the total enthalpy.

State:

$$p = R \rho T \sum_{i=1}^n \sigma_i \quad \text{VI-(5)}$$

where σ_i is the concentration of the i^{th} species and n is the number of species.

Here

$$H = \sum_{i=1}^n h_i \sigma_i \quad \text{VI-(6)}$$

$$h_i = \int_{T_b}^T c_{p_i} dT + h_{f_i}(T_b) \quad \text{VI-(7)}$$

The quantity $h_{f_i}(T_b)$ is the heat of formation of the i^{th} constituent at temperature T_b .

Species Continuity:

$$\rho \left(u \frac{\partial \sigma_K}{\partial x} + v \frac{\partial \sigma_K}{\partial y} \right) = \zeta_K, \quad K = n_0 + 1, \dots, n \quad \text{VI-(8)}$$

(Here $\sigma_1, \sigma_2, \dots, \sigma_{n_0}$ refer to the atomic species, $\sigma_{n_0+1}, \sigma_{n_0+2}, \dots, \sigma_n$ refer to the molecular species.)

$$\zeta_K = \sum_{j=1}^{n_r} (\alpha_{Kj}'' - \alpha_{Kj}') \left[k_{fj} \prod_{i=1}^n (\rho \sigma_i)^{a_{ij}'} - k_{bj} \prod_{i=1}^n (\rho \sigma_i)^{a_{ij}''} \right] \quad \text{VI-(9)}$$

In addition there are the atomic species continuity equations

$$\sigma_i + \sum_{K=n_0+1}^n \beta_{iK} \sigma_K = \Gamma_i \quad (\text{CONSTANT}) \quad \text{VI-(10)}$$

where β_{iK} is the number of atoms of species i in one molecule of species

Transformation to Local Coordinates

Consider the coordinate system at point P with ξ -axis along the streamline and η normal to it (positive orientation for ξ, η). If θ is the angle of inclination of the streamline relative to the axis of symmetry,

$$\frac{\partial}{\partial \xi} \equiv \cos \theta \frac{\partial}{\partial x} + \sin \theta \frac{\partial}{\partial y} \equiv \frac{u}{q} \frac{\partial}{\partial x} + \frac{v}{q} \frac{\partial}{\partial y} \quad \text{VI-(11)}$$

$$\frac{\partial}{\partial \eta} \equiv -\sin \theta \frac{\partial}{\partial x} + \cos \theta \frac{\partial}{\partial y} \equiv -\frac{v}{q} \frac{\partial}{\partial x} + \frac{u}{q} \frac{\partial}{\partial y} \quad \text{VI-(12)}$$

The system of equations becomes

$$q \frac{\partial q}{\partial \xi} + \frac{g}{\rho} \frac{\partial \rho}{\partial \xi} = 0 \quad \text{VI-(13)}$$

$$q^2 \frac{\partial \theta}{\partial \xi} + \frac{g}{\rho} \frac{\partial \rho}{\partial y} = 0 \quad \text{VI-(14)}$$

$$\frac{q}{\rho} \frac{\partial \rho}{\partial \xi} + \frac{\partial q}{\partial \xi} + q \frac{\partial \theta}{\partial y} + \frac{\epsilon q \sin \theta}{y} = 0 \quad \text{VI-(15)}$$

together with Eqs. VI-(4) through VI-(10). Equation VI-(8) is here

$$\rho q \frac{\partial \sigma_k}{\partial \xi} = \zeta_k, \quad k = n_0 + 1, \dots, n \quad \text{VI-(16)}$$

Reduction of the Equation System

The equation system is now simplified in the following way. Equation VI-(14) provides a relation between the tangential and normal derivatives of θ and ρ . A second such relation is obtained by eliminating the derivatives in q and ρ from VI-(15) using VI-(13) and VI-(4) through VI-(7).

From VI-(5)

$$dp = R \rho T \sum_{i=1}^n d\sigma_i + R \sum_{i=1}^n \sigma_i (\rho dT + T d\rho) \quad \text{VI-(17)}$$

and from V-(4), V-(6), V-(7)

$$\sum_{i=1}^n h_i d\sigma_i + \sum_{j=1}^n \sigma_j c_{pj} \left[\frac{dp - R \rho T \sum_{i=1}^n d\sigma_i}{R \rho \sum_{i=1}^n \sigma_i} - \frac{T}{\rho} d\rho \right] + \frac{q dq}{g J} = 0 \quad \text{VI-(18)}$$

or

$$\frac{q dq}{gJ} + \frac{\sum_i \sigma_i c_{p_i}}{R \rho \sum_i \sigma_i} dp - \frac{\tau \sum_i \sigma_i c_{p_i}}{\rho} d\rho + \sum_j \left[h_j - \frac{\sum_i \sigma_i c_{p_i}}{\sum_i \sigma_i} \tau \right] d\sigma_j = 0 \quad \text{VI-(19)}$$

It is subsequently developed that the sound speed involved in this analysis is the local-frozen-composition sound speed. For the present, define the ratio of specific heats,

$$\gamma = \frac{\sum_i \sigma_i c_{p_i}}{\sum_i \sigma_i c_{v_i} - \frac{R}{J} \sum_i \sigma_i} \quad \text{VI-(20)}$$

and the sound speed,

$$c^2 = \gamma g \frac{p}{\rho} \quad \text{VI-(21)}$$

Then VI-(19) becomes

$$\frac{q dq}{gJ} + \frac{1}{\rho J} \frac{\gamma}{\gamma-1} dp - \frac{c^2 d\rho}{\rho gJ(\gamma-1)} + \sum_{j=1}^n \left[h_j - \frac{c^2}{gJ(\gamma-1) \sum_i \sigma_i} \right] d\sigma_j = 0 \quad \text{VI-(22)}$$

We have, from VI-(8),

$$q \frac{\partial \sigma_K}{\partial \xi} = \frac{\zeta_K}{\rho}, \quad K = n_a + 1, \dots, n \quad \text{VI-(23)}$$

If we define, for $K = 1, 2, \dots, n_a$

$$\zeta_K = - \sum_{i=n_a+1}^n \beta_{K_i} \zeta_i, \quad \text{VI-(24)}$$

then by VI-(10) we may use VI-(23) for $K = 1, 2, \dots, n$. Eq. V-(22) implies then that

$$\frac{q}{gJ} \frac{\partial q}{\partial \xi} + \frac{1}{\rho J} \frac{\gamma}{\gamma-1} \frac{\partial p}{\partial \xi} - \frac{c^2}{\rho gJ(\gamma-1)} \frac{\partial \rho}{\partial \xi} + \sum_{j=1}^n \left[h_j - \frac{c^2}{gJ(\gamma-1) \sum_i \sigma_i} \right] \frac{\zeta_j}{\rho q} = 0 \quad \text{VI-(25)}$$

Form now

$$- \left[\frac{q^2}{gJ} + \frac{c^2}{gJ(\gamma-1)} \right] [\text{EQ.VI-(13)}] + \left[\frac{qc^2}{gJ(\gamma-1)} \right] [\text{EQ.VI-(15)}] + q^2 [\text{EQ.VI-(25)}]$$

and obtain, with $M^2 = q^2/c^2$,

$$g \frac{M^2-1}{\rho q^2} \frac{\partial \rho}{\partial \xi} + \frac{\partial \theta}{\partial \eta} + \frac{\epsilon \sin \theta}{y} + \sum_{j=1}^n \left[\frac{h_j g J(\gamma-1)}{c^2} - \frac{1}{\sum_i \sigma_i} \right] \frac{\zeta_j}{\rho q} = 0 \quad \text{VI-(26)}$$

A final equation is obtained eliminating $\partial q/\partial \xi$ between VI-(25) and VI-(13).

$$\frac{\partial \rho}{\partial \xi} = \frac{g}{c^2} \frac{\partial \rho}{\partial \xi} + \sum_{j=1}^n \left[\frac{g J(\gamma-1) h_j}{c^2} - \frac{1}{\sum_i \sigma_i} \right] \frac{\zeta_j}{q} \quad \text{VI-(27)}$$

Collecting VI-(13), (14), (16), (26), and (27) we have the equation system.

From VI-(14)

$$\gamma M^2 \frac{\partial \theta}{\partial \xi} + \frac{\partial \log p}{\partial \eta} = 0 \quad \text{VI-(28)}$$

From VI-(26)

$$\frac{M^2-1}{\gamma M^2} \frac{\partial \log p}{\partial \xi} + \frac{\partial \theta}{\partial \eta} + \frac{\epsilon \sin \theta}{y} + \sum_{j=1}^n \left[\frac{h_j g J(\gamma-1)}{c^2} - \frac{1}{\sum_i \sigma_i} \right] \frac{\zeta_j}{\rho q} = 0 \quad \text{VI-(29)}$$

From VI-(13)

$$\frac{\gamma q}{c^2} \frac{\partial q}{\partial \xi} + \frac{\partial \log p}{\partial \xi} = 0 \quad \text{VI-(30)}$$

From VI-(27)

$$\frac{\partial \rho}{\partial \xi} - \frac{g}{c^2} \frac{\partial \rho}{\partial \xi} - \sum_{j=1}^n \left[\frac{h_j g J(\gamma-1)}{c^2} - \frac{1}{\sum_i \sigma_i} \right] \frac{\zeta_j}{q} = 0 \quad \text{VI-(31)}$$

Finally, from VI-(24)

$$q \frac{\partial \sigma_K}{\partial \xi} = \frac{\xi_K}{\rho}, \quad K = 1, 2, \dots, n \quad \text{VI-(32)}$$

The Characteristic Equations

It is evident from this form of the equation system that the stream line is an $(n + 2)$ -fold characteristic. The two remaining characteristic directions at a given point may be determined directly from VI-(28) and VI-(29). Form

$$\lambda_1 \left\{ \gamma M^2 \frac{\partial \theta}{\partial \xi} + \frac{\partial \log p}{\partial y} \right\} + \lambda_2 \left\{ \frac{M^2 - 1}{\gamma M^2} \frac{\partial \log p}{\partial \xi} + \frac{\partial \theta}{\partial y} + \frac{\epsilon \sin \theta}{y} + \sum_{j=1}^n \left[\frac{h_j g J(\gamma - 1)}{c^2} - \frac{1}{\sum_i \sigma_i} \right] \frac{\xi_j}{\rho q} \right\} = 0 \quad \text{VI-(33)}$$

If $\phi(\xi, \eta) = 0$ is a characteristic curve at the point in question, then it is necessary and sufficient that $\lambda_1, \lambda_2 \neq 0$, 0 be found such that the directional derivatives of $\log p$ and θ involved be both in a direction tangent to this characteristic. Thus

$$\lambda_1 \gamma M^2 \phi_\xi + \lambda_1 \phi_y = 0 \quad \text{VI-(34)}$$

$$\lambda_1 \phi_n + \lambda_2 \frac{M^2 - 1}{\gamma M^2} \phi_\xi = 0 \quad \text{VI-(35)}$$

so that

$$(M^2 - 1) \phi_\xi^2 - \phi_n^2 = 0 \quad \text{VI-(36)}$$

The characteristic directions are thus given by

$$\frac{\partial y}{\partial \xi} = - \frac{\phi_\xi}{\phi_n} = \frac{\pm 1}{\sqrt{M^2 - 1}} \quad \text{VI-(37)}$$

The consistency condition along a characteristic curve is obtained merely by making a selection of and substituting into VI-(33):

$$\frac{\lambda_1}{\lambda_2} = - \frac{1}{\gamma M^2} \frac{\phi_n}{\phi_\xi} = \pm \frac{\sqrt{M^2 - 1}}{\gamma M^2} \quad \text{VI-(38)}$$

Note that the unit vectors along the characteristic directions are

$$\frac{\sqrt{M^2-1}}{M}, \quad \frac{\pm 1}{M},$$

so that the corresponding direction derivative operators are

$$\frac{\sqrt{M^2-1}}{M} \frac{\partial}{\partial \xi} \pm \frac{1}{M} \frac{\partial}{\partial \eta} \equiv \frac{\partial}{\partial s} \quad \text{VI-(39)}$$

where s indicates arc length.

Equation VI-(33) becomes

$$\frac{\sqrt{M^2-1}}{\gamma M} \left(\frac{\sqrt{M^2-1}}{M} \frac{\partial \log p}{\partial \xi} \pm \frac{1}{M} \frac{\partial \log p}{\partial \eta} \right) \pm M \left(\frac{\sqrt{M^2-1}}{M} \frac{\partial \theta}{\partial \xi} \pm \frac{1}{M} \frac{\partial \theta}{\partial \eta} \right) +$$

$$\frac{\epsilon \sin \theta}{y} + \sum_{j=1}^n \left[\frac{h_j g J(\gamma-1)}{c^2} - \frac{1}{\sum_i \sigma_i} \right] \frac{\zeta_j}{\rho q} = 0 \quad \text{VI-(40)}$$

or, in differential form along the Mach lines,

$$\frac{\sqrt{M^2-1}}{\gamma M^2} d \log p \pm d\theta + \left\{ \frac{\epsilon \sin \theta}{y} + \sum_{j=1}^n \left[\frac{h_j g J(\gamma-1)}{c^2} - \frac{1}{\sum_i \sigma_i} \right] \frac{\zeta_j}{\rho q} \right\} \frac{ds}{M} = 0 \quad \text{VI-(41)}$$

Return now to the x - y system of coordinates. For convenience we set $\alpha = \sin^{-1} 1/M$, $A = \tan \alpha$, $t = \tan \theta$. Then we have for the Mach line equations

$$dy = \tan(\theta \pm \alpha) dx = \frac{t \pm A}{1 \mp At} dx \quad \text{VI-(42)}$$

$$\frac{\sqrt{M^2-1}}{\gamma M^2} d \log p \pm \frac{dt}{1+t^2} + \left\{ \frac{\epsilon t}{y} + \sqrt{1+t^2} \sum_{j=1}^n \left[\frac{h_j g J(\gamma-1)}{c^2} - \frac{1}{\sum_i \sigma_i} \right] \frac{\zeta_j}{\rho q} \right\} \frac{A dx}{1 \mp At} = 0 \quad \text{VI-(43)}$$

inasmuch as

$$\frac{dS}{M} = \frac{\sin \alpha dx}{\cos(\theta \pm \alpha)} = \frac{A\sqrt{1+t^2}}{1 \pm At} dx \quad \text{VI-(44)}$$

The method of characteristics is thus based upon the following set of characteristic equations:

Up Mach Line:

$$dy = \frac{t+A}{1-At} dx \quad \text{VI-(45)}$$

$$\frac{\sqrt{M^2-1}}{\gamma M^2} d \log p + \frac{dt}{1+t^2} + \left\{ \frac{\epsilon t}{y} + \sqrt{1+t^2} \sum_{j=1}^n \left[\frac{h_j g J(\gamma-1)}{c^2} - \frac{1}{\sum \sigma_i} \right] \frac{\xi_j}{\rho q} \right\} \frac{Adx}{1-At} = 0 \quad \text{VI-(46)}$$

Down Mach Line:

$$dy = \frac{t-A}{1-At} dx \quad \text{VI-(47)}$$

$$\frac{\sqrt{M^2-1}}{\gamma M^2} d \log p - \frac{dt}{1+t^2} + \left\{ \frac{\epsilon t}{y} + \sqrt{1+t^2} \left[\sum_{j=1}^n \frac{h_j g J(\gamma-1)}{c^2} - \frac{1}{\sum \sigma_i} \right] \frac{\xi_j}{\rho q} \right\} \frac{Adx}{1+At} = 0 \quad \text{VI-(48)}$$

Stream line

$$d \log p = \frac{1}{\gamma} d \log p + \sum_{j=1}^n \left[\frac{h_j g J(\gamma-1)}{c^2} - \frac{1}{\sum \sigma_i} \right] \frac{\xi_j}{\rho q} \sqrt{1+t^2} dx \quad \text{VI-(49)}$$

$$dq^2 = -\frac{2}{\gamma} c^2 d \log p \quad \text{VI-(50)}$$

$$d \sigma_i = (\xi_i / \rho q) \sqrt{1+t^2} dx \quad i = 1, 2, \dots, n \quad \text{VI-(51)}$$

Note that the summation terms in Eqs. VI-46, VI-48, and VI-50 may be expressed in terms of process gamma, $\gamma_p = \left(\frac{d \ln p}{d \ln \rho} \right)_\psi$, taken along streamlines. In fact

$$\sum_{j=1}^n \left[\frac{h_j g J(\gamma-1)}{c^2} - \frac{1}{\sum_i \sigma_i} \right] \frac{\xi_j}{\rho q} = \frac{2 \log \rho}{2\xi} - \frac{1}{\gamma} \frac{2 \log p}{2\xi} \quad \text{VI-(52)}$$

$$= \frac{2 \log \rho}{2\xi} \left[1 - \frac{\gamma_p}{\gamma} \right]$$

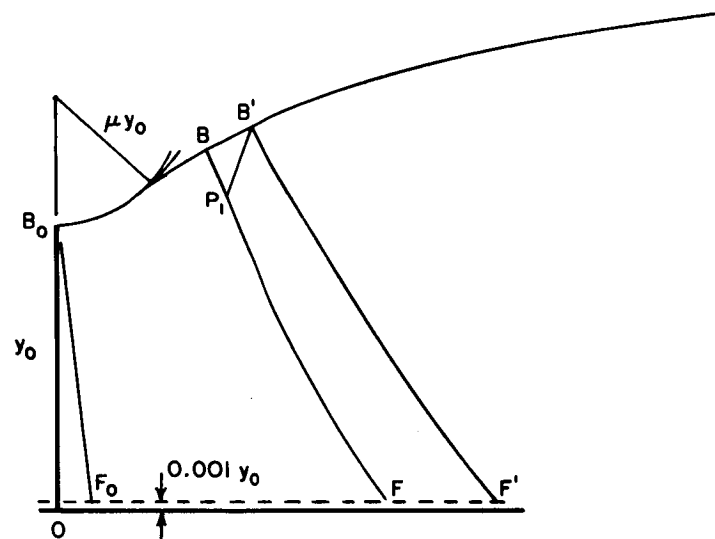
Since the size of this term in these characteristic equations marks the extent of the departure from a frozen composition construction, the magnitude of the quantity $1 - (\gamma_p/\gamma)$ may be used as a measure of the degree of freezing in the chemical reactions.

APPENDIX VII

METHOD OF CHARACTERISTICS: NUMERICAL CONSTRUCTION

Initial Mach Line

There are $N_c + 1$ equally spaced mesh points taken on the initial down Mach line which are used to begin the characteristics mesh construction. Of these, every N_p th will initiate a principal streamline along which the reaction kinetics equations are integrated (N_c is a multiple of N_p).



1.) BASIC NOZZLE CONFIGURATION

No point is used as the axis itself in view of the singularity for $y = 0$ in the axisymmetric case. A cylinder of radius $0.001 y_0$ ($y_0 =$ throat radius) is placed around the axis of symmetry in both two-dimensional and axisymmetric cases and taken to be a bounding surface of the flow. (It has been determined that this device permits approximating the proper solution to a high degree of accuracy and eliminates the instabilities and error in conventional axis constructions.)

The properties for the initial down Mach line are obtained from a one-dimensional analysis. The equations for the down Mach line (see Eq. VI-47, 48) are integrated by the Runge Kutta method to give the initial flow inclination and the Mach line configuration itself. The mesh points are obtained at approximately uniformly distributed radial distances (uniformly with respect to $\sqrt{\frac{\psi}{\psi_0}}$ where the stream function ψ is given by Eq. VII-15).

$$\left[\frac{0.999 y_0}{A_0} (1 - K/N_c), (0.001 + 0.999 K/N_c) y_0 \right], \quad K = 0, 1, \dots, N_c$$

VII-(1)

The dimensionless stream function ψ/ψ_{TOT} (ψ_{TOT} is the total mass flow across B_0F_0) at these principal streamline points is given by

$$\frac{\psi_K}{\psi_{tot}} \begin{cases} \frac{K N_p}{N_c} & \text{IF } \epsilon = 0 \\ \frac{K N_p}{1.001 N_c} (0.002 + 0.999 K N_p / N_c) & \text{IF } \epsilon = 1 \end{cases} \quad \text{VII-(2)}$$

$$K = 0, (N_c/N_p), 2(N_c/N_p), \dots, N_p$$

Information on a Mach Line

At each mesh point on a down Mach line is stored the following information

$$x, y, p, t, \rho, q, c^2, A, \psi, X$$

where

$$\begin{aligned} X &= \sqrt{1+t^2} \frac{\bar{X}}{q} = \sum_{j=1}^n \left[\frac{h_j g J(\gamma-1)}{c^2} - \frac{1}{\sum_i \sigma_i} \right] \frac{\xi_j}{q} \sqrt{1+t^2} \\ &= \sqrt{1+t^2} \left(\frac{d \log \rho}{d \xi} \right) \left[1 - (\gamma_p/\gamma) \right] \end{aligned} \quad \text{VII-(3)}$$

is used in the consistency relations along Mach lines. At each principal streamline point is stored

$$x, y, p, t, \rho, q, \sigma_1, \sigma_2, \dots, \sigma_n, \gamma$$

In addition, along this down Mach line are stored coefficients for spline fits (Refs. 57, 68) to be employed in the interpolation for the various characteristics constructions. These include fits against the dimensionless stream function of

$$x, p, q, \rho, X, c^2$$

It is here merely noted that the spline fit is a piecewise cubic curve of interpolation, the cubic segments being joined at the tabulated data points with slope and curvature continuous at these points (Ref. 67).

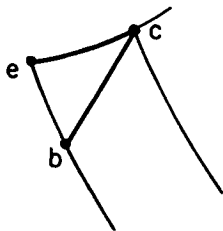
Construction of Mach Line

It is assumed here that the prescribed information is known along the Mach line BF (Figure of Basic Nozzle Configuration) and it is desired to construct a next Mach line B'F'. The point B' is first constructed based upon the mesh point p_1 , next below B on BF. (A restriction is placed upon the amount of contour turning between B and B'; if this restriction is exceeded, a point \tilde{p} is interpolated between B and p_1 , and \tilde{p} used in place of p_1). Next, in a series of "interior point" constructions, the successive mesh points on B'F' are determined. The final "axis construction" determines the point F' on the axis cylinder.

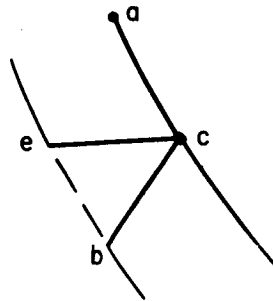
The Mach line construction is here distinguished from the integration of the reaction kinetics equations along principal streamlines. These two processes are used alternately to constitute the complete iterative cycle for the final determination of B'F'.

(a) The Characteristics Equations

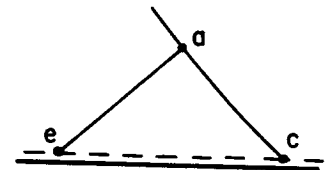
2.) MACH NET CONSTRUCTION



A.) BOUNDARY POINT



B.) INTERIOR POINT



C.) AXIS POINT

The characteristics equations are set forth in iterative form, the schematics (see Mach Net Construction) indicating the point designation scheme: point c is to be determined, bc is an up Mach line, ac is a down Mach line, ec is a streamline segment. The point $c^{(K)}$ represents the K^{th} approximation to c, etc.

Up Mach Line ($c^{(0)} = b$)

$$y_{c(K)} - y_b = \frac{1}{2} \left[(M_u)_b + (M_u)_{c^{(K-1)}} \right] (x_{c(K)} - x_b) \quad \text{VII-(4)}$$

$$\frac{1}{2} \left[N_b + N_{c^{(K-1)}} \right] (p_{c(K)} - p_b) + (t_{c(K)} - t_b) = - \frac{1}{2} \left[(L_u)_b + (L_u)_{c^{(K-1)}} \right] (x_{c(K)} - x_b) \quad \text{VII-(5)}$$

Down Mach Line $(c^{(0)} = a)$

$$y_{c(k)} - y_a = \frac{1}{2} \left[(M_D)_a + (M_D)_{c(k-1)} \right] (x_{c(k)} - x_a) \quad \text{VII-(6)}$$

$$\frac{1}{2} \left[N_a + N_{c(k-1)} \right] (p_{c(k)} - p_a) - (t_{c(k)} - t_a) = - \frac{1}{2} \left[(L_D)_a + (L_D)_{c(k-1)} \right] (x_{c(k)} - x_a) \quad \text{VII-(7)}$$

Streamline $(c^{(0)} = e^{(1)})$

$$\rho_{c(k)} - \rho_{e(k)} = \frac{1}{2} \left[\left(\frac{g}{c^2} \right)_{e(k)} + \left(\frac{g}{c^2} \right)_{c(k-1)} \right] (p_{c(k)} - p_{e(k)}) + \frac{1}{2} \left[X_{e(k)} + X_{c(k-1)} \right] (x_{c(k)} - x_{e(k)}) \quad \text{VII-(8)}$$

$$q_{c(k)} - q_{e(k)} = - \frac{1}{2} \left[\left(\frac{q}{\rho q} \right)_{e(k)} + \left(\frac{q}{\rho q} \right)_{c(k-1)} \right] (p_{c(k)} - p_{e(k)}) \quad \text{VII-(9)}$$

where

$$M_u = \frac{t+A}{1-A t}, \quad M_D = \frac{t-A}{1+A t}, \quad N = \frac{g(1+t^2)}{\rho q^2 A} \quad \text{VII-(10)}$$

$$L_u = \left[\frac{\epsilon t}{y} + \frac{X}{\rho} \right] \frac{A}{1-A t} (1+t^2), \quad \text{VII-(11)}$$

$$L_D = \left[\frac{\epsilon t}{y} + \frac{X}{\rho} \right] \frac{A}{1+A t} (1+t^2) \quad \text{VII-(12)}$$

(b) Interior Point Construction

Equations VII-(4) and VII-(6) yield $x_c^{(k)}$, $y_c^{(k)}$. Then VII-(5) and VII-(7) give $p_c^{(k)}$ and $t_c^{(k)}$ (see schematic of Interior Point). Equations VII-(8) and VII-(9) now yield $\rho_c^{(k)}$ and $q_c^{(k)}$ when properties at $e^{(k)}$ are determined by interpolation.

It is required to evaluate at $e^{(K)}$ the quantities ρ, q, ψ, p, c^2, X . These are obtained by interpolation using the spline fits referred to with the value of the dimensionless stream function at $e^{(K)}$ and $c^{(K)}$ taken as

$$\frac{\psi_{c^{(K)}}}{\psi_{B'}} = \frac{\psi_{c^{(K)}}}{\psi_B} \frac{1}{2} \left\{ \frac{\psi_a}{\psi_{B'}} + \frac{1}{2} \left[\left(\frac{p_D}{\psi_{B'}} \right)_a + \left(\frac{p_D}{\psi_{B'}} \right)_{c^{(K-1)}} \right] (x_{c^{(K)}} - x_a) + \frac{\psi_b}{\psi_B} + \frac{1}{2} \left[\left(\frac{p_u}{\psi_B} \right)_b + \left(\frac{p_u}{\psi_B} \right)_{c^{(K-1)}} \right] (x_{c^{(K)}} - x_b) \right\} \quad \text{VII-(13)}$$

(In the right-hand member, $c^{(0)} = a$ and $c^{(0)} = b$, respectively.) Here along an up Mach line

$$\frac{d\psi}{dx} = (2\pi y)^\epsilon \rho q \frac{A\sqrt{1+t^2}}{1-A\uparrow} \equiv p_u \quad \text{VII-(14)}$$

and along a down Mach line

$$\frac{d\psi}{dx} = -(2\pi y)^\epsilon \rho q \frac{A\sqrt{1+t^2}}{1+A\uparrow} \equiv p_D \quad \text{VII-(15)}$$

(c) Boundary Point Construction

This procedure is employed when the boundary contour is prescribed, as in the performance deck or in the initial part of the design deck. In the latter case, the boundary is the circular arc initiated at the throat. Here

$$y = y_0(1+\mu) - \sqrt{\mu^2 y_0^2 - x^2}, \quad t = - \frac{x}{y - y_0(1+\mu)} \quad \text{VII-(16)}$$

μ is the radius ratio (see schematic of Basic Nozzle Configuration). In the case of the performance deck, the boundary is taken to consist of the initial circular arc and a spline-fitted curve adjoined to this. The latter curve is determined by prescribing a table of points through which the contour is to pass. The spline fit is made with the fitted curve tangent to the circular arc at the junction. The cubic segment involved is given generally by (cf Ref. 67)

$$y = M_{c-1} \frac{(x_i - x)^3}{6l_i} + \frac{M_i(x - x_{i-1})^3}{6l_i} + \left(\frac{y_{c-1}}{l_c} - \frac{M_{c-1}l_i}{6} \right) (x_c - x) + \left(\frac{y_c}{l_c} - \frac{M_{c-1}l_i}{6} \right) (x - x_{c-1}) \quad \text{VII-(17)}$$

$$t = \frac{y_c - y_{c-1}}{l_i} + \frac{l_i}{6} (M_{c-1} + M_i) + \frac{M_i}{2l_i} (x - x_{c-1})^2 - \frac{M_{c-1}}{2l_i} (x_c - x)^2 \quad \text{VII-(18)}$$

for $x_{c-1} \leq x \leq x_i$; here $l_i = x_i - x_{i-1}$ and the M_i are the corresponding "moments".

The boundary point iteration now proceeds as follows: Equations VII-(5) and VII-(16) yield $x_c^{(K)}, y_c^{(K)}$ explicitly if the circular arc is involved. For the spline curve, VII-(5) and the appropriate representation VII-(18) are solved by a second-order False Position procedure to yield this intersection point. The quantity $t_c^{(K)}$ comes from VII-(18), $p_c^{(K)}$ from VII-(5), f and q from VII-(8) and VII-(9) with $e^{(K)} \equiv e$.

(d) Axis-Point Construction

Here $y_c^{(K)} = .001 y_0$ and $t_c^{(K)} = 0$. Thus VII-(6) gives $x_c^{(K)}$ and VII-(7) gives $p_c^{(K)}$. Again VII-(8) and VII-(9) give $\rho_c^{(K)}$ and $q_c^{(K)}$ with $e^{(K)}$ fixed at e .

In the first construction of the new Mach line B'F', the quantity X is taken to be zero, a frozen composition construction results. In subsequent iterations, X is determined from the results of the reaction kinetics integrations, and $c^2 = \frac{\gamma g p}{\rho}$ is obtained from γ fitted against ψ/ψ_B .

Integration of the Stream Function

Following the construction of the mesh points on a particular iteration to B'F', the stream function ψ is integrated as follows: the derivative $d\psi/dx = p_0$ is spline fitted against x and integrated. The quantity $(\psi_B' - \psi_{B_0})/\psi_{B_0}$ is used as a measure of accumulated error in the characteristics construction.

The quantity ψ is evaluated at each mesh point and the variables x, y, p, t , then fitted against ψ/ψ_B' . The quantities x, y, p, t are determined at the principal streamline positions.

Integration Along Principal Streamlines

It is now necessary to integrate the reaction kinetics relations along the principal streamlines. The characteristics equations along a streamline are

$$\frac{\rho'}{\rho} = \frac{1}{\gamma} \frac{p'}{p} + \sum_{j=1}^n \left[\frac{h_j g^j (\gamma-1)}{c^2} - \frac{1}{\sum_i \sigma_i} \right] \sigma_i' \quad \text{VII-(19)}$$

$$q q' = \frac{g}{\rho} p' \quad \text{VII-(20)}$$

$$\sigma_j' = \frac{\xi_j}{\rho q} \sqrt{1 + t^2} \quad \text{VII-(21)}$$

where primes indicate differentiation with respect to x .

From the previous determination of B'F', the quantities p , t , x , are available for the principal streamline points. Take p , t , x at the corresponding points on BF and on the Mach line preceding BF. Fit p and t against x quadratically: $p = p(x)$, $t = t(x)$. Equations VII-(19), (20), and (21) are integrated by the Runge-Kutta method from BF to B'F' along each of these streamline segments to obtain at the terminal points $\rho, q, \sigma_1, \dots, \sigma_n$ and hence $T = p/\rho R \sum \sigma_i$. The quantities c_{p_i} are introduced at the outset in tabular form and spline-fitted as functions of T . Here then

$$\gamma = \frac{\sum_{i=1}^n c_{p_i} \sigma_i}{\sum_{i=1}^n c_{p_i} \sigma_i - \frac{R}{J} \sum_{i=1}^n \sigma_i} \quad \text{VII-(22)}$$

is determined at each of the principal streamline positions on B'F' and spline-fitted against ψ/ψ_{TOT} . The values of γ thus lag by one iteration but this effect is negligible.

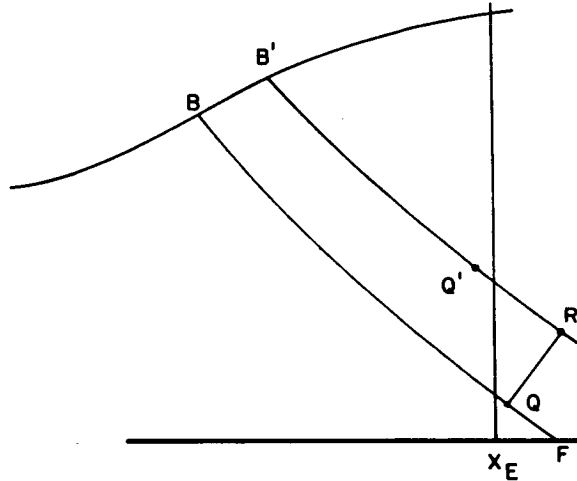
The quantity \bar{X} is next fitted against ψ/ψ_{TOT} to be used in the subsequent iterations for B'F'.

Terminal Procedure - Performance Deck

The construction of successive down Mach lines in the performance deck is carried on until BF is obtained for which x_F exceeds a prescribed cut off x_E .

Counting from the top, let Q be the first principal streamline terminus on BF which lies to the right of $x = x_E$ (Q may be F). All mesh points on BF below Q are deleted and Q is entered as the last mesh point on BF .

The frozen composition calculation of $B'R'$ (QR' is the up Mach line from Q) is carried out in the usual way. By integration ψ is obtained along $B'R'$ with $\psi_R' = 0$.



3.) TERMINAL PROCEDURE

When the integration is complete the quantity, $\psi_B - \psi_B'$, is added to each of the ψ entries (ψ_B' now equals ψ_B). The quantities p and t are fitted against ψ/ψ_B' and the principal streamline points on $B'R'$ are obtained. Counting from the top, the point Q' is the last streamline termination point above R' or the first beyond x_E , whichever is first. (Note that Q' may be to the left of x_E .)

The reaction kinetics equations are integrated along the principal streamlines, the last terminating at Q' , and X and γ are fitted against ψ/ψ_B' .

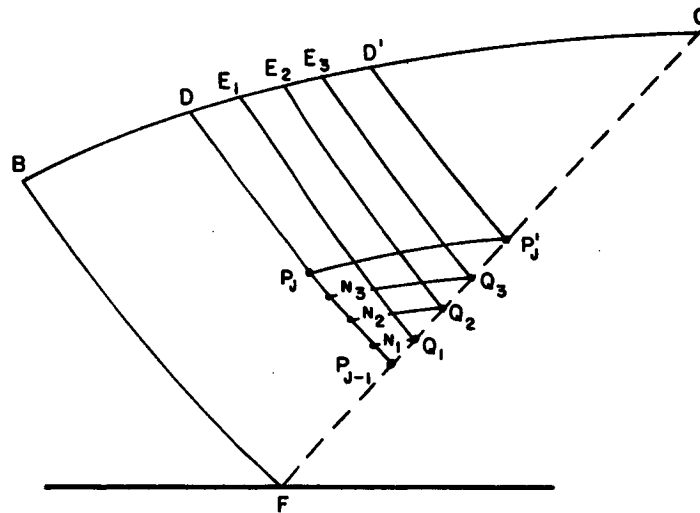
The mesh points on $B'R'$ are now recalculated using the results of the principal streamline integrations. For beyond-the-end-of-table properties on $B'R'$ (R' will be below Q') the spline fits on BQ are used. (Note: this device is merely a convenient termination device. If the flow is frozen, there will be an error here. If not, the error is actually inconsequential.)

This problem is now iterated to the necessary extent. A flow chart for the axisymmetric/two-dimensional machine program is outlined on the following page.

Modified Perfect Nozzle Construction

The modified perfect nozzle is one for which the exhaust flow is axial in direction. The exit Mach line for such a nozzle will, however, not be straight inasmuch as the histories of the gas along different streamlines are different. This section presents the termination procedure for the calculation of these nozzles.

In the Figure (Modified Perfect Nozzles) below, BF is a down Mach line determined by the methods described in detail above. It remains to calculate the flow field in region BFC and so to determine the contour BC. The construction consists of constructing the exit Mach line FC simultaneously with the down Mach lines backward from FC to the contour.



4.) MODIFIED PERFECT NOZZLES

These Mach lines are constructed in groups. Initiating a group is a Mach line DP_{j-1} , where P_{j-1} is a principal streamline point. The number of Mach lines in the group, following DP_{j-1} and preceding $D'P'_j$, is equal to the number of mesh points between P_{j-1} and P_j on DP_{j-1} . The construction of this group is typical and is presented in detail.

(a) Construction of Point P'_j

From $\psi_{P'_j} / \psi_B = \psi_{P_j} / \psi_D$, and ψ_D determine $\gamma_{P'_j(i)}$ from

$$\frac{\psi_{P'_j}}{\psi_D} = \frac{1}{2} \left[(\rho q)_{P_{j-1}} + (\rho q)_{P_{j(i-1)}} \right] \pi \left(\gamma_{P_{j(i)}}^{\epsilon+1} - \gamma_{P_{j-1}}^{\epsilon+1} \right) + \psi_{P_{j-1}} \quad \text{VII-(23)}$$

$P'_{j(0)} = P_{j-1}$

From VII-(4) get $x_{P'_j(i)}$ Set $t_{P_j} = 0$. From VII-(5) get $P_{P'_j(i)}$, from VII-(8) and VII-(9) get $\rho_{P'_j(i)}$ and $q_{P'_j(i)}$.

Integrate reaction equations along $P_j P'_j$ after making quadratic fit of p and t vs x . These yield \bar{X} , at $P'_j(i)$ as well as $\sigma_1, \sigma_2, \dots, \sigma_n$.

Note that this iteration begins with a frozen composition determination of $P'_j(X=0)$. Thereafter, two or three iterations are usually sufficient.

(b) Interpolation for conditions on $P_{j-1} P'_j$

The quantities $x, y, p, \rho, q, \bar{X}, \gamma$ are fitted quadratically against ψ on the exit streamline, using P_j, P_{j-1} , and the streamline point next below P_{j-1} on FC. Values at Q_1, Q_2, Q_3 are computed based upon the stream function values at N_1, N_2, N_3 .

In order to improve the first such interval (immediately following F on FC) over which the interpolation is necessarily linear, a special additional principal streamline close to the axis cylinder is incorporated into the design deck.

(c) Backward construction of the Mach line $E_1 Q_1$ up from Q_1 .

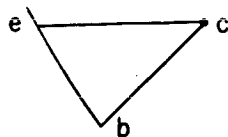
First construct $E_1 Q_1$ using frozen composition ($X=0$). The equation $d\psi/dx = P_D$ is integrated to determine the stream function. Segments of streamlines are chosen by fitting p and t vs x . The reaction kinetic equations are integrated along the principal streamlines from $P_{j-1} D$ to $Q_1 E_1$, giving a fit of \bar{X} and γ against ψ/ψ_B . In this fit are employed the values of \bar{X} and γ established previously at Q_1 by interpolation. The iteration is now repeated using \bar{X} and γ as determined on $Q_1 E_1$.

The point constructions are modifications of those previously employed. Q_1 is constructed such as was P'_j , except that the values \bar{X} and γ at Q_1 are already available.

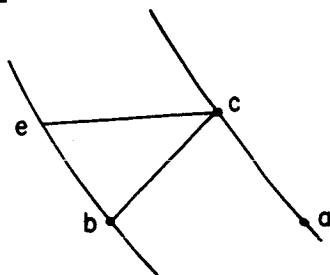
For the interior point (see schematic of Termination Procedure), the identical procedure used previously is applicable of $\psi_C/\psi_B \leq 1$. When ψ_C exceeds ψ_B , the

boundary point (see schematic of Termination Procedure) must be calculated.

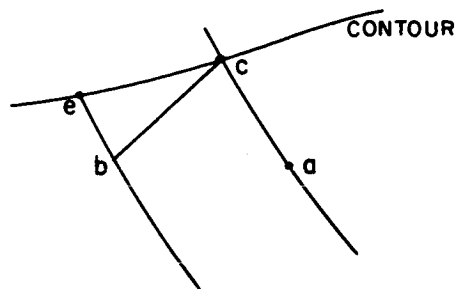
5.) TERMINATION PROCEDURE



A.) EXIT POINT



B.) INTERIOR POINT



C.) BOUNDARY POINT

For the determination of the boundary point (see schematic of Termination Procedure) the point $x_c(K)$, $y_c(K)$ is determined from (6) and

$$y_{c(K)} - y_e = \frac{1}{2} [t_e + t_{c(K-1)}] (x_{c(K)} - x_e) \quad \text{VII- (24)}$$

$$c^{(0)} = e$$

From VII-(4) modified,

$$y_{b(K)} - y_{c(K)} = \frac{1}{2} [(M_u)_{c(K-1)} + (M_u)_{b(K-1)}] (x_{b(K)} - x_{c(K)}) \quad \text{VII- (25)}$$

and VII-(6) from e

$$y_{b(K)} - y_e = \frac{1}{2} [(M_D)_e + (M_D)_{b(K-1)}] (x_{b(K)} - x_e) \quad \text{VII- (26)}$$

$$c^{(0)} = b^{(0)} = e$$

are obtained $x_b(k)$ and $y_b(k)$.

$$\text{Set } \psi_{c(K)} = \psi_e$$

$$\frac{\psi_{b(K)}}{\psi_e} = 1 - \frac{1}{2} [(P_u)_{c(K-1)} + (P_u)_{b(K-1)}] (x_{c(K)} - x_{b(K)}) \quad \text{VII- (27)}$$

$$b^0 = e, \quad c^0 = a$$

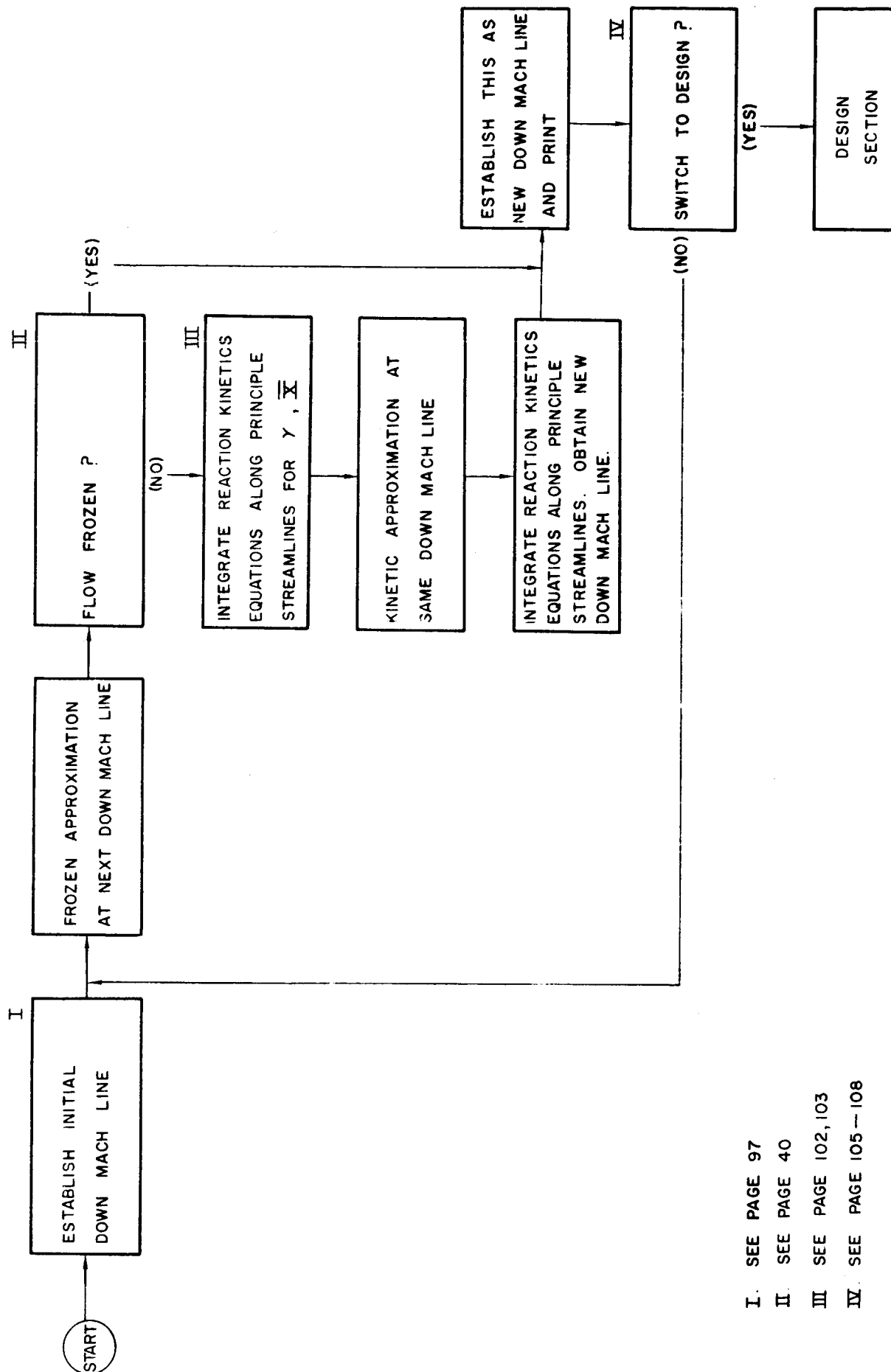
The quantities ρ, q, P, t, X, c are known from spline fits on the down Mach line containing b and e .

With VII-(5) from $b^{(K)}$ and VII-(7) from a obtain $P_c^{(K)}$ and $t_c^{(K)}$. Obtain $q_c^{(K)}$ and $\rho_c^{(K)}$ from VII-(8) and VII-(9) with e fixed.

Frozen Composition Construction

The normal iteration process for the construction of successive down Mach lines continues until the flow is essentially frozen. This is said to occur when γ_p/γ is sufficiently close to unity. Thereafter only the frozen composition calculation is effected.

TWO - DIMENSIONAL / AXISYMMETRIC PROGRAM



- I. SEE PAGE 97
- II. SEE PAGE 40
- III. SEE PAGE 102, 103
- IV. SEE PAGE 105 - 108

APPENDIX VIII

DETAILED DESCRIPTION OF TEST APPARATUS

The test apparatus employed during this investigation may be divided into the following subsystems: (1) carrier gas supply; (2) reactant supply; (3) heat exchanger; (4) transition and test nozzle; (5) diffuser and exhaust; and (6) instrumentation. The components of these systems are shown schematically in Fig. 27, and are described in detail below. With the exception of the exhaust system ejector and stack, all system components which were subject to exposure to the reactant chemical in either concentrated or dilute form were fabricated of stainless steel and all control components had metal to metal or fluorocarbon seats and seals.

Carrier Gas Supply System

The carrier gas, dry nitrogen, was stored at a pressure of approximately 2000-psi in a manifold consisting of 124 K-type cylinders. The first stage of gas pressure regulation was accomplished by a Grove dome controller (model GBX-306-N4) located between the supply manifold and the test cell. The delivery pressure of this regulator was controlled by adjusting the nitrogen pressure in the control dome through manipulation of small load and vent valves. A Republic relief valve set to limit the downstream pressure to a maximum of 250 psig was installed in the supply line immediately after the Grove regulator. The nitrogen flow metering device was a standard ASME long radius nozzle which was designed according to the applicable specifications presented in Ref. 69. Second and final stage pressure regulation was provided by a Spence regulator (model E-4-D). The balancing pressure signal for the pilot valve of this regulator was taken from the test nozzle entrance via a 1/4 in. tubing and the test nozzle entrance pressure was controlled through manual adjustment of the spring force against the balancing diaphragm of the pilot valve.

Reactant Supply System

The chemical reactant, N_2O_4 , was stored in the liquid phase in its shipping container (ICC-3D480). The liquid was expelled from this container with dry nitrogen maintained at a constant head by a small-volume pressure regulator. The chemical flowed to the reaction tunnel through 1/4 in. stainless steel tubing. The flow rate was controlled by a Hoke micrometer throttling valve and measured with a Fisher and Porter variable area flowmeter (10A1735A) having an accuracy of $\pm 1\%$ of full scale (i.e., ± 0.0005 lb/sec). Prior to entering the flowmeter, the reactant

passed through a coil of 25 ft of stainless steel tubing which was immersed in a water-ice bath. The purpose of this assembly was to maintain the reactant temperature at a value for which the liquid density is well known and to minimize the magnitude of flow-rate corrections for the flowmeter which was calibrated for liquid nitrogen tetroxide at 0 C.

Provision was made for purging the entire system with dry nitrogen and all venting was accomplished through the exhaust system of the flow reactor. Also, a gaseous oxygen source was provided. Before each series of tests, oxygen was bubbled through the reactant in the storage container by means of the container dip leg to oxidize any lower nitrogen oxide compounds that might have been present.

Heater System

The heater system was composed of a steam preheater and a eutectic-alloy-bath heat exchanger. A Kiwannee-Ross steam heat exchanger operating on 100 psig steam was used to preheat the metered nitrogen to a controlled temperature of approximately 760 R. The maximum temperature obtainable as preheat was a function of the flow rate of nitrogen, but could never exceed the steam saturation temperature of about 798 R. In practice, the temperature control (Mason-Neilan proportional controller actuating a pneumatically positioned Taylor valve) was set at less than the maximum so that operation was in the proportional region. Under steady state conditions the preheat temperature could be held constant within about ± 5 R^o, from about 560 to 760 R. The liquid N₂O₄ was injected into the preheated carrier gas (nitrogen) stream at the exit of the preheater.

The mixture of reactant (N₂O₄ or NO₂) and preheated carrier gas (N₂) was raised to the final operating temperature in a specially designed heat exchanger. This heat exchanger consisted of 34 ft of 2 in. ID type 304 stainless steel pipe submerged in a eutectic alloy of 71% tin, 24% lead, and 5% zinc. The quoted pipe length is more than sufficient to provide complete turbulent mixing of the reactants. This alloy, with a density of 494.4 lbs/ft³ and a melting point of 810 R, was contained in a four-compartment carbon-steel box. Twenty-two Watlow strip heaters (total rating 26.47 Kw) were bonded to the box with Trans-A-Therm heat conductive putty, and fixed in place with straps and bolts. The entire assembly was placed in an insulating box with 1 in. thick Marinite walls and an air gap of 1 1/2 in. between inner and outer boxes. The electric heaters were automatically controlled in three independent groupings to hold the temperature of the eutectic alloy just above the melting point. In operation, the first flow of gases through the heat exchanger dropped the temperature of the alloy to the melting point, and the temperature then stabilized at this level for essentially all of an experimental run. The latent heat of fusion of the alloy (approximately 1000 lbs) was slightly

more than 22000 Btu, enough to heat the gases from the preheat to final temperature for over 10 minutes at normal flow rates. With a constant inlet temperature (preheat or interstage temperature), the outlet temperature from the eutectic heat exchanger did not drop significantly during a test because there was no progressive cooling of the eutectic as heat was extracted by the gases. A vernier effect was obtained whereby a change of 4.25 R° in the interstage temperature was required (by design) to give a change of 1 R in the final heater outlet temperature. In practice, the temperature fluctuation of $\pm 5\text{ R}^\circ$ from the preheater resulted in about a $\pm 1\text{ R}^\circ$ variation in final temperature.

Transition and Test Nozzle System

Upon leaving the heaters, the reactant mixture passed through a 3-in. Worcester ball valve which was used to isolate the test section from the reactant supply during measurements of the reference or zero transmitted light intensity, I_i , with the photometer system. A calming section which consisted of a length of 8-in. dia pipe containing a series of four 200-mesh screens was provided downstream of the ball valve to reduce the gas stream turbulence level and remove any particulate foreign matter which might have been carried from the carrier gas supply system. The round calming section was connected to the rectangular test nozzle entrance by a transition section.

The two-dimensional test nozzle is shown schematically in Fig. 28 and a photograph of the completed nozzle assembly is presented in Fig. 29. The test section was originally conceived as a bilaterally symmetrical, two-dimensional nozzle with a throat height of 1.25 in. and a throat aspect ratio of 2 but, because of the high carrier gas flow rate required for such a nozzle and the hazards associated with the liberation of large quantities of nitrogen tetroxide to the atmosphere, the final design was that of a half-nozzle. The top block of this nozzle had a convergence of 30 deg. , a blended throat radius of 2.5 in., and a divergence angle of 14 deg. The bottom block was displaced 0.004 in. from the pseudocenterline at the nozzle throat and diverged at an angle of $0\text{ deg.}, 15\text{ min.}$ to account for the calculated boundary layer displacement thickness on this wall. No contribution to the convergence of the subsonic portion of the nozzle was provided by this block. The internal configuration of the nozzle assembly was such that the geometric contraction ratio was 6.385 and the expansion ratio was 2.013. The nozzle had a constant width of 2.5 in., an entrance height of 4.016 in., a throat height of 0.629 in., and an exit height of 1.266 in. The blocks were so machined as to provide a thickness of 0.250 in. for the top and bottom walls of the nozzle. The nozzle side walls were fabricated of 0.025 in. thick plate, and they included provisions for the insertion of 0.375 in. thick optically flat pyrex windows. The windows were held in place on the side plates by stainless steel retaining frames. The windows were

sealed to the side plates and the side plates to the nozzle blocks with 3M EC 801 sealer. At assembly, four 0.032 in. holes were drilled in the lower corners of the window frames. The holes were at the four corners of a rectangular plane which was parallel to and 0.057 in. above the flat, horizontal portion of the bottom nozzle block. The axial distance between holes was 10.875 in. During testing, the photometer system was aligned so the lowest of the five light beams passed through each set of opposing holes as it was traversed from one end of the nozzle to the other. These holes also provided axial displacement reference points during testing by causing alternate blanking and unblanking of the bottom light beam of the photometer as it moved past them in its traverse.

A 0.125 in. stainless steel sheathed thermocouple (chromel-alumel) and a static pressure tap were located at the test nozzle entrance. Also, four static pressure taps were located on the centerline in the supersonic portion of the top nozzle block for purposes of comparison of the pressure distribution in the test nozzle with that measured in the calibration nozzle. The calibration nozzle had identical internal scale and geometry to that of the test nozzle but was more completely instrumented with pressure taps for the determination of boundary layer characteristics through tests in a separate wind tunnel.

Diffuser and Exhaust Section

The flow reactor included a two-dimensional, fixed-geometry diffuser at the nozzle exit to ensure shock-free flow in the test section. The nitrogen tetroxide-nitrogen mixture leaving the diffuser was ducted to the suction side of an Ingersoll-Rand air ejector C4-10x10-504x8. The motive air for this ejector was a portion of the output of one, two, or three Spencer thirteen stage centrifugal compressors operated in parallel. Four pounds per second of primary air at 50.4 in. Hg absolute were required for design operation of the ejector. Using two compressors (normal operation), a flow of 29.6 lbs/sec was available, at 50.4 in. Hg absolute. The air not required for operation of the ejector was diverted up a 2 ft diameter, 20 ft tall exhaust stack. The effluent from the ejector, containing approximately 4 lbs/sec of air, 0.9 lbs/sec of nitrogen from the test section, and a maximum of 0.05 lbs/sec of N_2O_4 was discharged into the stack and mixed with the diverted air from the compressors. Considering the total stack flow of 30.55 lbs/sec (25.6 lbs/sec diverted air, 4 lbs/sec motive air, 0.9 lbs/sec nitrogen carrier gas, and 0.05 lbs/sec N_2O_4), the effluent contained about 1640 ppm N_2O_4 . At wind velocities of 10 mph or less the effective stack height was at least 100 ft, resulting in (calculated) maximum concentrations of N_2O_4 on the ground of less than 1.5 ppm at distances of a half mile or more. The design dead-end operation of the ejector with design motive air flow was less than 17.3 in. Hg absolute. In operation, suction port pressures less than this were obtained at full flow.

Instrumentation System

Pressure and Temperature Transducers

All pressure transducers used for recorded data during the test program were strain gauge-type units selected to have pressure ranges which were consistent with the pressure levels measured. The quoted accuracy of these units is $\pm 0.5\%$ of full scale. A pressure transducer was provided for each of the following measurements:

1. Carrier gas flow nozzle upstream pressure
2. Carrier gas flow nozzle differential pressure
3. Test nozzle entrance pressure
4. Test nozzle exit pressure

Prior to each test run, the first two transducers were calibrated against a Heise Laboratory Test Gauge which has a range of 300 psig and an accuracy of 0.25% of full scale. The second two transducers were calibrated with mercury-filled U-tube manometers having a reading accuracy of 0.05 in. Hg.

The thermocouples used and parameters recorded were:

1. Preheater exit temperature (copper-constantan)
2. Test section entrance temperature (chromel-alumel)
3. Carrier gas temperature at flow nozzle (copper-constantan)
4. Reactant (N_2O_4) temperature at flowmeter entrance (copper-constantan)

All thermocouples were calibrated before each test run with a Technique Associates, Inc. Pyrotest (Model 9B) which has an accuracy of ± 0.02 MV.

Absorption Photometer

A schematic diagram of the photometer is shown in Fig. 30. The light source was a six-volt ribbon-filament incandescent lamp (18A/T-10/2P-6) operated from a 60-cycle AC transformer. A Sola voltage regulating transformer was placed between the line and the six-volt transformer to eliminate the effect of line voltage variation. An image of the lamp filament was formed by a pair of condensing lenses (1.75 in. F. L., 1.25 in. dia.) at the focus of the collimating lens (3 in. F. L.). The

resulting collimated beam passed through an aperture plate which contained five 0.014 in. dia. holes vertically spaced 0.250 in. on centers. The five resulting light beams traveled across a five-in. work space where the test nozzle was placed. The collimation was such that the 0.014 in. dia. beams spread to a maximum dia. of 0.052 in. at the far side of the work space. The light beams then entered a ten-in. long light baffle which was mounted on the front of the photomultiplier housing to preclude the admission of room illumination. The beams next passed through a Baird Atomic, Inc. filter (4358B5) having a half peak band pass between 3943 Å and 4773 Å, and were directed by first surface aluminized mirrors to the cathodes of five 1P21 photomultiplier tubes placed in a semicircular array. The instrument components were placed in two light-tight boxes which were rigidly mounted to a single aluminum channel base. A number of baffles were positioned in the system as shown in Figs. 30 and 31 and all surfaces normal to the optical axis were painted dull black.

Prior to the test program, a calibration of the photometer system was made with a series of filters of known absorption to check the operation of the system. The results of these tests indicate that the instrument operation was well within the linear range of the photomultipliers.

Power for the five photomultipliers was provided by an NJE Corp. Model S-326 regulated power supply having a rated stability of $\pm 0.005\%$ for line voltage variations of $\pm 10\%$. The circuitry of the photomultiplier system is shown in Fig. 40.

The instrument base channel was fastened to a manually driven traversing carriage which ran on rails held in fixed parallel relationship to the test nozzle axis. An antibacklash gear train between the traverse drive screw and a 1000 ohm, ten-turn potentiometer provided a means of obtaining photometer position data. The potentiometer was rated as having a maximum deviation from linearity of 0.1%.

Data Recording System

The outputs of all data transducers were transmitted over approximately 300 ft of shielded cables to an Epsco high-speed data recording system where they were passed through a DC amplifier, attenuators in some cases, 10 cps low-pass filters and a Datrac digital converter in that order. The data was read from the Datrac unit every tenth of a second during a test run and recorded on magnetic tape. The data recording accuracy of the Epsco system is $\pm 0.33\%$. The tape was subsequently played into an IBM 7090 computer which reduced, sorted and tabulated the data. An additional function of the computer was to write an input tape for a Cal Comp plotter which provided curves of the five photomultiplier outputs versus the position indicating potentiometer output.

The excitation voltage (6 volts DC) for the strain gauge transducers and the potentiometer bridge circuit was supplied by the regulated power supply of the Epsco data system.

APPENDIX IX
DISTRIBUTION LIST

<u>COPIES</u>	<u>RECIPIENT</u>
	NASA Headquarters Washington 25, D. C.
1	Contracting Officer, BC
1	Patent Office, AGP
	NASA Lewis Research Center, Mail Stop 0-7 Chemical Rocket Systems Procurement Section 21000 Brookpark Road Cleveland 35, Ohio
10	Contracting Officer
	<u>NASA HEADQUARTERS</u> Washington 25, D. C.
3	Mr. Henry Burlage, Jr. Chief, Liquid Propulsion Systems, RPL
1	Mr. A. O. Tischler Assistant Director for Propulsion, MLP
25	Scientific and Technical Information Facility NASA Representative (CRT) P. O. Box 5700 Bethesda, Maryland
	<u>TECHNICAL MANAGER</u>
1	Mr. Thomas Mariani NASA Lewis Research Center 21000 Brookpark Road Cleveland 35, Ohio
	<u>NASA FIELD CENTERS</u>
2	Ames Research Center Moffett Field, California
2	Goddard Space Flight Center Greenbelt, Maryland

COPIES

RECIPIENT

2	Jet Propulsion Laboratory California Institute of Technology 4800 Oak Grove Drive Pasadena, California
2	Langley Research Center Langley Field, Virginia
2	Lewis Research Center 21000 Brookpark Road Cleveland 35, Ohio
2	Marshall Space Flight Center Huntsville, Alabama
2	Manned Spacecraft Center Houston, Texas

GOVERNMENT INSTALLATIONS

1	Advanced Research Projects Agency Pentagon, Room 3D154 Washington 25, D. C.
1	Aeronautical Systems Division Air Force Systems Command Wright-Patterson Air Force Base, Ohio
1	Air Force Missile Development Center Holloman Air Force Base, New Mexico
1	Air Force Missile Test Center Patrick Air Force Base, Florida
1	Army Ordnance Missile Command Redstone Arsenal, Alabama
1	Armed Services Technical Information Agency Arlington Hall Station Arlington 12, Virginia
1	Arnold Engineering Development Center A. E. O. R. Tullahoma, Tennessee

COPIES

RECIPIENT

1	Bureau of Naval Weapons Department of the Navy Washington 25, D. C.
1	Central Intelligence Agency 2430 E Street, N. W. Washington 25, D. C. Attn: Miss Elizabeth F. Kerman
1	Headquarters, United States Air Force Washington 25, D. C.
1	Picatinny Arsenal Dover, New Jersey
1	Rocket Research Laboratories Edwards Air Force Base, California
1	U. S. Naval Ordnance Test Station China Lake, California
1	U. S. Atomic Energy Commission Technical Information Services Box 62 Oak Ridge, Tennessee

LPFA

Chemical Propellant Information Agency
Johns Hopkins University
Applied Physics Laboratory
8621 Georgia Avenue
Silver Spring, Maryland

COMMERCIAL CONTRACTORS

1	Aerojet-General Corporation P. O. Box 296 Azusa, California
---	---

<u>COPIES</u>	<u>RECIPIENT</u>
1	Aerojet-General Corporation P. O. Box 1947 Sacramento 9, California
1	Aeronutronic A Division of Ford Motor Company Ford Road Newport Beach, California
1	Aerospace Corporation 2400 East El Segundo Boulevard El Segundo, California
1	Arthur D. Little, Inc. Acorn Park Cambridge 40, Massachusetts
1	Astropower, Inc., Subsidiary of Douglas Aircraft Company, Inc. 2968 Randolph Avenue Costa Mesa, California
1	Astrosystems, Inc. 82 Naylon Avenue Livingston, New Jersey
1	Atlantic Research Corporation Edsall Road and Shirley Highway Alexandria, Virginia
1	Beech Aircraft Corporation Boulder Facility Box 631 Boulder, Colorado
1	Bell Aerosystems Company P. O. Box 1 Buffalo 5, New York
1	Bendix Systems Division Bendix Corporation Ann Arbor, Michigan

<u>COPIES</u>	<u>RECIPIENT</u>
1	Boeing Company P. O. Box 3707 Seattle 24, Washington
1	Convair (Astronautics) Division of General Dynamics Corporation P. O. Box 2672 San Diego 12, California
1	Curtiss-Wright Corporation Wright Aeronautical Division Wood-ridge, New Jersey
1	Douglas Aircraft Company, Inc. Missile and Space Systems Division 3000 Ocean Park Boulevard Santa Monica, California
1	Fairchild Stratots Corporation Aircraft Missiles Division Hagerstown, Maryland
1	General Electric Company Missile and Space Vehicle Department Box 8555 Philadelphia, Pennsylvania
1	General Electric Company Rocket Propulsion Units Building 300 Cincinnati 15, Ohio
1	Grumman Aircraft Engineering Corporation Bethpage, Long Island, New York
1	Itek Corporation Vidya Division 1450 Paze Mell Road Palo Alto, California
1	Kidde Aero-Space Division Walter Kidde and Company, Inc. 675 Main Street Belleville 9, New Jersey
1	Lockheed Aircraft Corporation Missile and Space Division Sunnyvale, California

<u>COPIES</u>	<u>RECIPIENT</u>
1	Lockheed Propulsion Company P. O. Box 111 Redlands, California
1	Marquardt Corporation 16555 Saticoy Street Box 2013 - South Annex Van Nuys, California
1	Martin Division Martin Marietta Corporation Baltimore 3, Maryland
1	Martin Denver Division Martin Marietta Corporation Denver, Colorado
1	McDonnell Aircraft Corporation P. O. Box 6101 Lambert Field, Missouri
1	North American Aviation, Inc. Space & Information Systems Division Downey, California
1	Northrop Corporation 1001 East Broadway Hawthorne, California
1	Pratt & Whitney Aircraft Corporation Florida Research & Development Center West Palm Beach, Florida
1	Radio Corporation of America Astro-Electronics Division Defense Electronic Products Princeton, New Jersey
1	Reaction Motors Division Thiokol Chemical Corporation Denville, New Jersey

COPIES

RECIPIENT

1	Republic Aviation Corporation Farmingdale Long Island, New York
1	Rocketdyne (Library Dept. 586-306) Division of North American Aviation, Inc. 6633 Canoga Avenue Canoga Park, California
1	Space General Corporation 9200 Flair Avenue El Monte, California
1	Space Technology Laboratories P. O. Box 95001 Airport Station Los Angeles 45, California
1	Stanford Research Institute 333 Ravenswood Avenue Menlo Park, California
1	TAPCO Division Thompson-Ramo-Wooldridge, Inc. 23555 Euclid Avenue Cleveland 17, Ohio
1	Thiokol Chemical Corporation Redstone Divison Huntsville, Alabama
1	United Aircraft Corporation East Hartford Plant 400 Main Street East Hartford, Connecticut
1	United Technology Corporation 587 Methilda Avenue Sunnyvale, California
1	Vought Astronautics Box 5907 Dallas 22, Texas

COPIES

RECIPIENT

EDUCATIONAL INSTITUTIONS

1	Applied Physics Laboratory Johns Hopkins University 8621 Georgia Avenue Silver Spring, Maryland
1	California Institute of Technology 4800 Oak Grove Drive Pasadena, California
1	University of California Berkeley 4, California
1	Cornell Aeronautical Laboratory Buffalo, New York
1	Harvard University Cambridge, Massachusetts
1	Massachusetts Institute of Technology Cambridge, Massachusetts
1	New York University New York 53, New York
1	Princeton University Princeton, New Jersey
1	Purdue University West Lafayette, Indiana
1	Yale University New Haven, Connecticut

TABLE 1

KINETIC DATA FOR H₂-F₂ SYSTEM

<u>Reaction</u>	<u>Rate</u>
$\text{H} + \text{H} + \text{M} \rightleftharpoons \text{H}_2 + \text{M}$	$k_f = 2 \times 10^{18} \text{ T}^{-1} \text{ cm}^6 \text{ mol}^{-2} \text{ sec}^{-1*}$
$\text{H} + \text{F} + \text{M} \rightleftharpoons \text{HF} + \text{M}$	$k_f = 1.09 \times 10^{15} \text{ T}^{1/2} \text{ cm}^6 \text{ mol}^{-2} \text{ sec}^{-1**}$
$\text{F} + \text{F} + \text{M} \rightleftharpoons \text{F}_2 + \text{M}$	$k_f = 1.27 \times 10^{14} \text{ T}^{1/2} \text{ cm}^6 \text{ mol}^{-2} \text{ sec}^{-1**}$
$\text{H}_2 + \text{F} \rightleftharpoons \text{HF} + \text{H}$	$k_f = 2.45 \times 10^{10} \text{ T} \exp(-8.00/\mathcal{R} \text{ T}) \text{ cm}^3 \text{ mol}^{-1} \text{ sec}^{-1**}$
$\text{H} + \text{F}_2 \rightleftharpoons \text{HF} + \text{F}$	$k_f = 5.28 \times 10^{12} \text{ T}^{1/2} \exp(-4.00/\mathcal{R} \text{ T}) \text{ cm}^3 \text{ mol}^{-1} \text{ sec}^{-1**}$
$\text{H}_2 + \text{F}_2 \rightleftharpoons 2 \text{ HF}$	$k_f = 2.92 \times 10^{12} \text{ T}^{1/2} \exp(-39.5/\mathcal{R} \text{ T}) \text{ cm}^3 \text{ mol}^{-1} \text{ sec}^{-1**}$

NOTE: All activation energies in kcal/mol
Temperatures in °K

* See Reference 9

** Estimated

TABLE 2

SELECTED RATE DATA FOR THE $\text{N}_2\text{H}_4\text{-N}_2\text{O}_4$ SYSTEM

<u>Reaction</u>	<u>Rate</u>
$\text{H}_2 + \text{O}_2 \rightleftharpoons 2 \text{OH}$	$k_f = 1 \times 10^{14} \exp -70/\mathcal{R} T \text{ cm}^3 \text{ mol}^{-1} \text{ sec}^{-1*}$
$\text{OH} + \text{H}_2 \rightleftharpoons \text{H}_2\text{O} + \text{H}$	$k_f = 2.5 \times 10^{14} \exp -10/\mathcal{R} T \text{ cm}^3 \text{ mol}^{-1} \text{ sec}^{-1**}$
$\text{H} + \text{O}_2 \rightleftharpoons \text{OH} + \text{O}$	$k_f = 5 \times 10^{14} \exp -18/\mathcal{R} T \text{ cm}^3 \text{ mol}^{-1} \text{ sec}^{-1\dagger}$
$\text{O} + \text{H}_2 \rightleftharpoons \text{OH} + \text{H}$	$k_f = 2.5 \times 10^{12} \exp -7.7/\mathcal{R} T \text{ cm}^3 \text{ mol}^{-1} \text{ sec}^{-1**}$
$\text{H} + \text{H} + \text{M} \rightleftharpoons \text{H}_2 + \text{M}$	$k_f = 2 \times 10^{18} T^{-1} \text{ cm}^6 \text{ mol}^{-1} \text{ sec}^{-1\dagger\dagger}$
$\text{O} + \text{O} + \text{M} \rightleftharpoons \text{O}_2 + \text{M}$	$k_f = 2 \times 10^{19} T^{-3/2} \text{ cm}^6 \text{ mol}^{-1} \text{ sec}^{-1* \dagger}$
$\text{OH} + \text{M} \rightleftharpoons \text{O} + \text{H} + \text{M}$	$k_f = 1 \times 10^{21} T^{-3/2} \exp -101/\mathcal{R} T \text{ cm}^3 \text{ mol}^{-1} \text{ sec}^{-1*}$
$\text{H}_2\text{O} + \text{M} \rightleftharpoons \text{H} + \text{OH} + \text{M}$	$k_f = 2 \times 10^{22} T^{-3/2} \exp -114.7/\mathcal{R} T \text{ cm}^3 \text{ mol}^{-1} \text{ sec}^{-1*}$
$\text{OH} + \text{OH} \rightleftharpoons \text{H}_2\text{O} + \text{O}$	$k_f = 2.5 \times 10^{14} \exp -10/\mathcal{R} T \text{ cm}^3 \text{ mol}^{-1} \text{ sec}^{-1*} \text{ and } **$

NOTE: All activation energies in kcal/mol
Temperature in $^{\circ}\text{K}$

* Reference 14

** Reference 15

\dagger Reference 16

$\dagger\dagger$ Reference 9

* \dagger Reference 17

TABLE 3

SIGNIFICANT RECOMBINATION REACTIONS

 B_2H_6 - OF_2 SYSTEM

<u>Over-All Reaction</u>	<u>ΔN_i, mols/100g</u>	<u>ΔH_{ri}, kcal/mol</u>	<u>Δh_i, kcal/100g</u>	<u>Percent of Δh_{total}</u>
$BF + 2F \rightarrow BF_3$	0.05	-259.8	13.0	12.4
$BF + 2HF \rightarrow BF_3 + H_2$	0.03	-158.6	4.8	
$BF + HF \rightarrow BOF + \frac{1}{2} H_2$	0.17	- 83.5	14.2	
$BF + OH \rightarrow BOF + \frac{1}{2} H_2$	0.10	-107	10.7	33.7
$BF + O \rightarrow BOF$	0.15	-156	23.4	
$H \rightarrow \frac{1}{2} H_2$	1.50	- 51.6	77.4	53.9
			<u><u> </u></u>	<u><u> </u></u>
		$h_{total} =$	143.5	100.0

TABLE 4
REACTION MECHNAISM AND RATE DATA FOR
HYDROGEN-OXYGEN SYSTEM

<u>Reaction Mechanism</u>	<u>Reaction Rate</u>	<u>Reference</u>
1. $\text{H}_2 + \text{OH} \xrightleftharpoons[k_b^1]{k_f^1} \text{H}_2\text{O} + \text{H}$	$k_f^1 = 4.2 \times 10^9 \times T^{0.5} \exp(-10/RT)$	53,54
2. $\text{H} + \text{O}_2 \xrightleftharpoons[k_b^2]{k_f^2} \text{OH} + \text{O}$	$k_f^2 = 5.64 \times 10^{10} \exp(-15.1/RT)$	55
3. $\text{H}_2 + \text{O} \xrightleftharpoons[k_b^3]{k_f^3} \text{OH} + \text{H}$	$k_f^3 = 1.2 \times 10^{10} \exp(-9.2/RT)$	56
4. $\text{H} + \text{H} + \text{M} \xrightleftharpoons[k_b^4]{k_f^4} \text{H}_2 + \text{M}$	$k_b^4 = 10^{18} \times T^{-1.5} \exp(4103.2/RT)$	14 adjusted to agree with 52
5. $\text{H} + \text{OH} + \text{M} \xrightleftharpoons[k_b^5]{k_f^5} \text{H}_2\text{O} + \text{M}$	$k_b^5 = 2 \times 10^{19} \times T^{-1.5} \exp(-114.7/RT)$	14 adjusted to agree with 52
6. $\text{O} + \text{O} + \text{M} \xrightleftharpoons[k_b^6]{k_f^6} \text{O}_2 + \text{M}$	$k_f^6 = 18.5 \times 10^{10} \times T^{-0.5}$	57

Note: Units for reaction rate data are liter, gm-mole, sec, and °K.

TABLE 5

SUMMARY OF PERFORMANCE RESULTS FOR CONTOURS STUDIED IN TASK II

Equilibrium starting conditions:

Contraction ratio: 2
Temperature (static): 5510° R
Pressure (static): 56.7 psia
Expansion area ratio (A/A_{\min}): 400.0

<u>Nozzle Configuration</u>	<u>Vacuum Specific Impulse</u>	<u>Average Molecular Weight at Exhaust</u>	<u>Mach No. @ A_{\min}</u>
I	467 sec	11.725	0.986
II	464 sec	11.690	0.985
III	473 sec	11.863	0.975
Equilibrium	485 sec	12.100	1.0
Frozen	449 sec	11.520	1.0

TABLE 6

FREEZING POINTS FOR DIFFERENT THROAT CONTOURS

Freezing points determined from
one-dimensional kinetic flow
calculations

Equilibrium starting conditions:

Contraction ratio: 2
Temperature (static): 5510° R
Pressure (static): 56.7 psia
Expansion area ratio (A/A_{\min}): 400.0

<u>Nozzle Configuration</u>	<u>$\frac{A}{A_{\min}}$ from γ</u>	<u>$\frac{A}{A_{\min}}$ from mean mol. wt.</u>
I	2.310	2.387
II	2.05	2.15
III	2.993	3.423

TABLE 7

OPTIMUM NOZZLE CONFIGURATION

AND FLOW PROPERTIES

Propellant System: H_2-O_2
 $P_c = 60$ psia
 $T_c = 5510$ °R
 $O/F = 2.0$

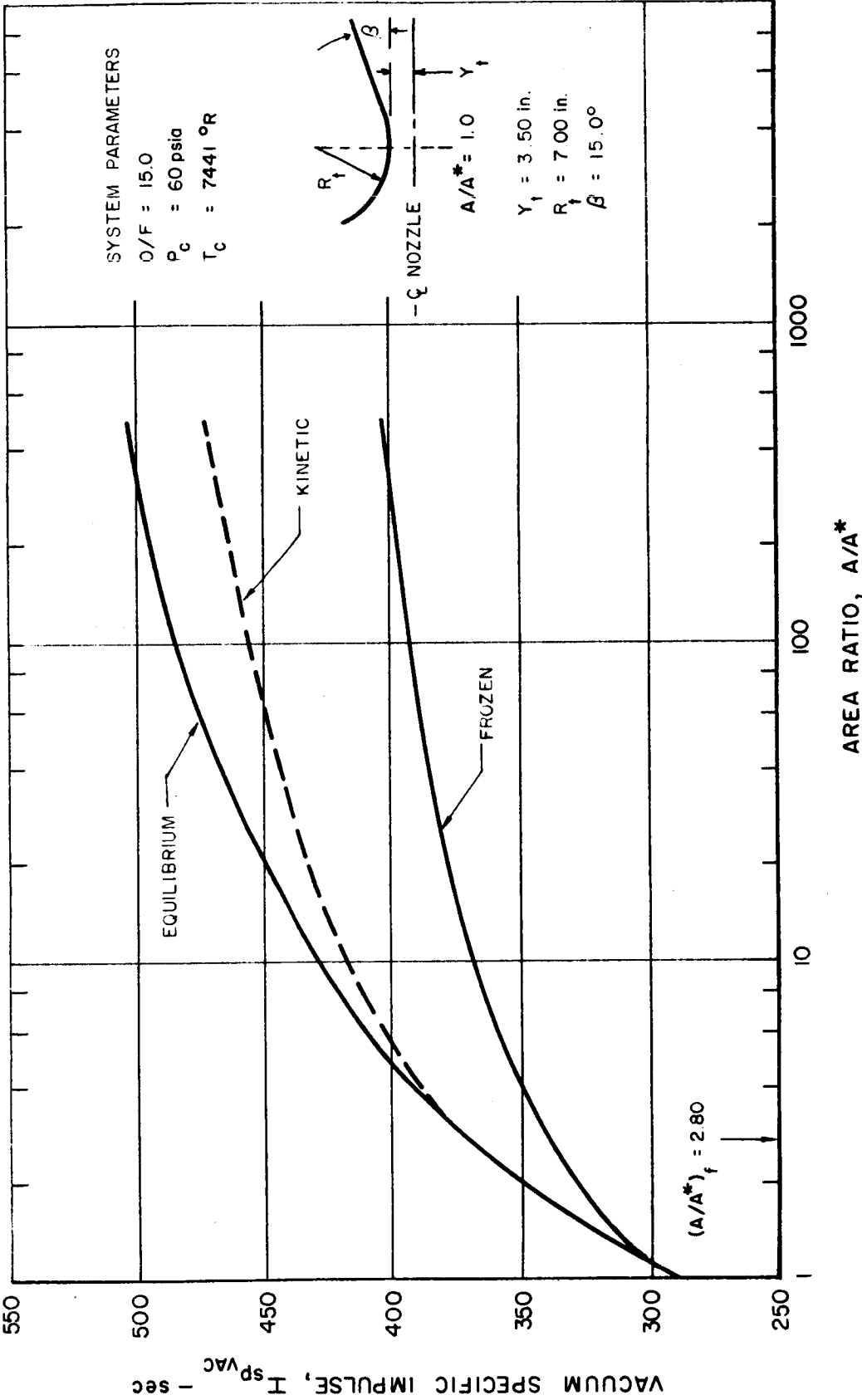
x/R_o	y/R_o	$T(^{\circ}R)$	ρ (lb _F /FT ²)	Mach no.	$t(\tan \theta)$
0.02753	1.00019	5155.29	4796.95	1.0050	0.01377
0.06198	1.00096	5085.47	4407.63	1.0788	0.03100
0.21127	1.01119	4902.38	3480.24	1.2660	0.10623
0.47642	1.05757	4585.65	2305.11	1.5526	0.24527
0.70511	1.12842	4274.21	1530.04	1.8095	0.37675
1.21889	1.40804	3551.19	562.95	2.3842	0.66732
1.29690	1.46038	3502.03	523.44	2.4244	0.67416
1.46956	1.57761	3404.11	451.66	2.5057	0.68388
1.69332	1.73117	3291.42	379.60	2.6012	0.68867
1.91346	1.88283	3194.06	325.50	2.6853	0.68917
2.18458	2.06912	3086.55	273.54	2.7803	0.68508
2.78975	2.47941	2888.65	196.23	2.9620	0.66918
3.24233	2.77896	2765.65	158.32	3.0799	0.65334
3.96339	3.24040	2601.67	117.59	3.2444	0.62642
5.32091	4.05904	2368.63	75.21	3.4956	0.58086
6.48642	4.71629	2217.29	55.33	3.6723	0.54734
8.05286	5.54267	2057.23	39.31	3.8740	0.50883
10.23364	6.60336	1888.14	26.79	4.1071	0.46551
13.91562	8.20992	1684.59	16.28	4.4234	0.41000
22.24061	11.25606	1405.90	7.58	4.9451	0.32851
30.15698	13.64787	1245.47	4.61	5.3120	0.27834
40.38052	16.24917	1107.75	2.88	5.6834	0.23284
49.74124	18.27571	1017.48	2.05	5.9639	0.20141
60.83360	20.34522	938.04	1.49	6.2416	0.17273

FIG. 1

VACUUM SPECIFIC IMPULSE VS AREA RATIO

$H_2 - F_2$

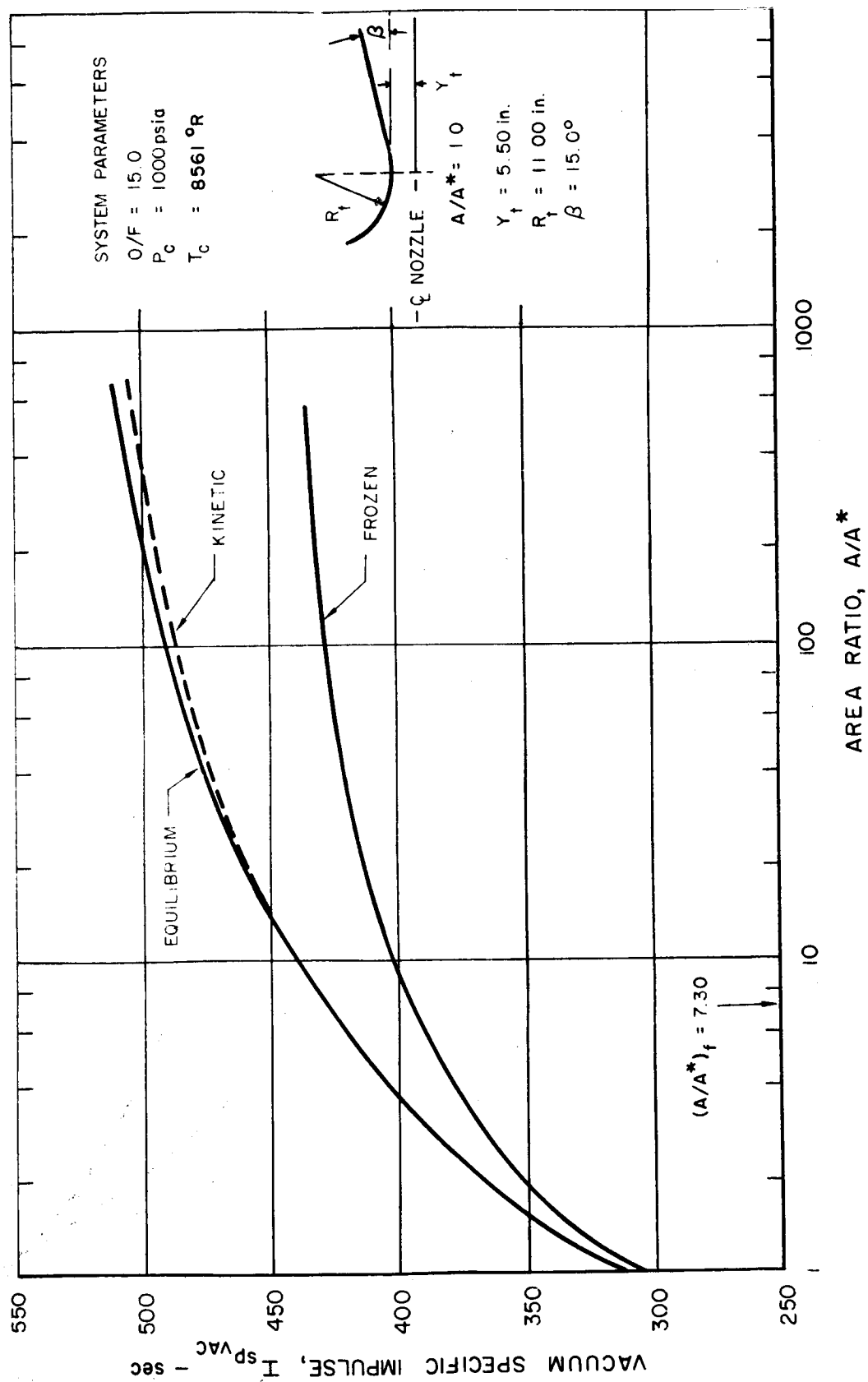
CHAMBER PRESSURE = 60 psia



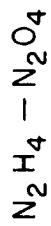
VACUUM SPECIFIC IMPULSE VS AREA RATIO

 $H_2 - F_2$

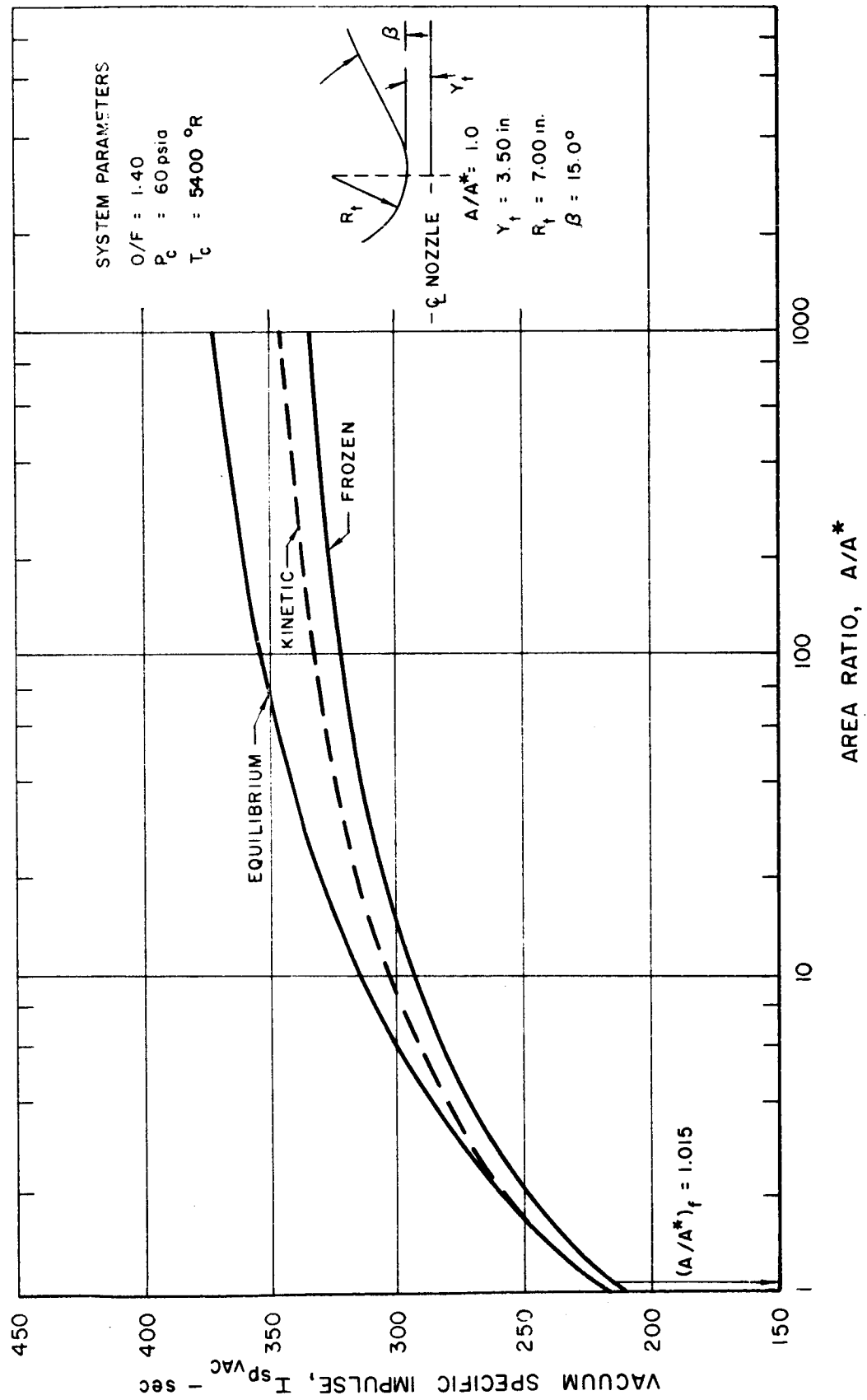
CHAMBER PRESSURE = 1000 psia



VACUUM SPECIFIC IMPULSE VS AREA RATIO



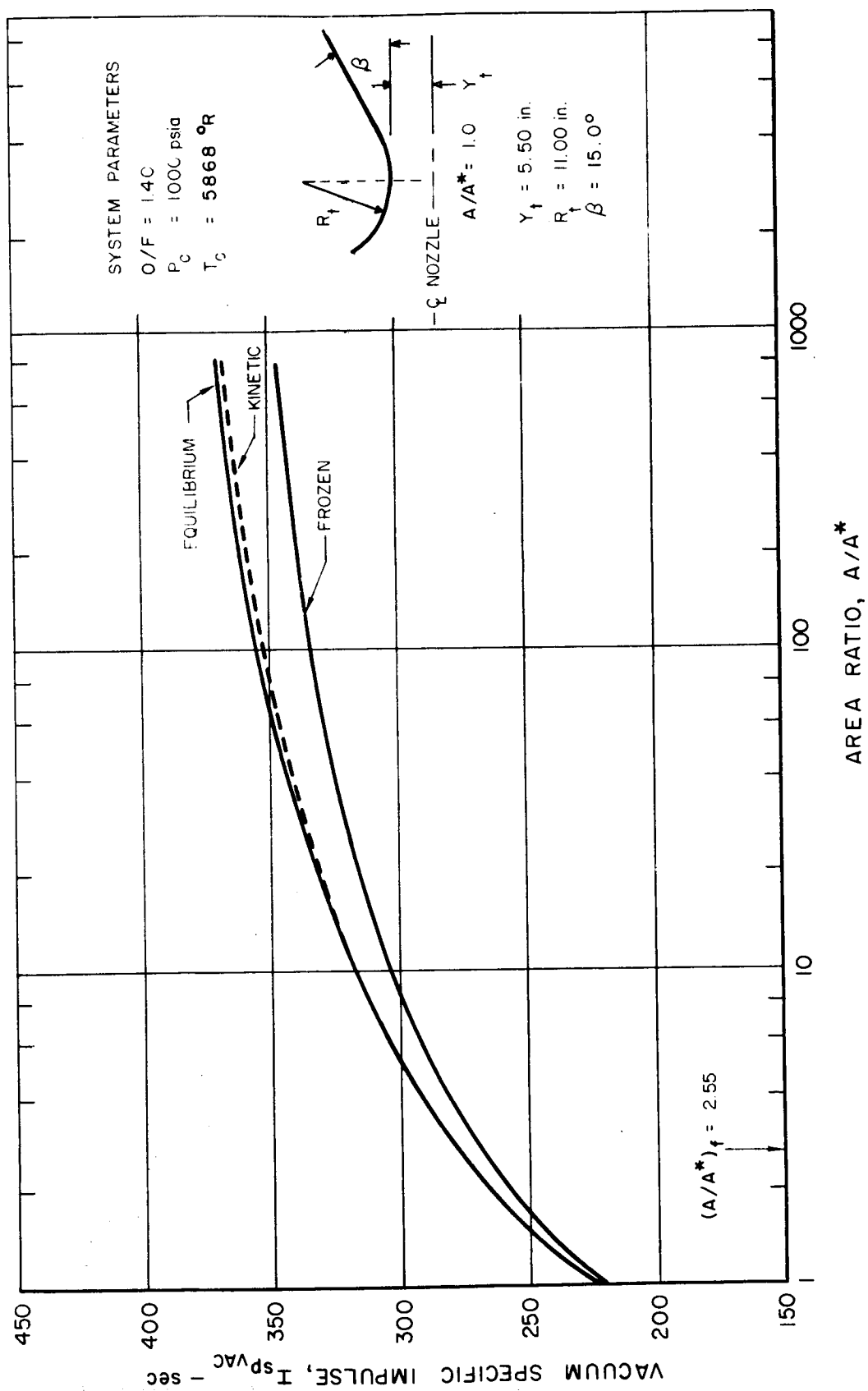
CHAMBER PRESSURE = 60 psia



VACUUM SPECIFIC IMPULSE VS AREA RATIO



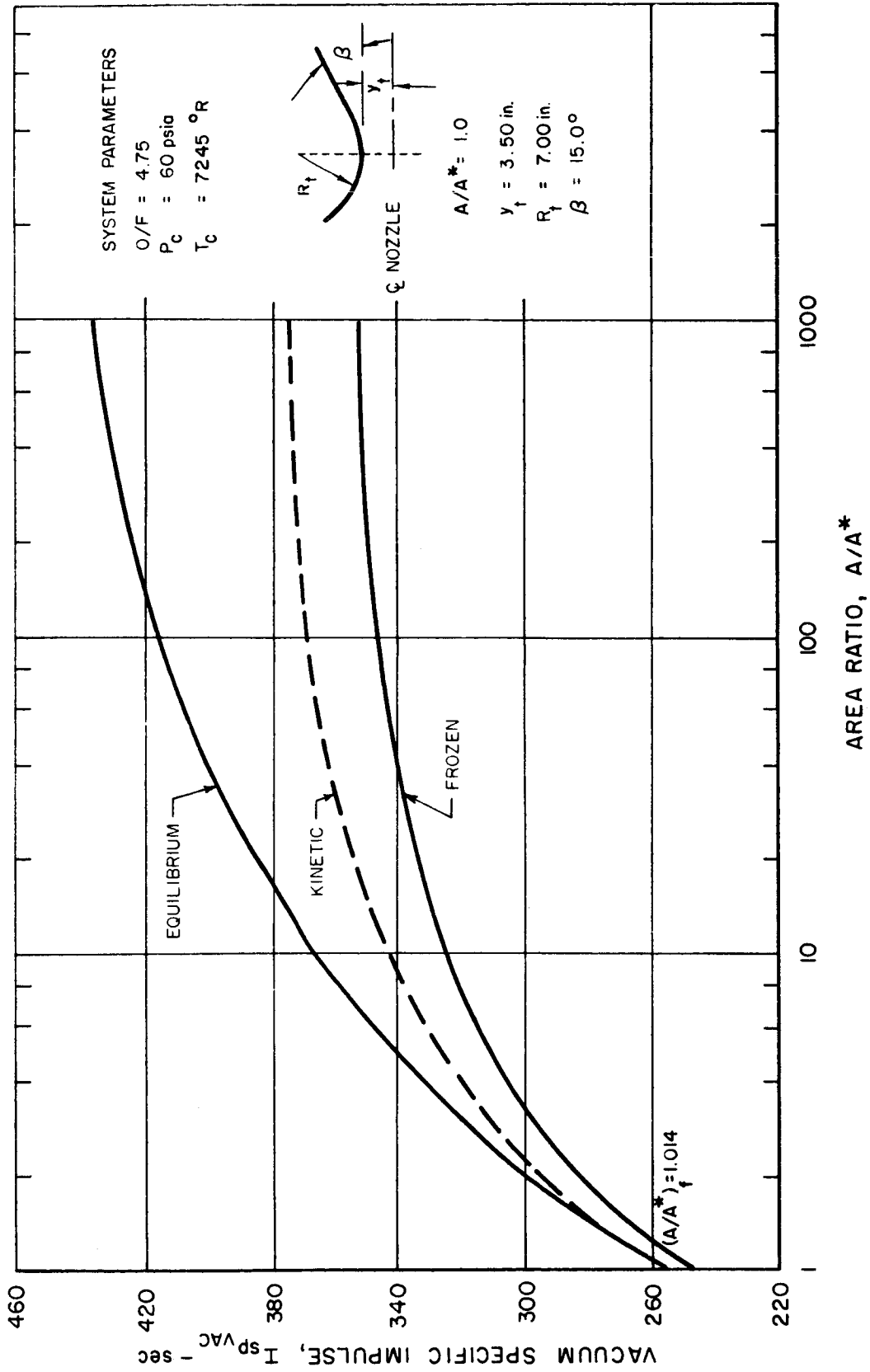
CHAMBER PRESSURE = 1000 psia



VACUUM SPECIFIC IMPULSE VERSUS AREA RATIO

$C_6H_{14} - OF_2$

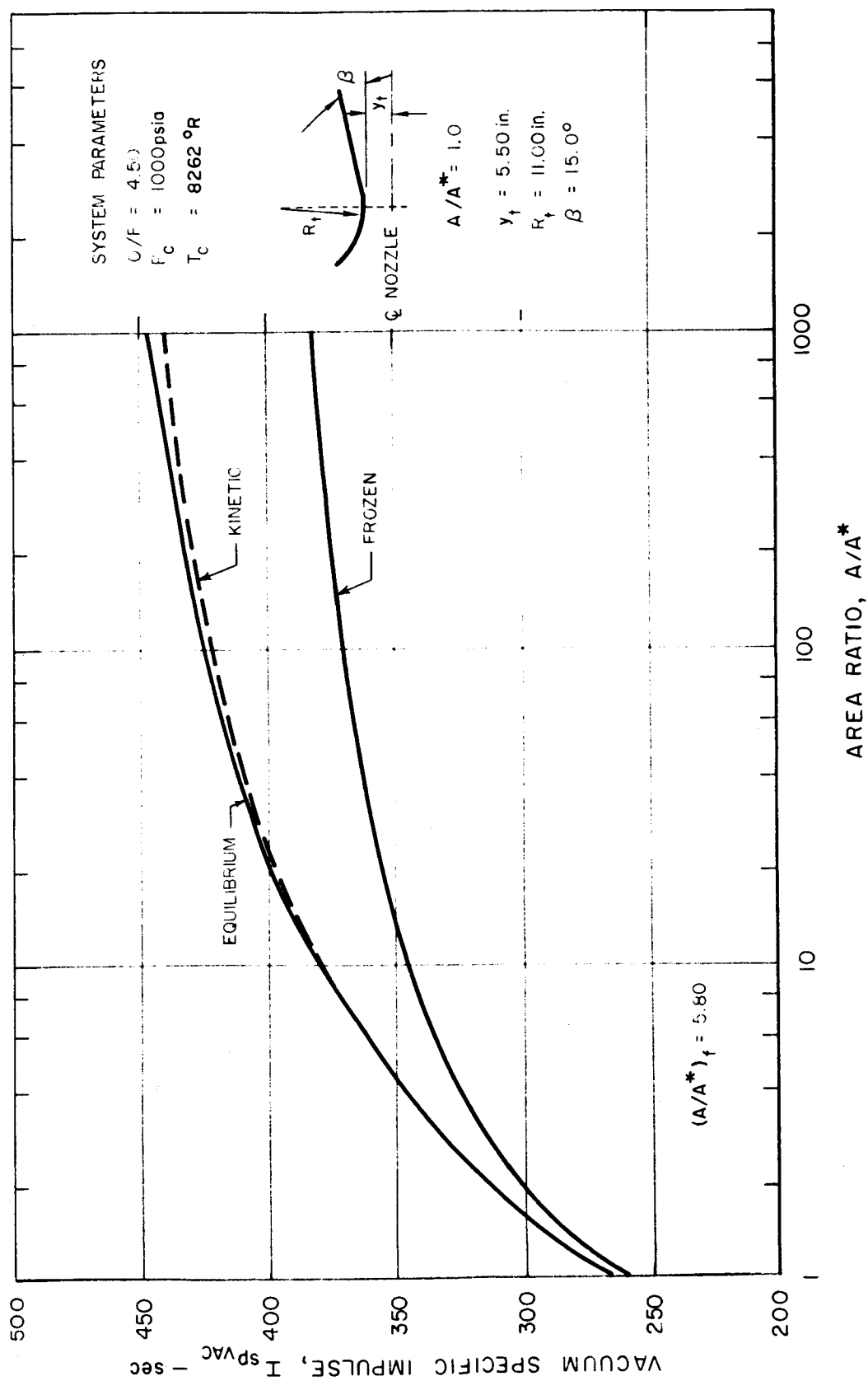
CHAMBER PRESSURE = 60 psia



VACUUM SPECIFIC IMPULSE VERSUS AREA RATIO

 $C_6H_{14} - OF_2$

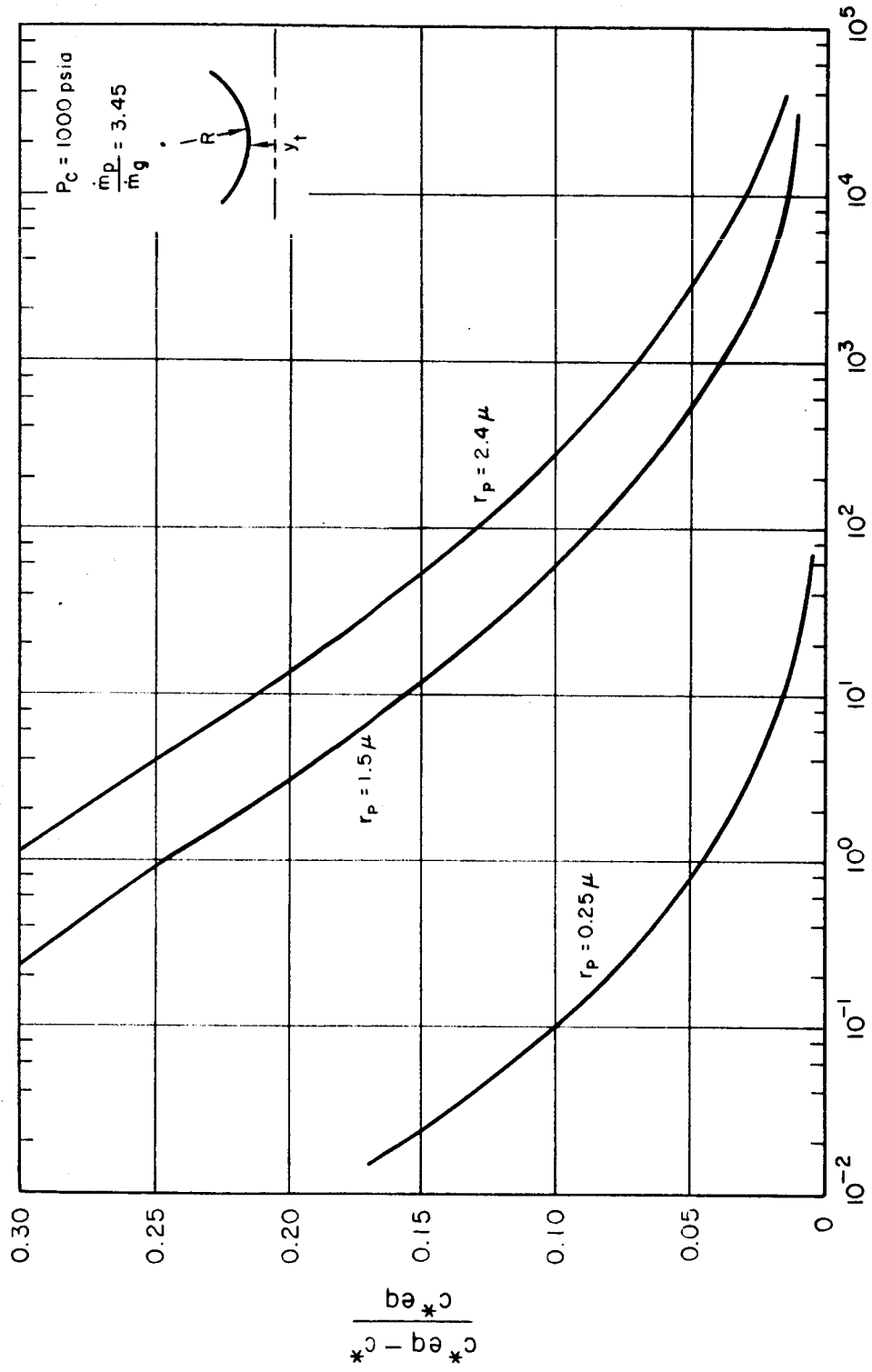
CHAMBER PRESSURE = 1000 psia



LOSS IN CHARACTERISTIC VELOCITY VERSUS THROAT GEOMETRY FOR TWO-PHASE FLOW

Be - H₂ - O₂ SYSTEM

CHAMBER PRESSURE = 1000 psia



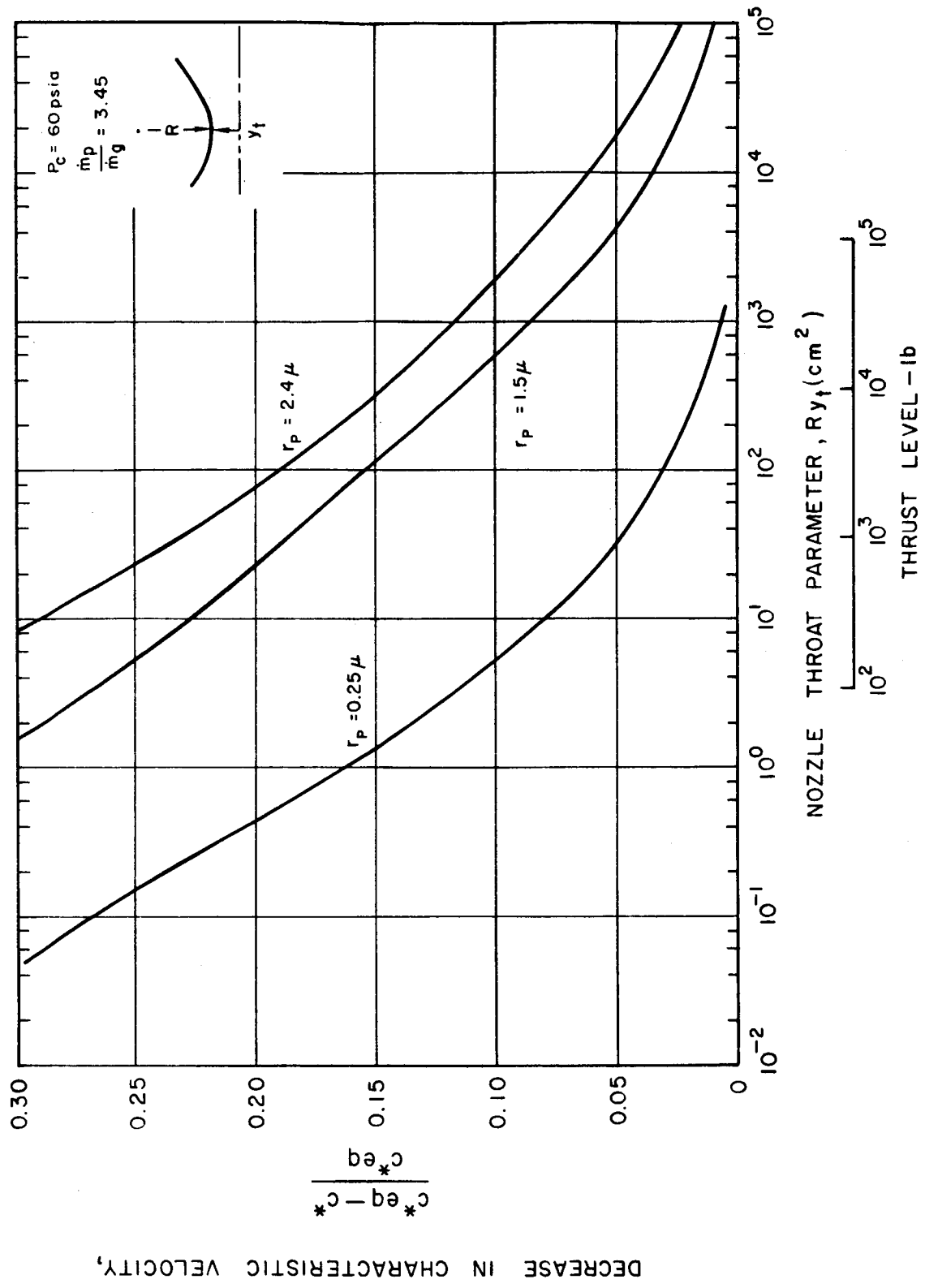
NOZZLE THROAT PARAMETER, Ry (cm²)

THRUST LEVEL - Ib

LOSS IN CHARACTERISTIC VELOCITY VERSUS
THROAT GEOMETRY FOR TWO-PHASE FLOW

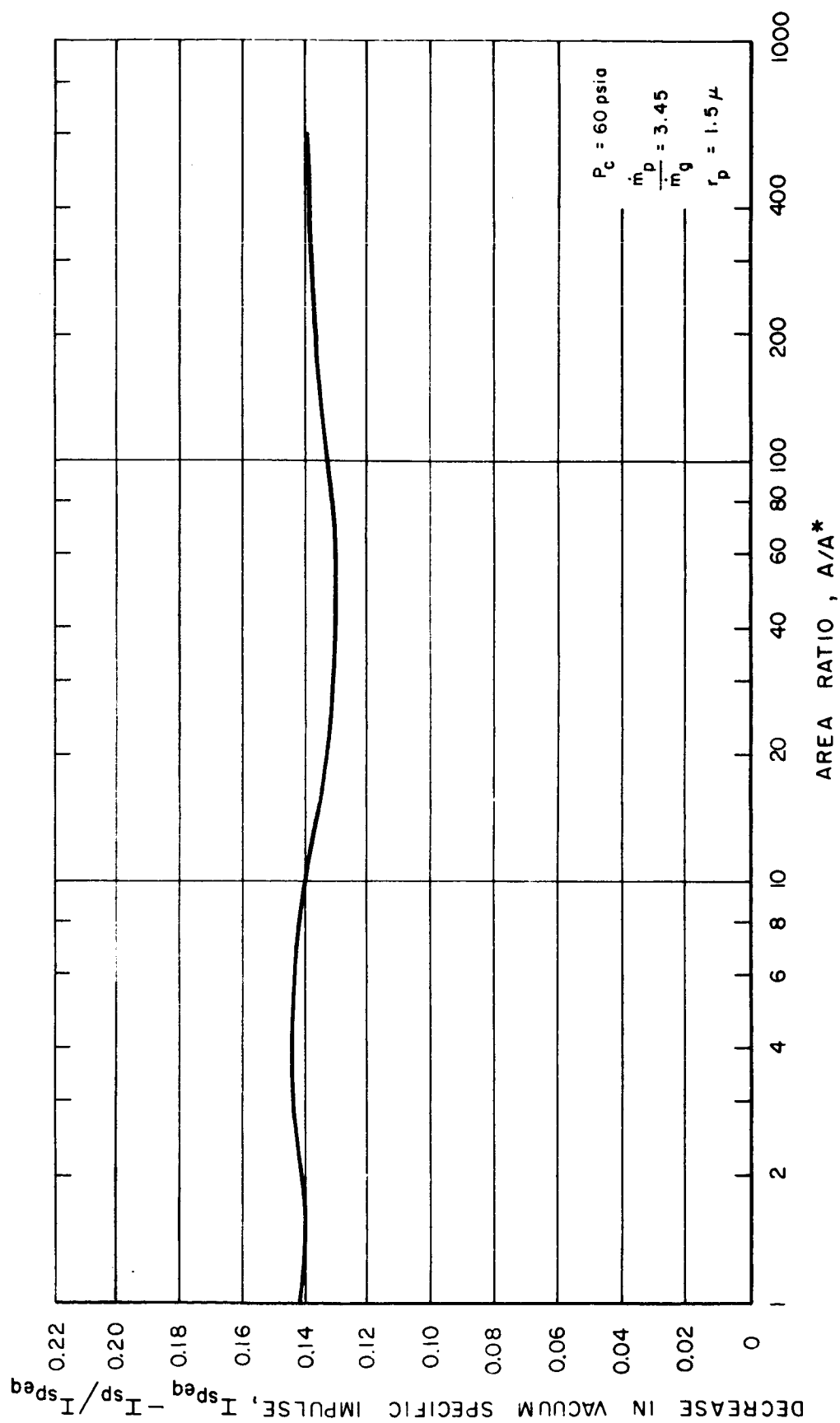
Be - H₂ - O₂ SYSTEM

CHAMBER PRESSURE = 60 psia



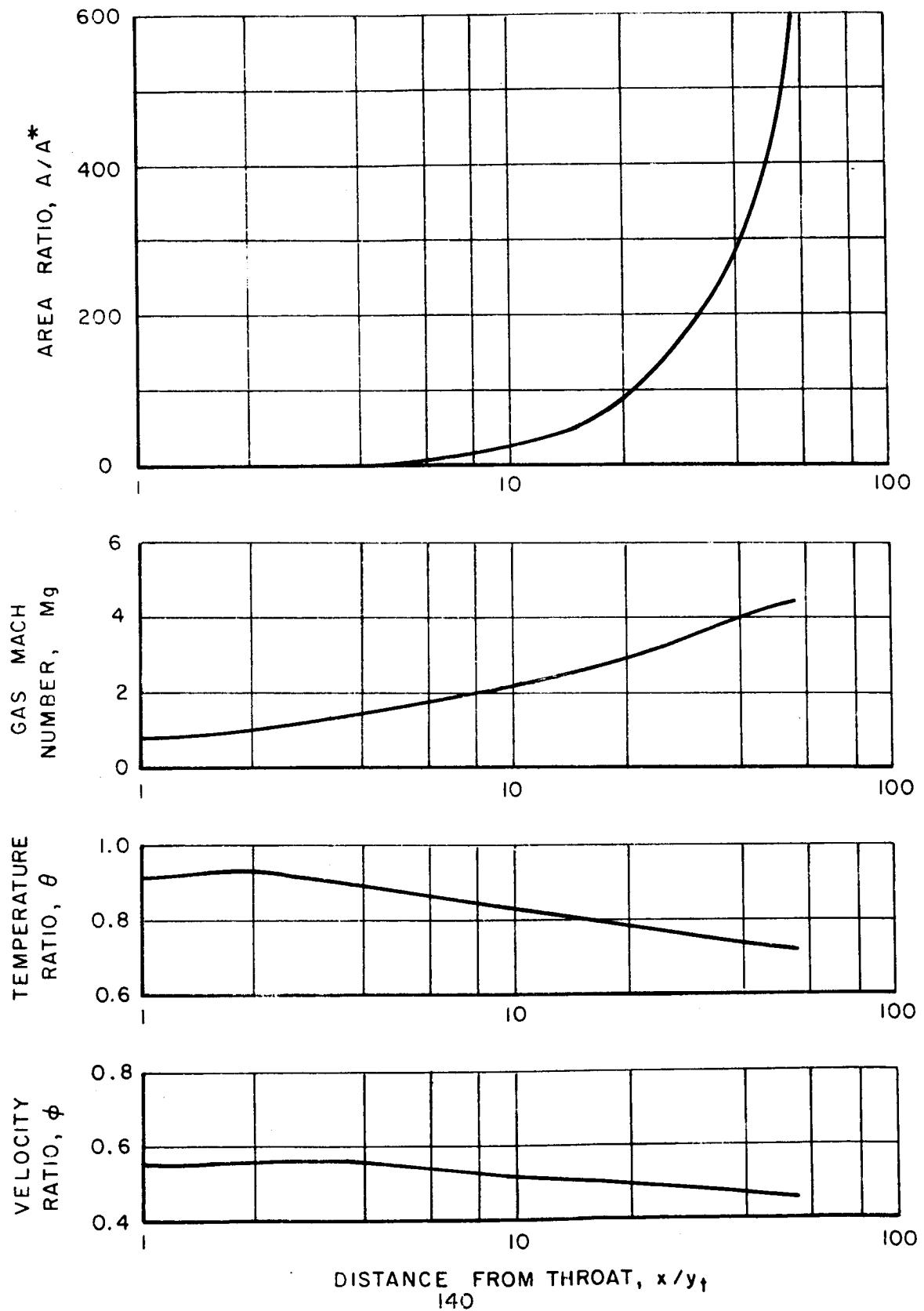
LOSS IN VACUUM SPECIFIC IMPULSE VERSUS AREA RATIO FOR TWO PHASE FLOW

Be - H₂ - O₂ SYSTEM

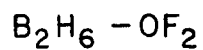


VARIATION OF NOZZLE PARAMETERS IN NOZZLE EXIT CONE

$$P_c = 60 \text{ psia}, \quad \dot{m}_p / \dot{m}_g = 3.45, \quad r_p = 1.5 \mu$$

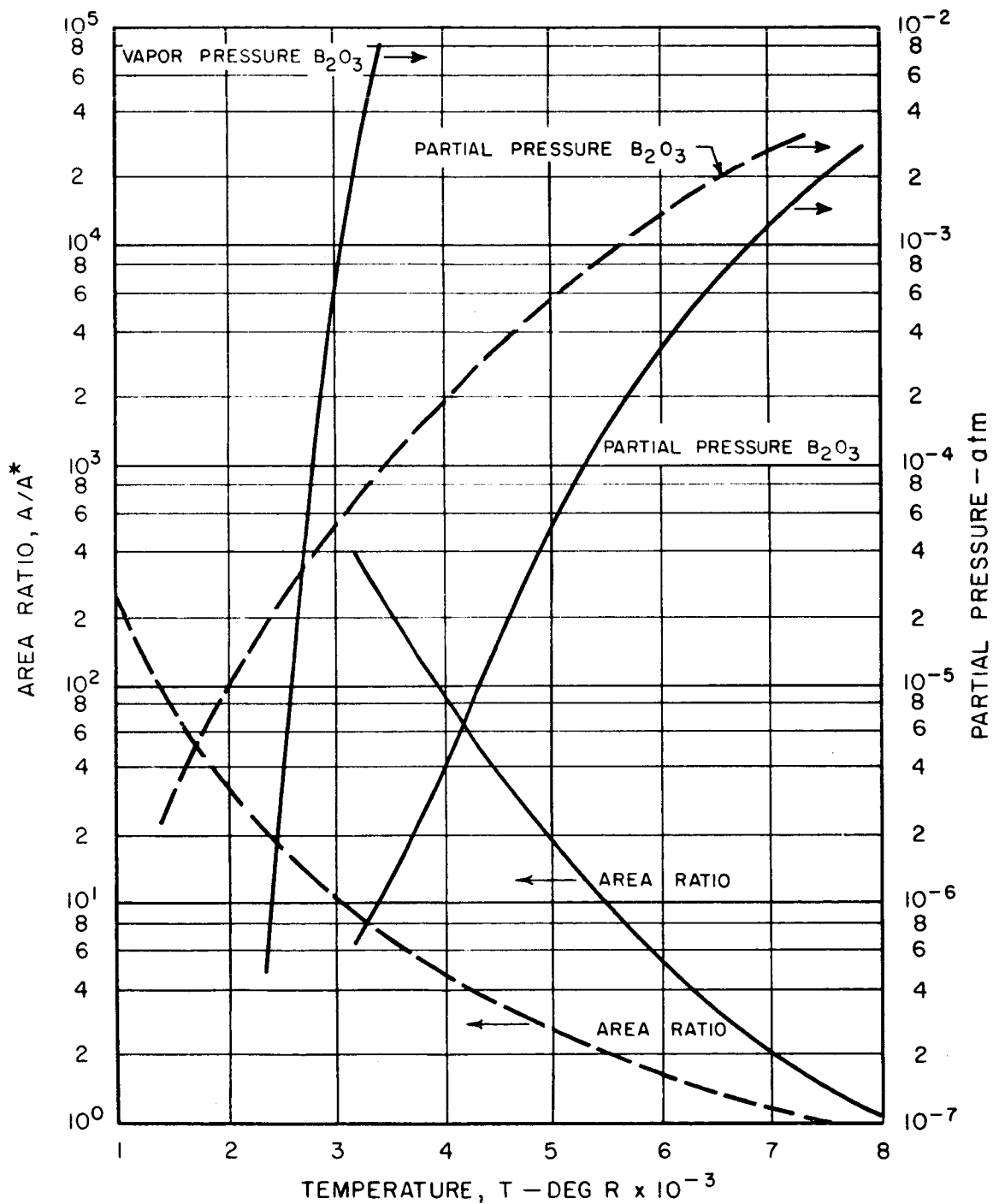


PARTIAL PRESSURE B_2O_3 VERSUS AREA RATIO AND TEMPERATURE


 $P_c = 1000 \text{ psia}$
 $O/F = 3.8$

— EQUILIBRIUM

-- FROZEN



PARTIAL PRESSURE B_2O_3 VERSUS AREA RATIO AND TEMPERATURE

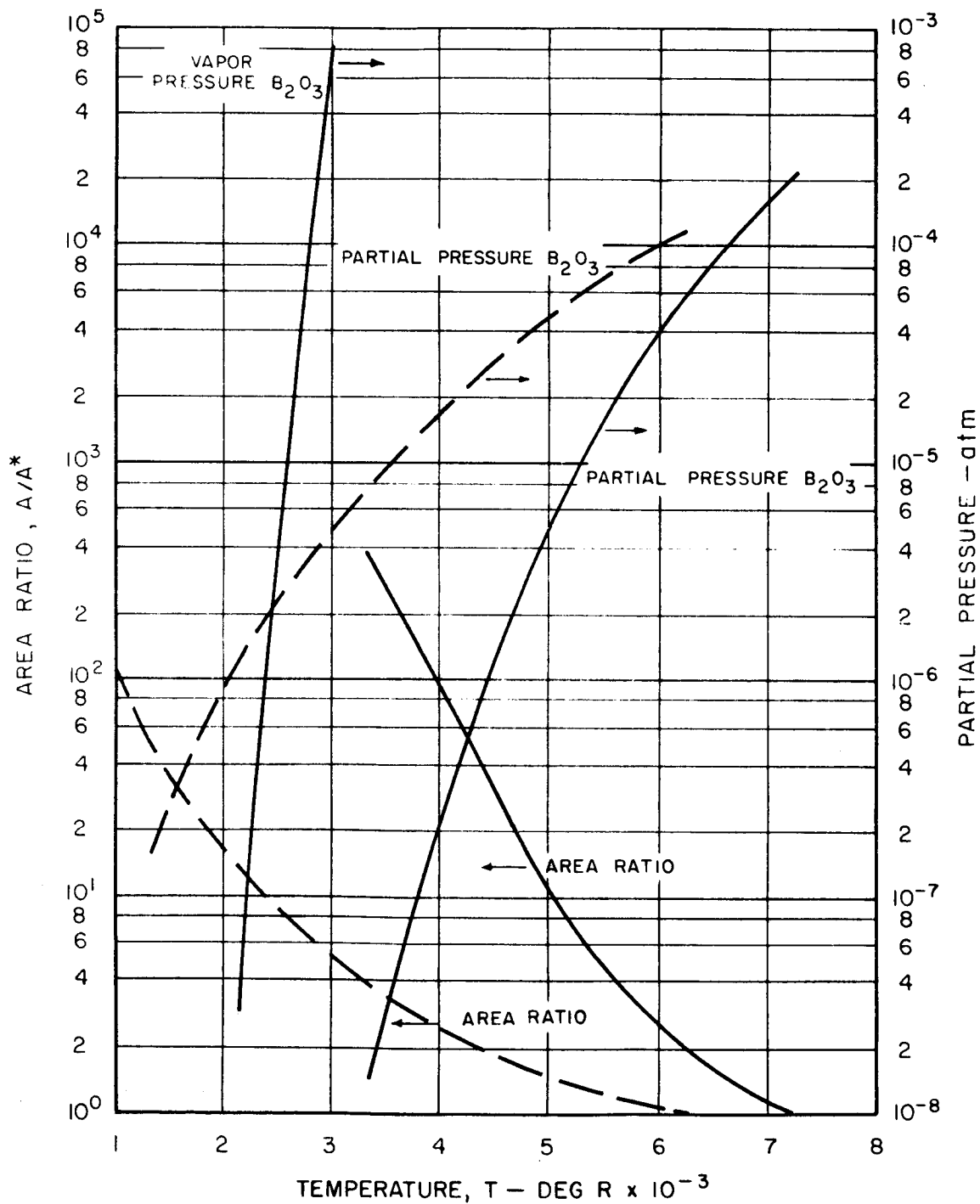
$B_2H_6 - OF_2$

$P_c = 60$ psia

$O/F = 3.8$

— EQUILIBRIUM

-- FROZEN



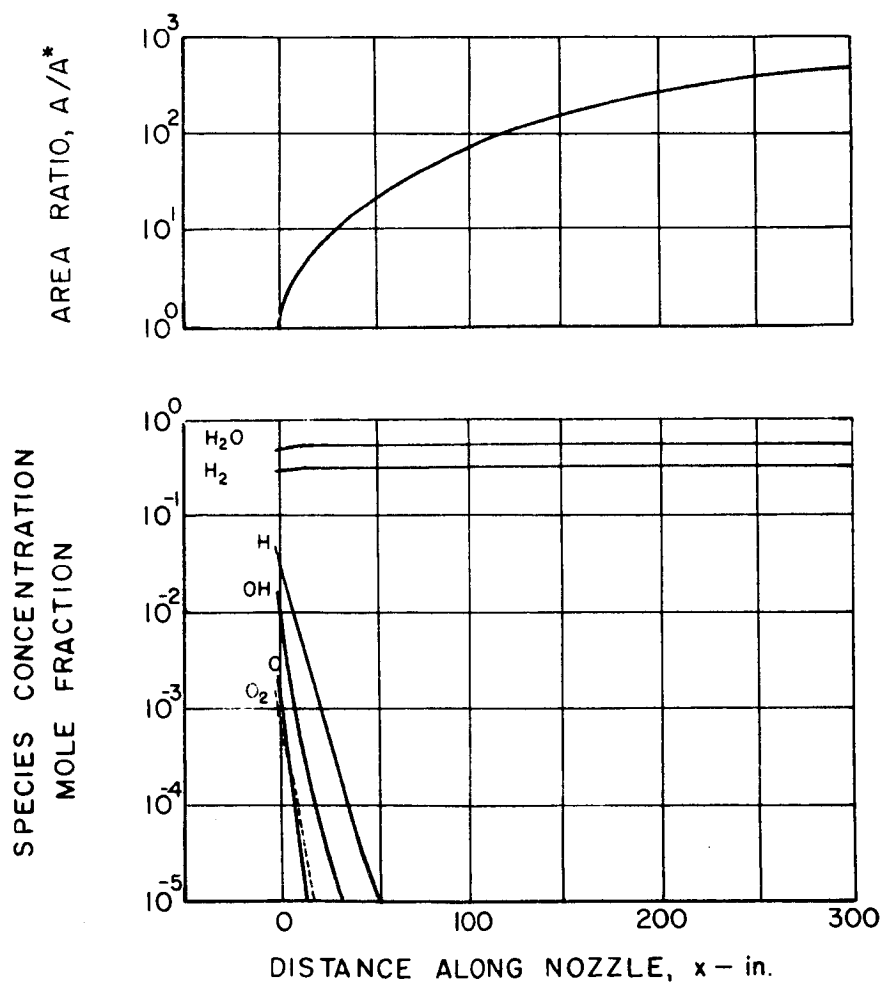
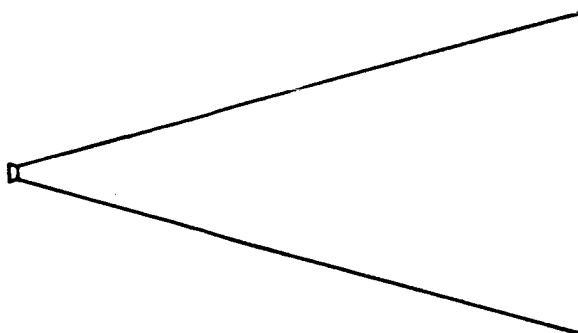
VARIATION OF AREA RATIO AND SPECIES CONCENTRATION IN HYPOTHETICAL NOZZLE CONFIGURATION

$H_2 - O_2$, $O/F = 5$

EQUILIBRIUM FLOW

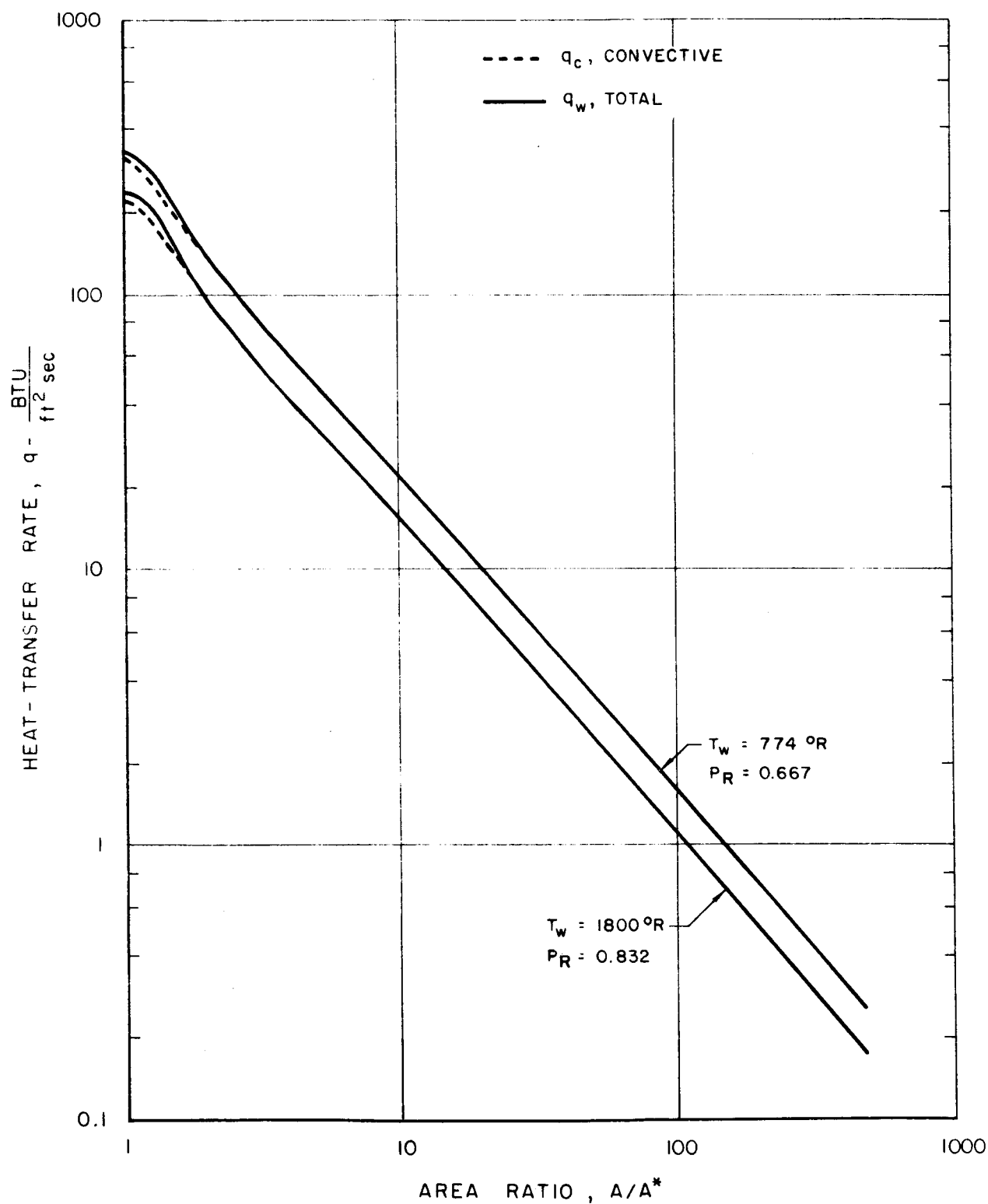
CHAMBER PRESSURE = 60 psia

CHAMBER TEMPERATURE = 5508 °R



HEAT - TRANSFER RATE FOR H_2-O_2 NOZZLE

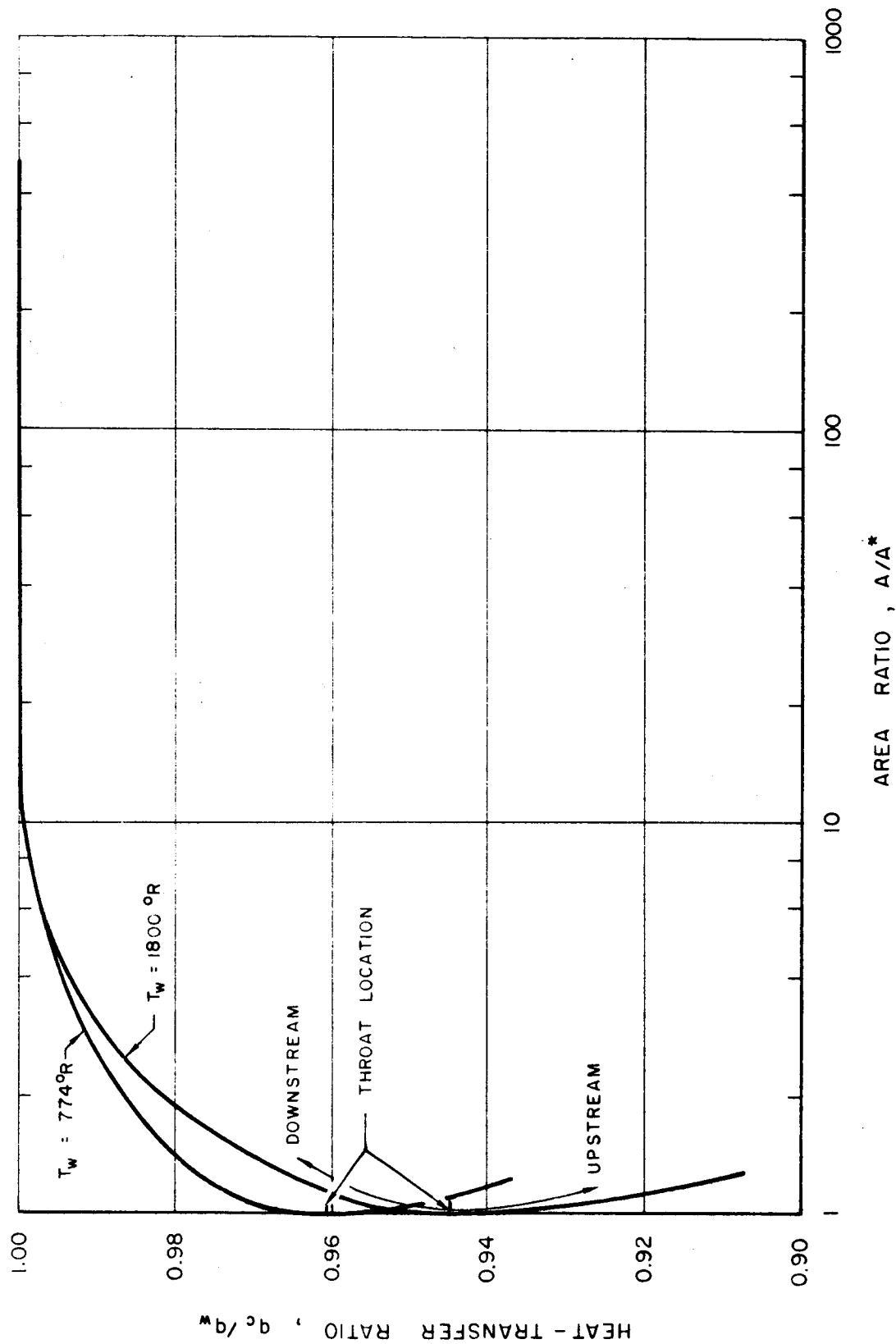
$P_c = 60$ psia
 $O/F = 5$
THRUST = 5000 lb

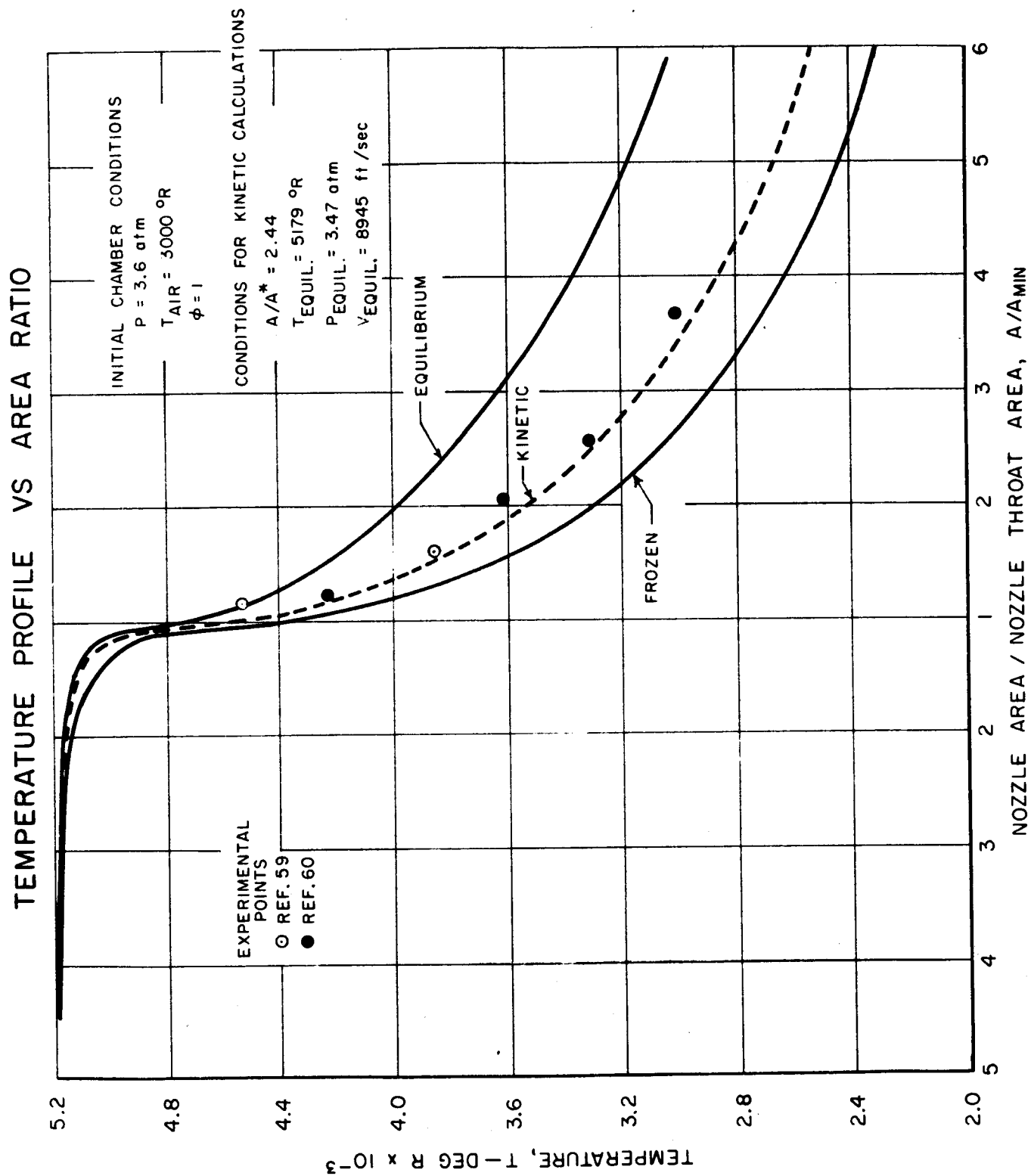


RATIO OF CONVECTIVE TO TOTAL HEAT TRANSFER FOR H_2-O_2 NOZZLE

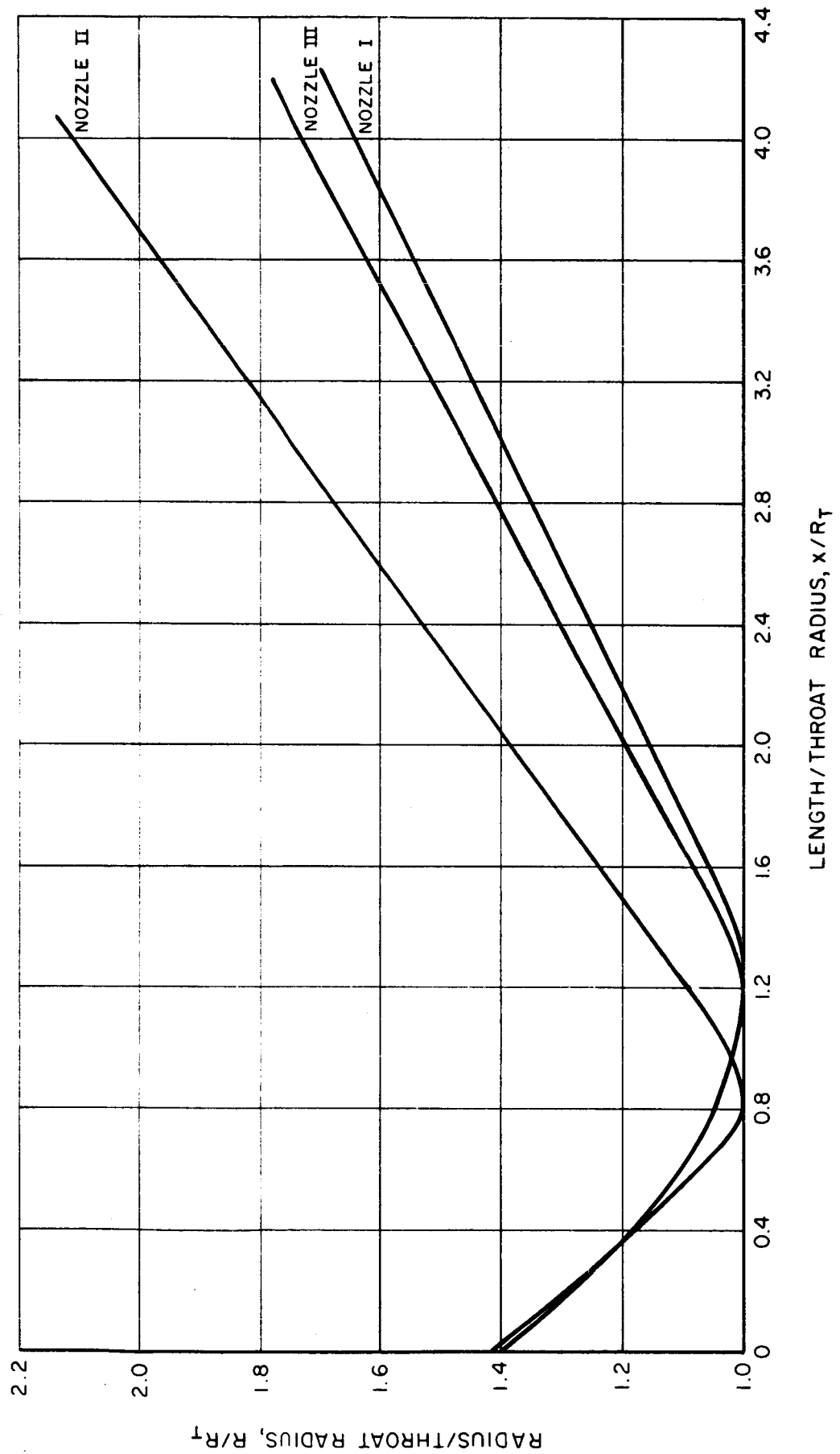
 $P_c = 60 \text{ psia}$
 $O/F = 5$

THRUST = 5000 lb





NOZZLE CONTOURS FOR ONE-DIMENSIONAL STUDIES



VACUUM SPECIFIC IMPULSE VERSUS AREA RATIO

NOZZLE CONTOURS I AND II

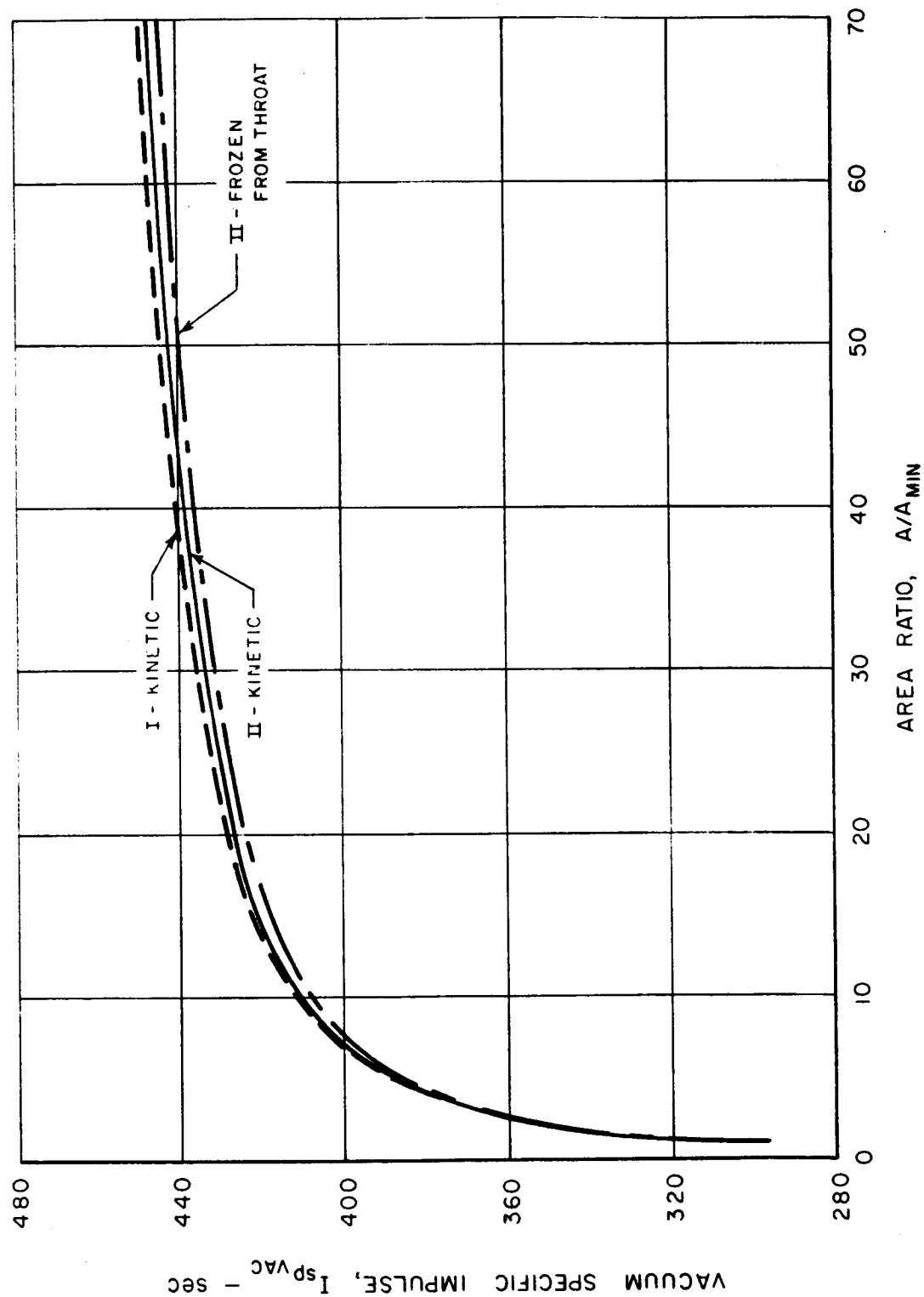
PROPELLANT: $H_2 - O_2$

EQUILIBRIUM CHAMBER CONDITIONS:

$T = 5540^\circ R$

$P = 60 \text{ psia}$

$O/F = 5$



VACUUM SPECIFIC IMPULSE VERSUS AREA RATIO

NOZZLE CONTOURS I AND II CONT'D

PROPELLANT: $H_2 - O_2$
 EQUILIBRIUM CHAMBER CONDITIONS:
 $T = 5540^\circ R$
 $P = 60 \text{ psia}$
 $O/F = 5$

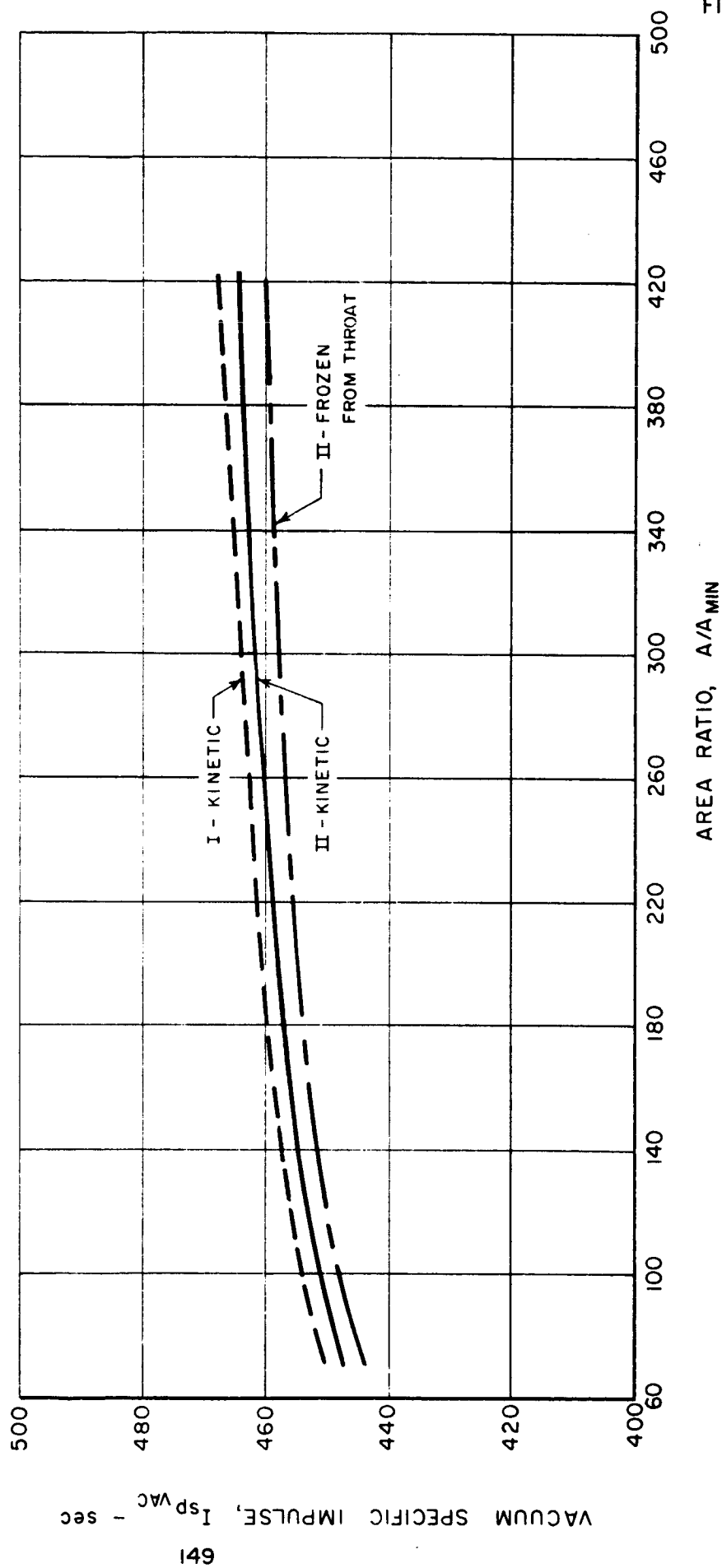


FIG. 19

MEAN MOLECULAR WEIGHT VERSUS MACH NUMBER

NOZZLE CONTOURS I, II, AND III

PROPELLANT: $H_2 - O_2$

EQUILIBRIUM CHAMBER CONDITIONS:

$T = 5540^\circ R$

$P = 60 \text{ psia}$

$O/F = 5$

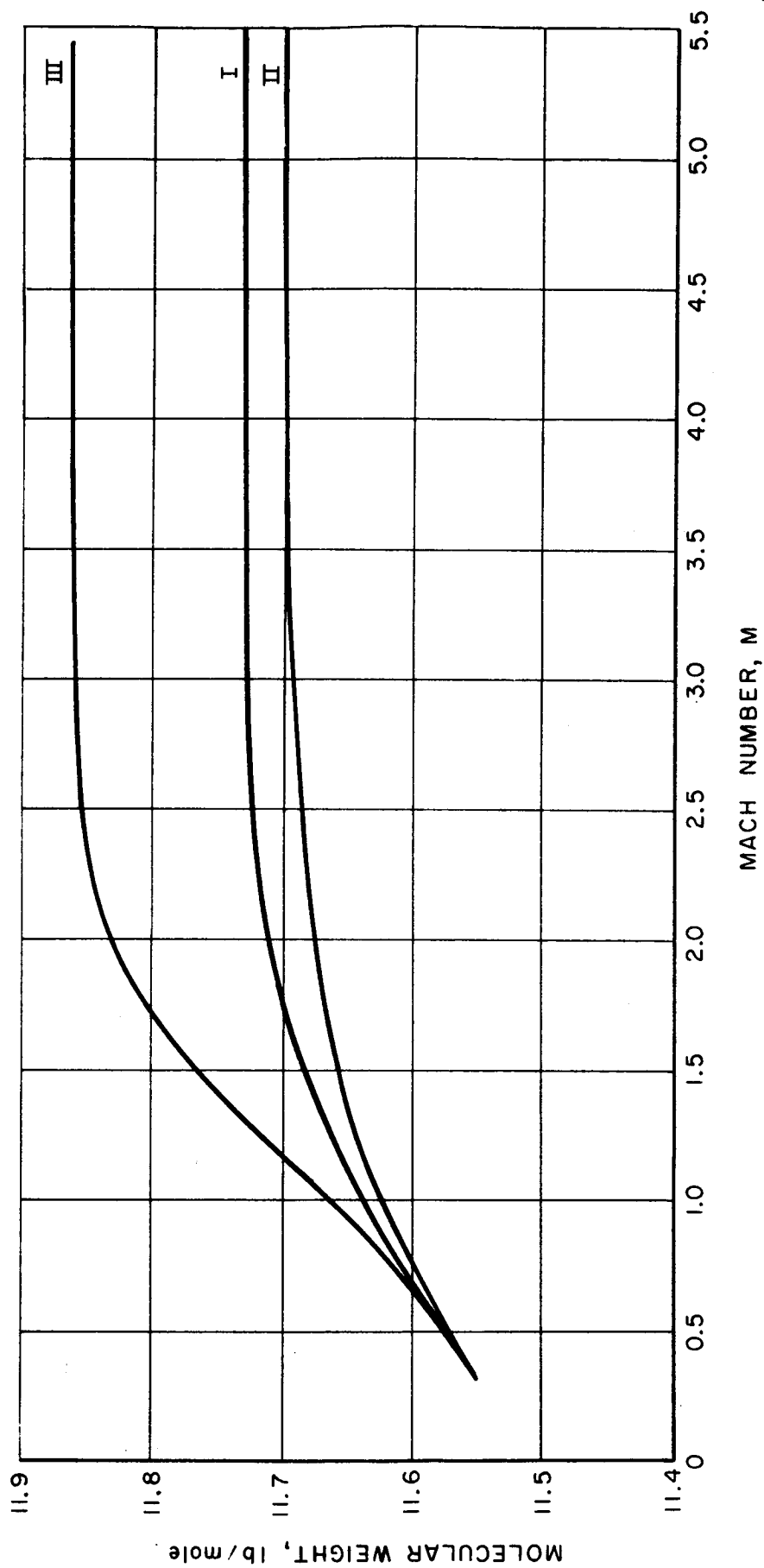


FIG. 20

SCALING EFFECT : TEMPERATURE VERSUS AREA RATIO

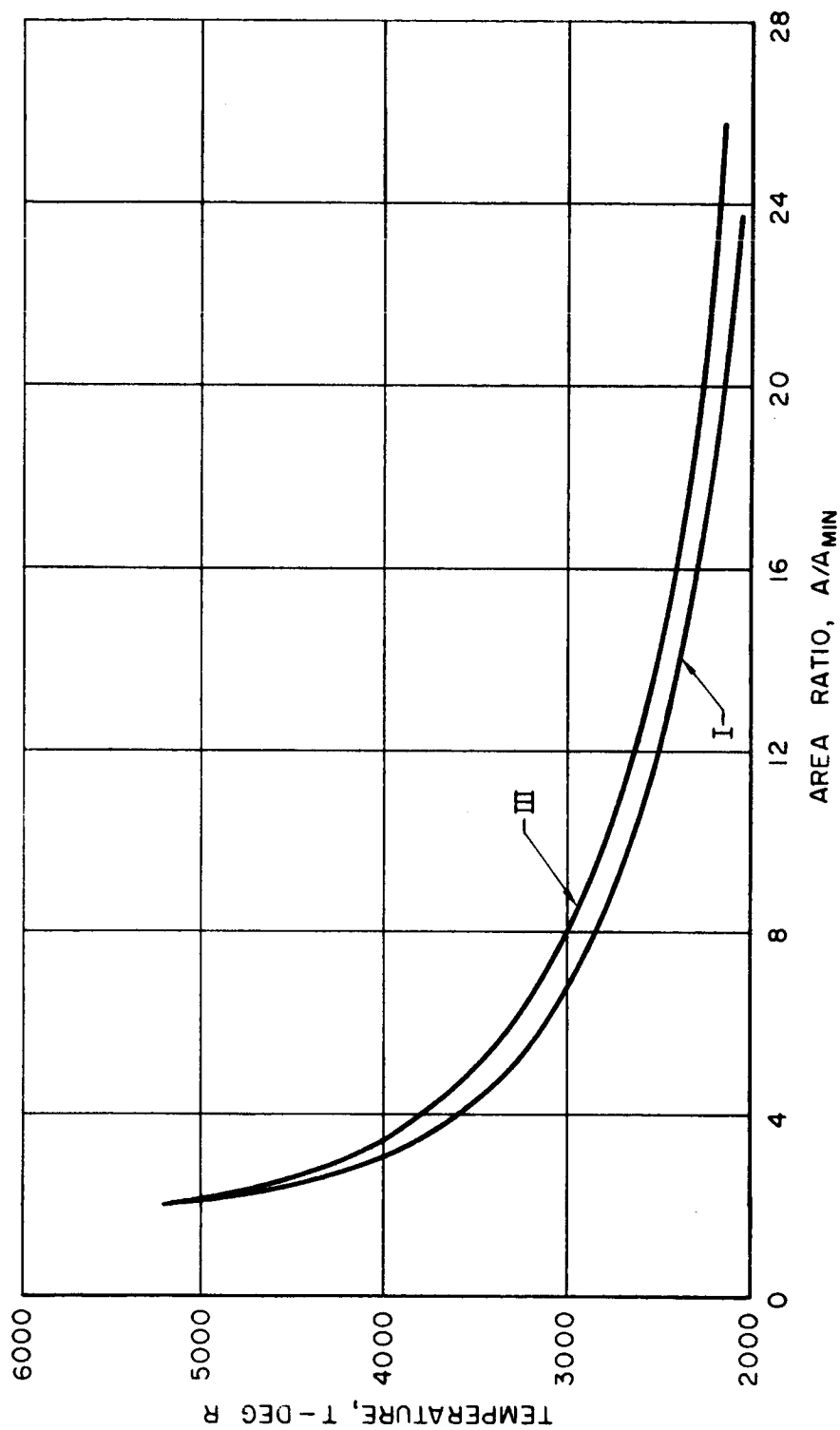
NOZZLE CONTOURS I AND III

PROPELLANT : $H_2 - O_2$
EQUILIBRIUM CHAMBER CONDITIONS:

$T = 5540^\circ R$

$P = 60$ psia

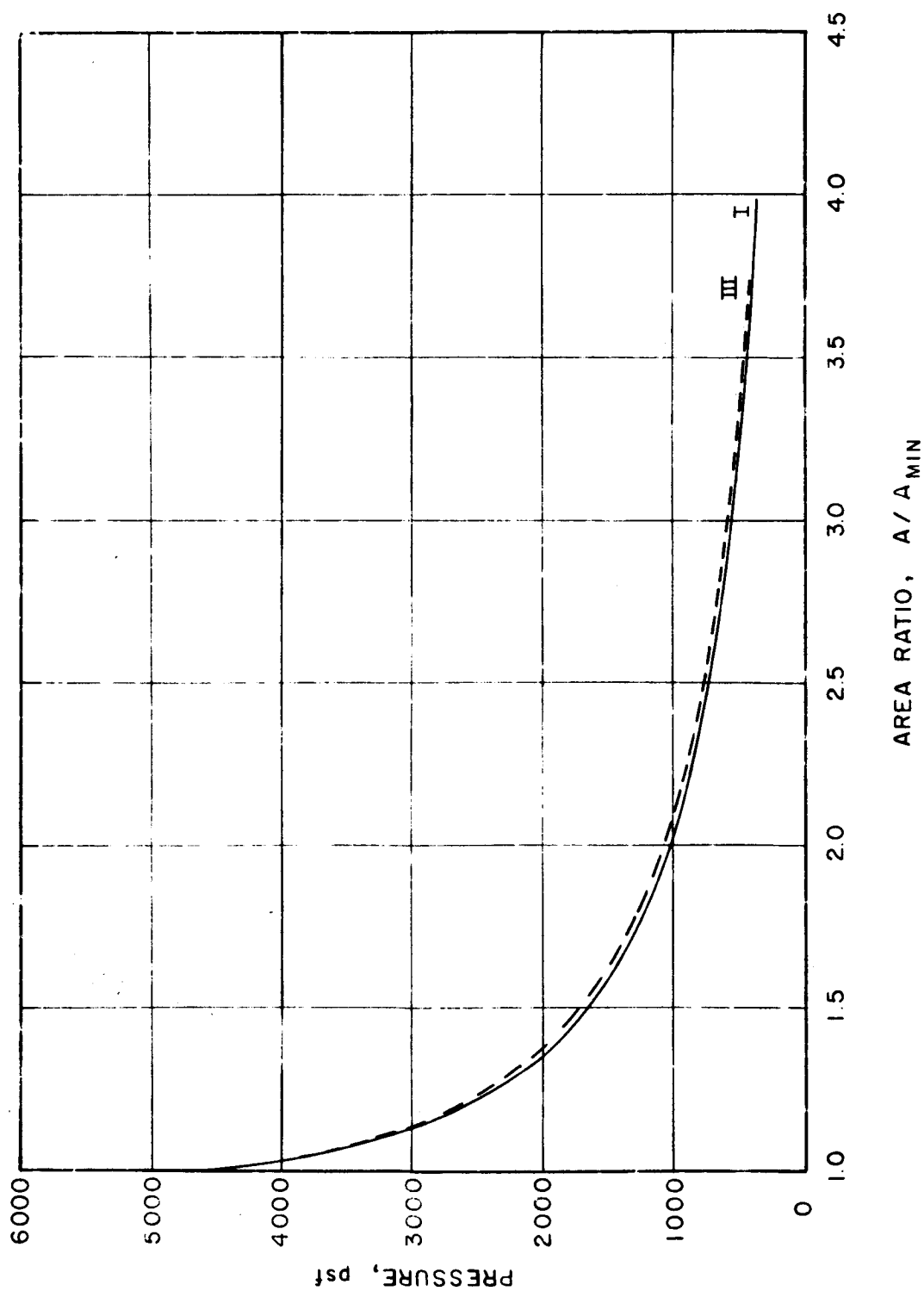
$O/F = 5$



SCALING EFFECT : PRESSURE VERSUS AREA RATIO

NOZZLE CONTOURS I AND III

PROPELLANT $H_2 - O_2$
 EQUILIBRIUM CHAMBER CONDITIONS:
 $T = 5540^\circ R$
 $P = 60 \text{ psia}$
 $O/F = 5$



SCALING EFFECT : MEAN MOLECULAR WEIGHT VERSUS MACH NUMBER

NOZZLE CONTOURS I AND III

PROPELLANT : H_2-O_2
 EQUILIBRIUM CHAMBER CONDITIONS:
 $T = 5540^\circ R$
 $P = 60 \text{ psia}$
 $O/F = 5$

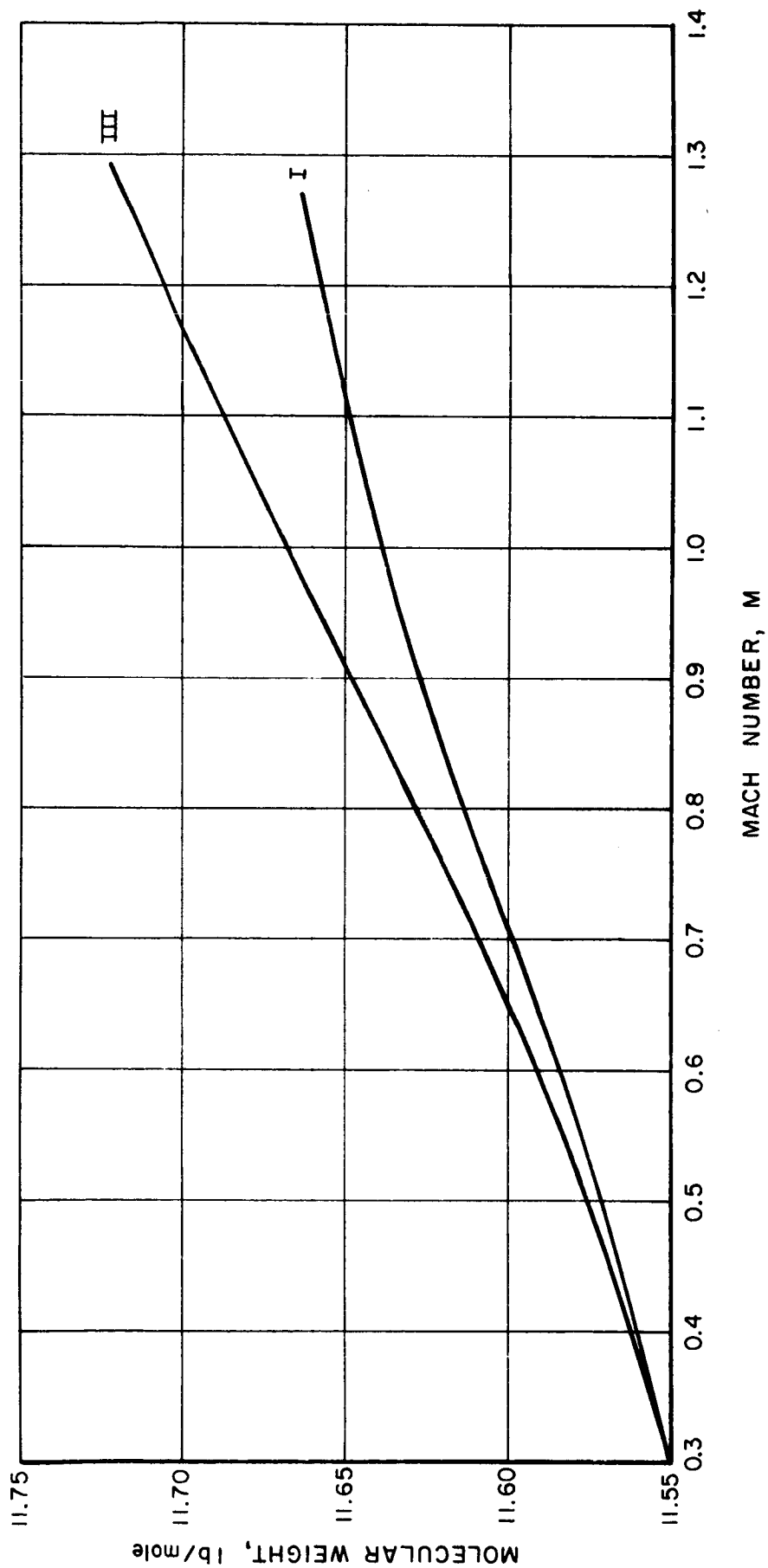


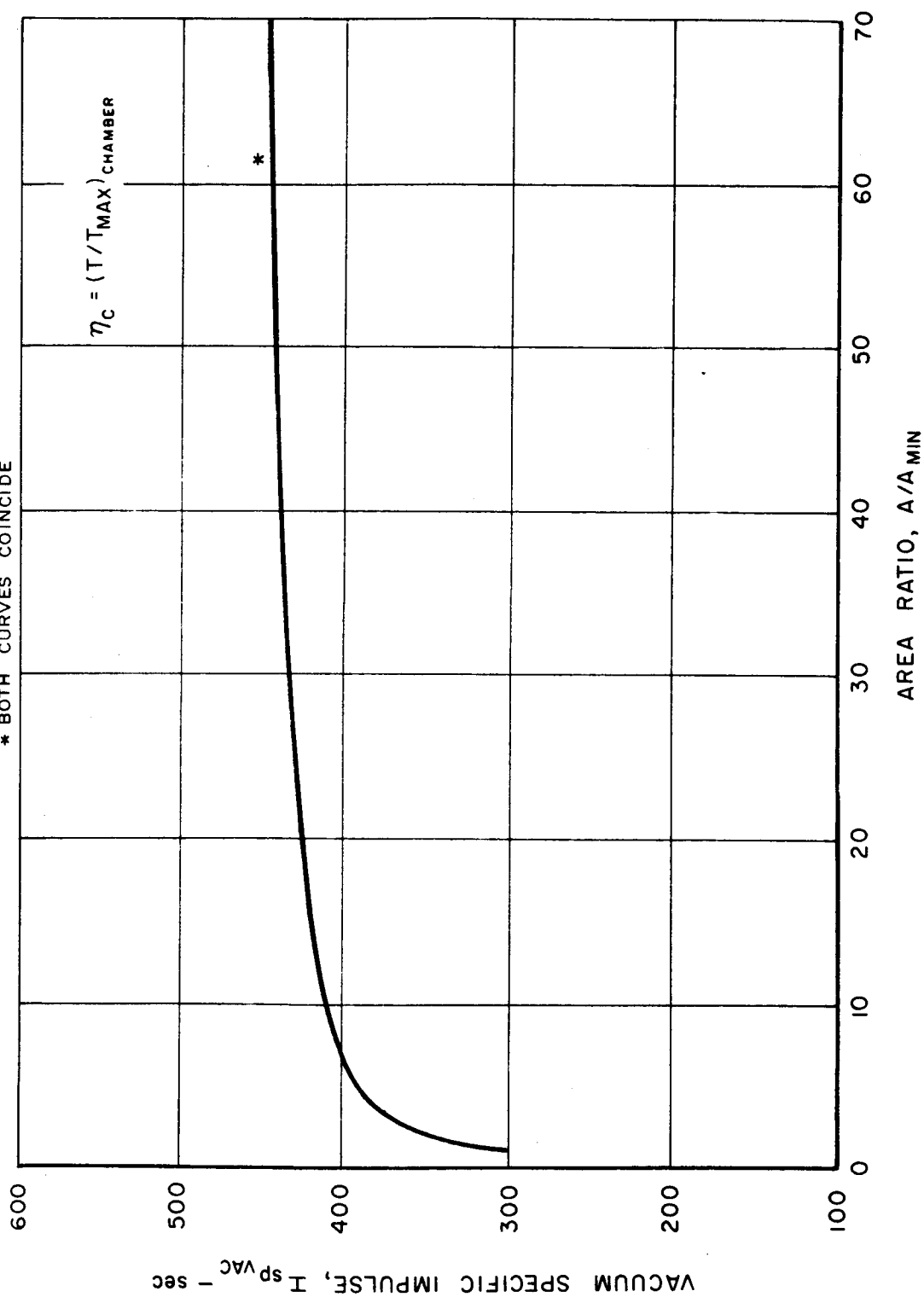
FIG. 23

COMBUSTION EFFICIENCY: VACUUM SPECIFIC IMPULSE VERSUS AREA RATIO

NOZZLE CONTOUR II

PROPELLANT: H_2-O_2 $O/F = 5$ NOZZLE ENTRANCE CONDITIONS: $5470^\circ R - 56.7 \text{ psia} - \eta_c = 0.98$ $5540^\circ R - 60.0 \text{ psia} - \eta_c = 1.00$

* BOTH CURVES COINCIDE



COMBUSTION EFFICIENCY : TEMPERATURE VERSUS AREA RATIO

NOZZLE CONTOUR II

PROPELLANT : H_2-O_2

O/F = 5

NOZZLE ENTRANCE CONDITIONS : 5470 °R - 56.7 psia

5540 °R - 60.0 psia

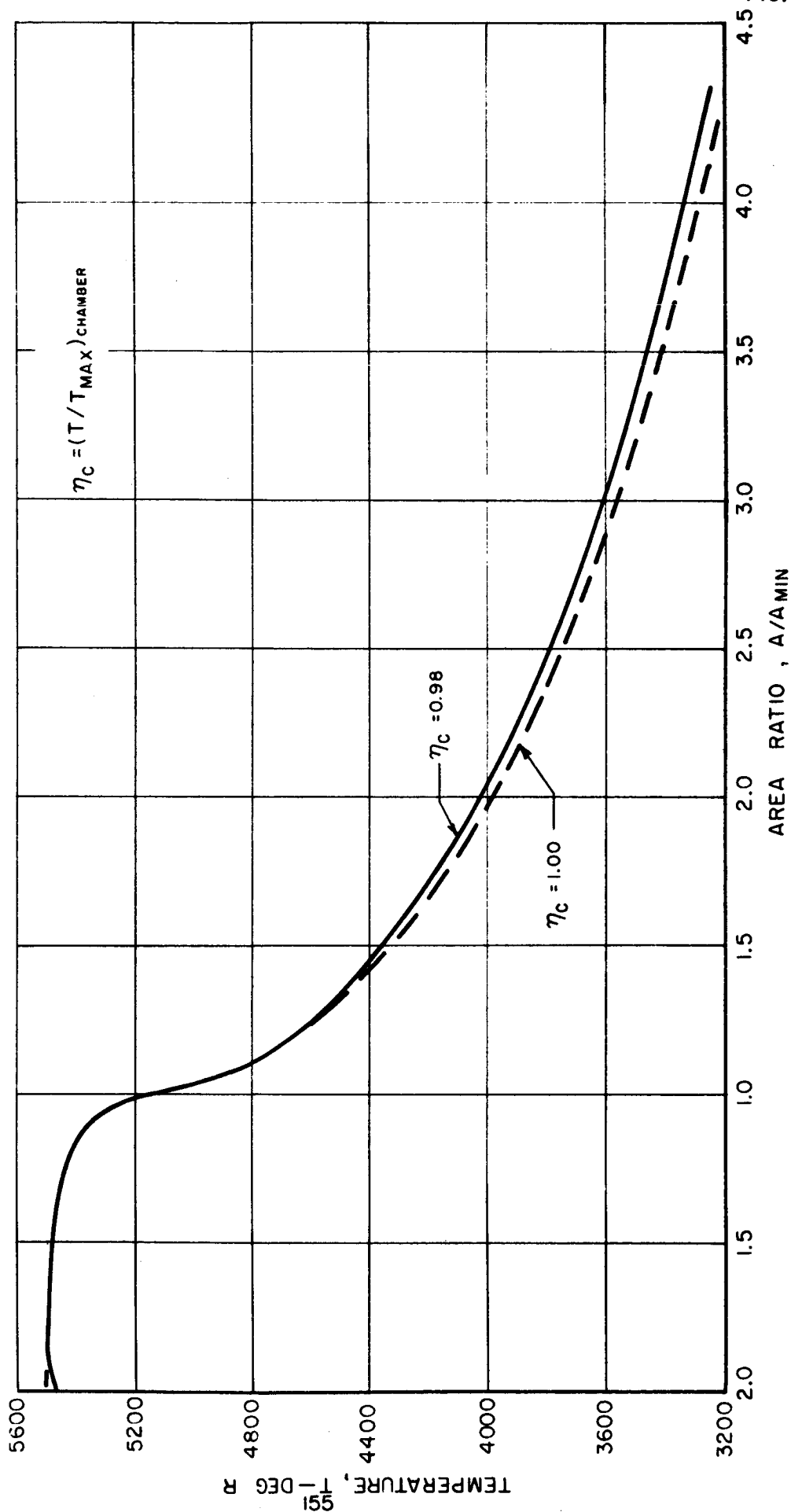


FIG. 25

OPTIMIZATION MAP

PROPELLANT SYSTEM: H_2-O_2 $O/F = 5.0$ $P_c = 60$ PSIATHROAT RADIUS: $R_0 = 0.054$ FT $\frac{\text{RADIUS OF CURVATURE}}{\text{THROAT RADIUS}} = 2.0$

$$\frac{\text{THRUST}}{P_c A_{\text{THROAT(MIN)}}} = C_{Tg}$$

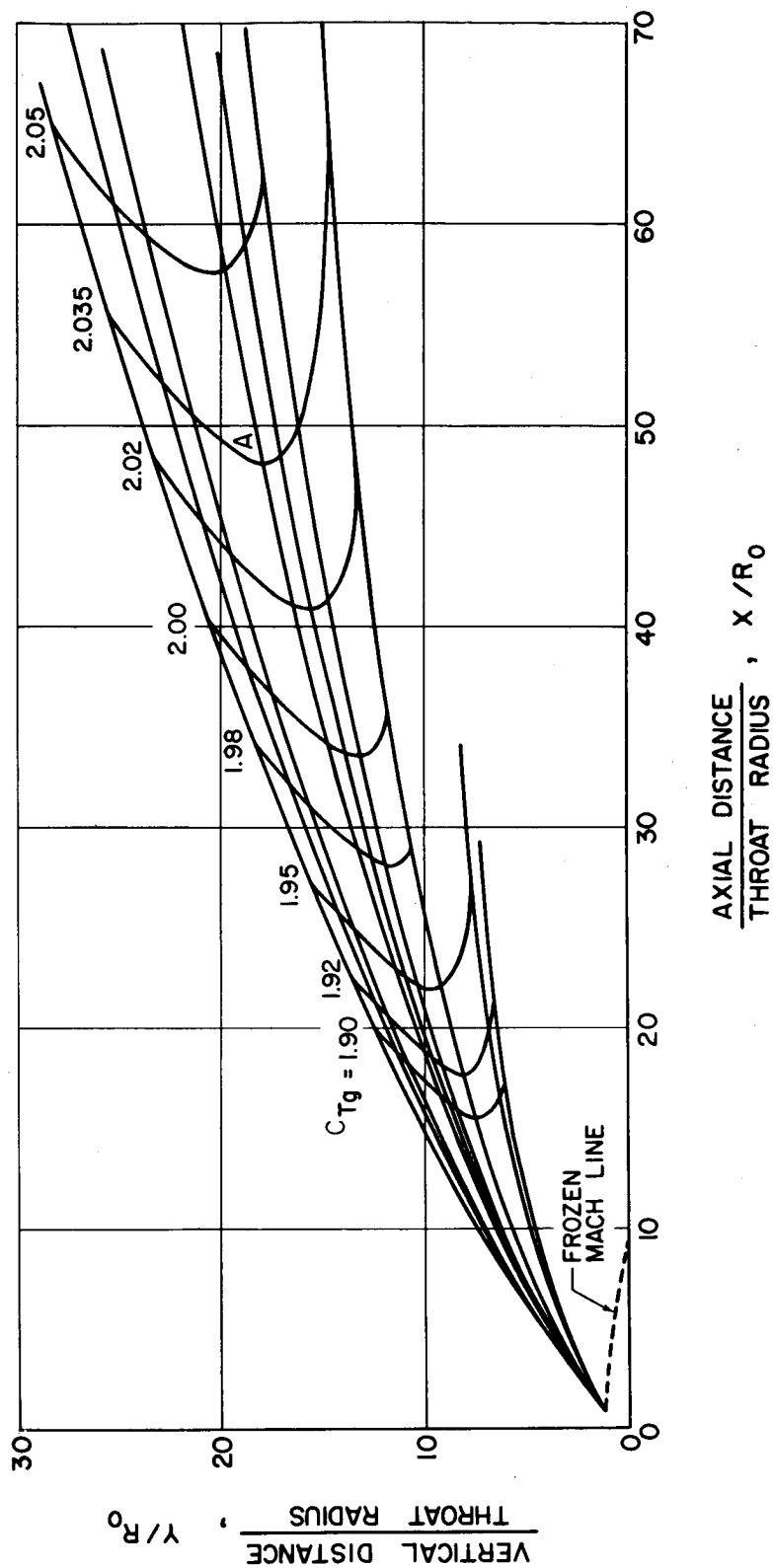
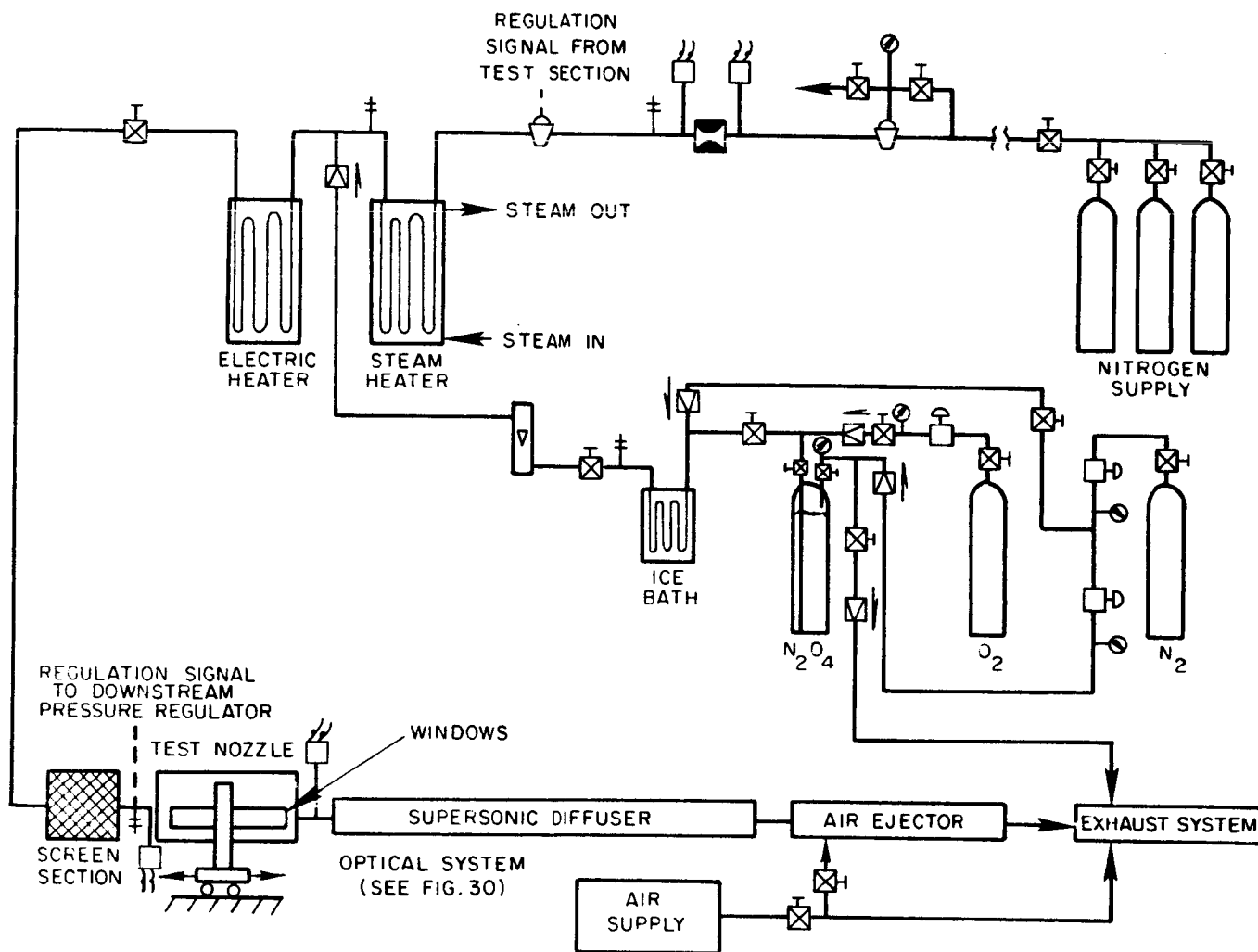











DIAGRAM OF EXPERIMENTAL APPARATUS



-  SMALL-VOLUME PRESSURE REGULATOR
-  LARGE-VOLUME PRESSURE REGULATOR
-  MANUAL SHUT-OFF VALVE
-  PRESSURE TRANSDUCER
-  ASME LONG RADIUS FLOW NOZZLE

-  CHECK VALVE
-  THERMOCOUPLE
-  PRESSURE GAUGE
-  VARIABLE AREA FLOWMETER

SCHEMATIC DIAGRAM OF TEST NOZZLE

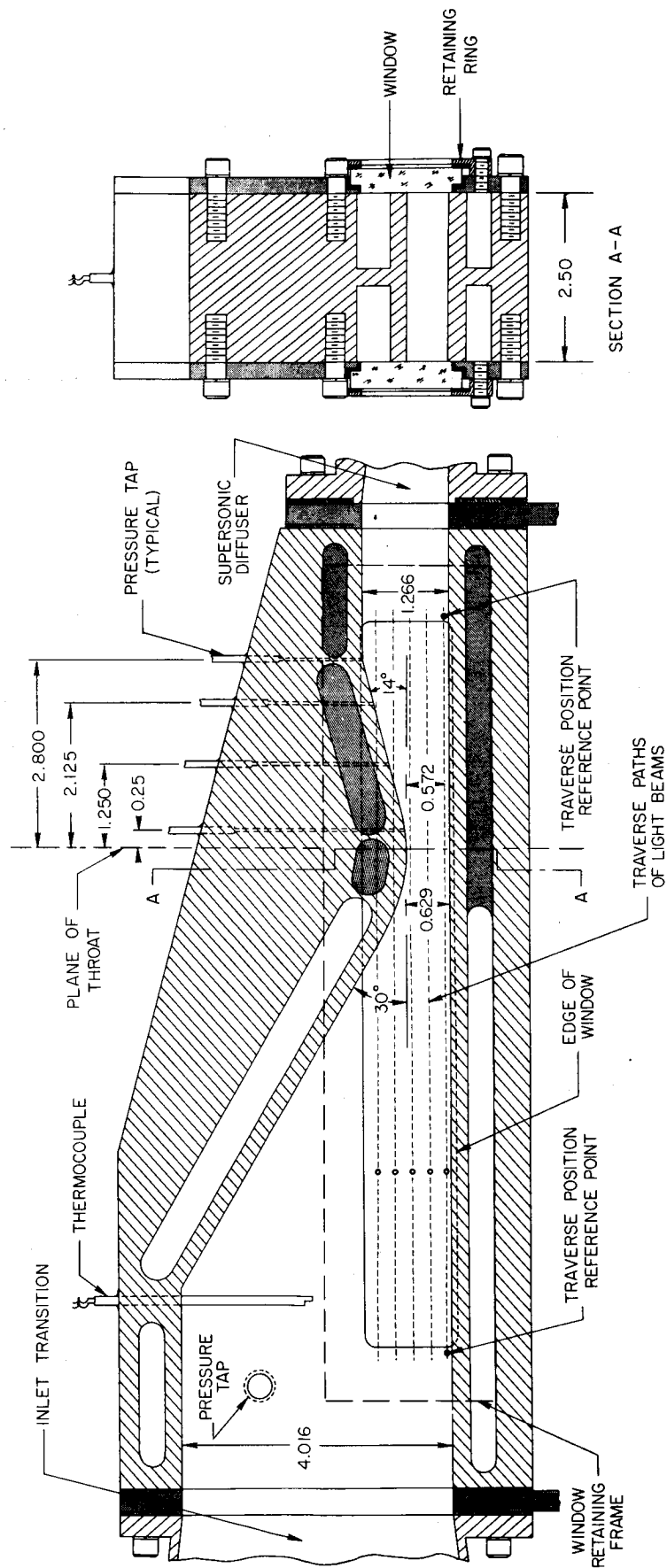
CONVERGENCE AREA RATIO = 6.385

DIVERGENCE AREA RATIO = 2.013

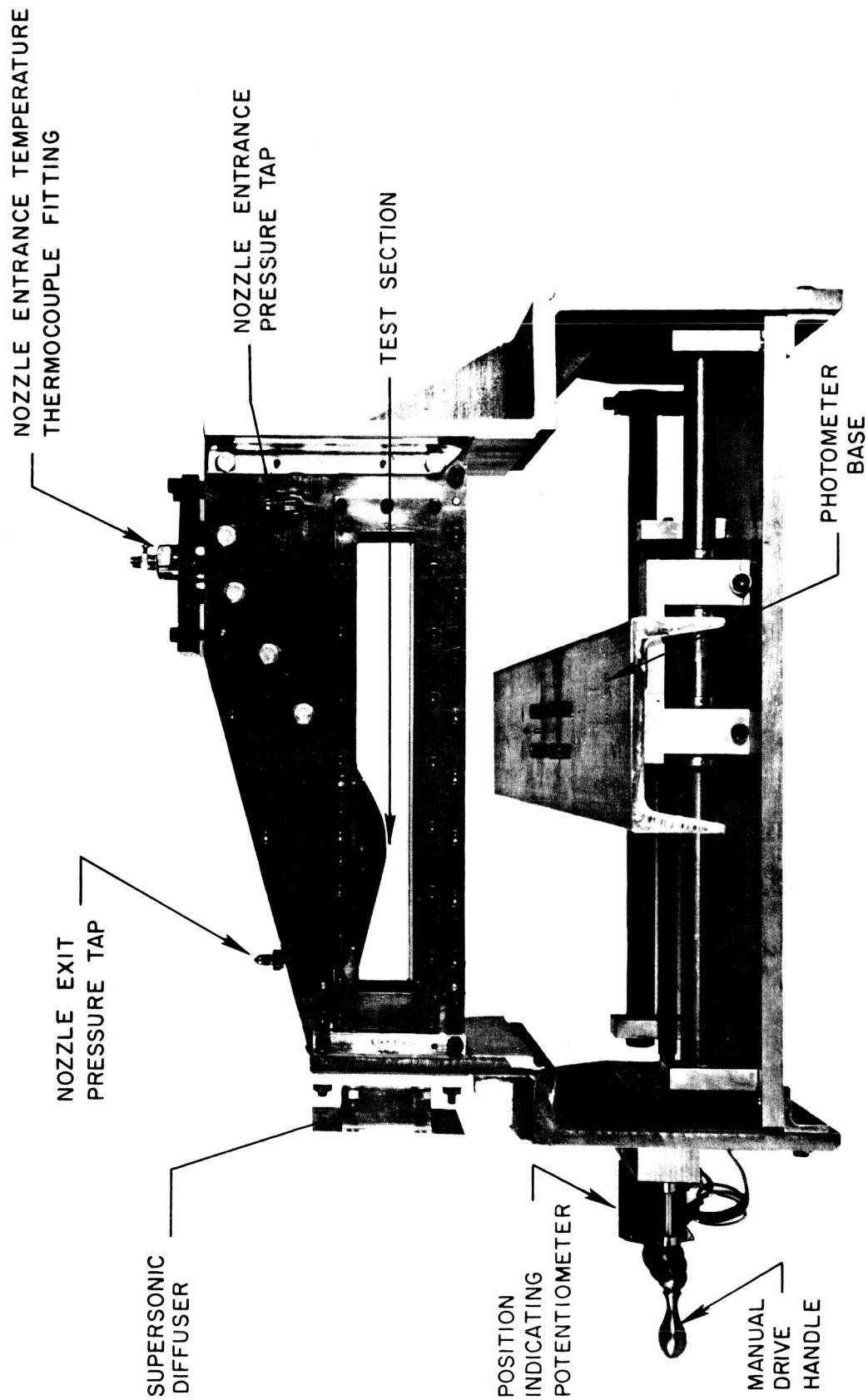
BLENDED THROAT RADIUS = 2.50 in.

VERTICAL SPACE BETWEEN LIGHT BEAMS = 0.25 in.

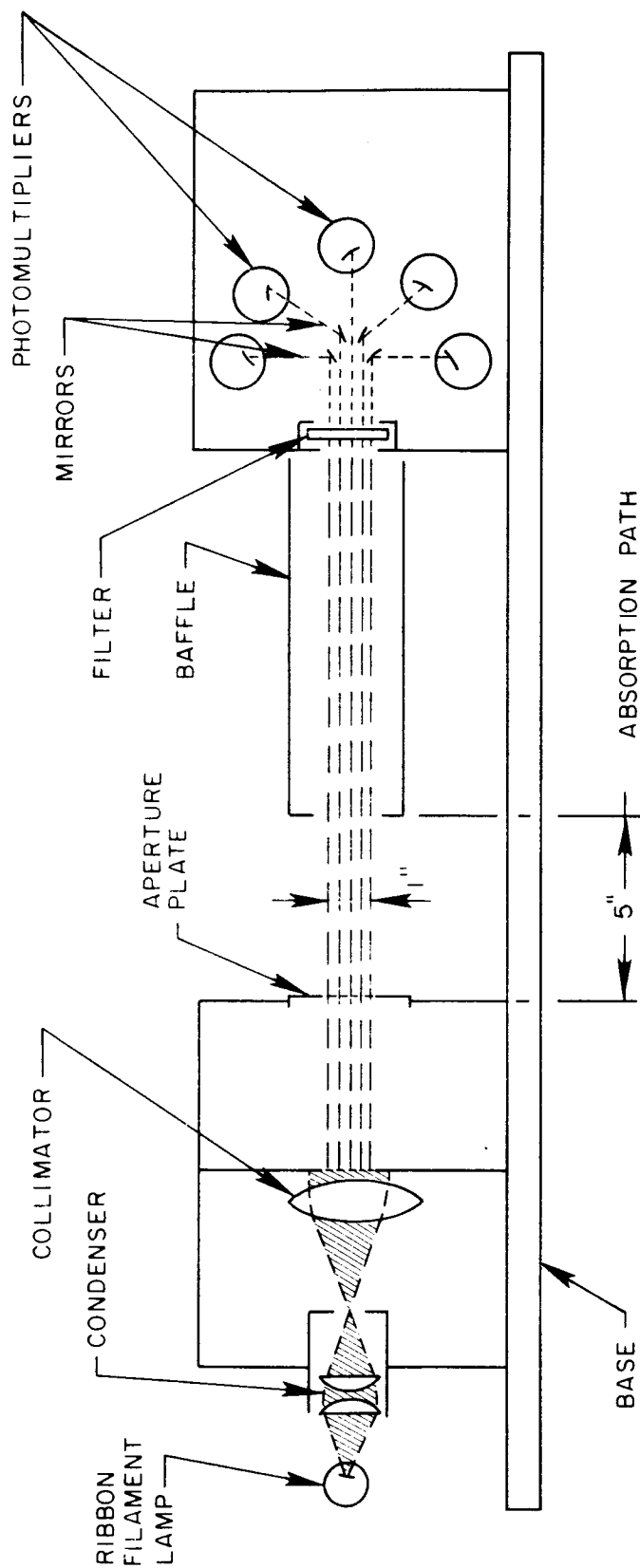
DIVERGENCE OF LOWER WALL FROM NOZZLE THROAT = $0^{\circ} 15'$



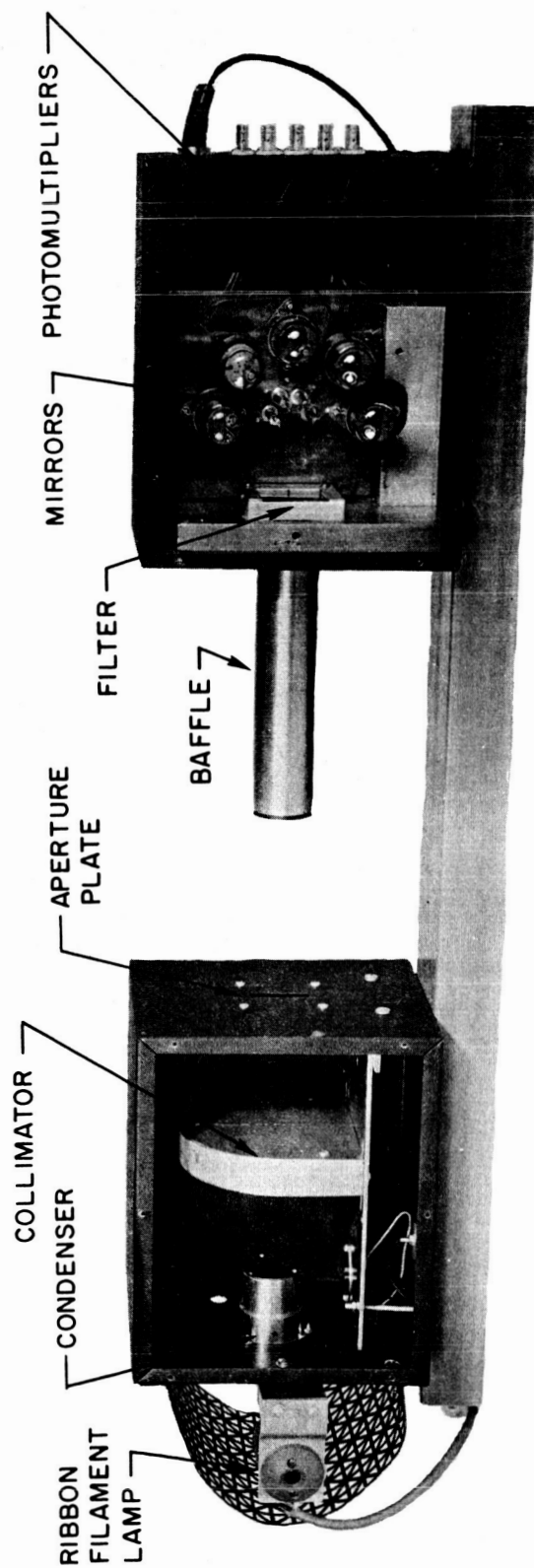
PHOTOGRAPH OF TEST NOZZLE AND TRAVERSING MECHANISM



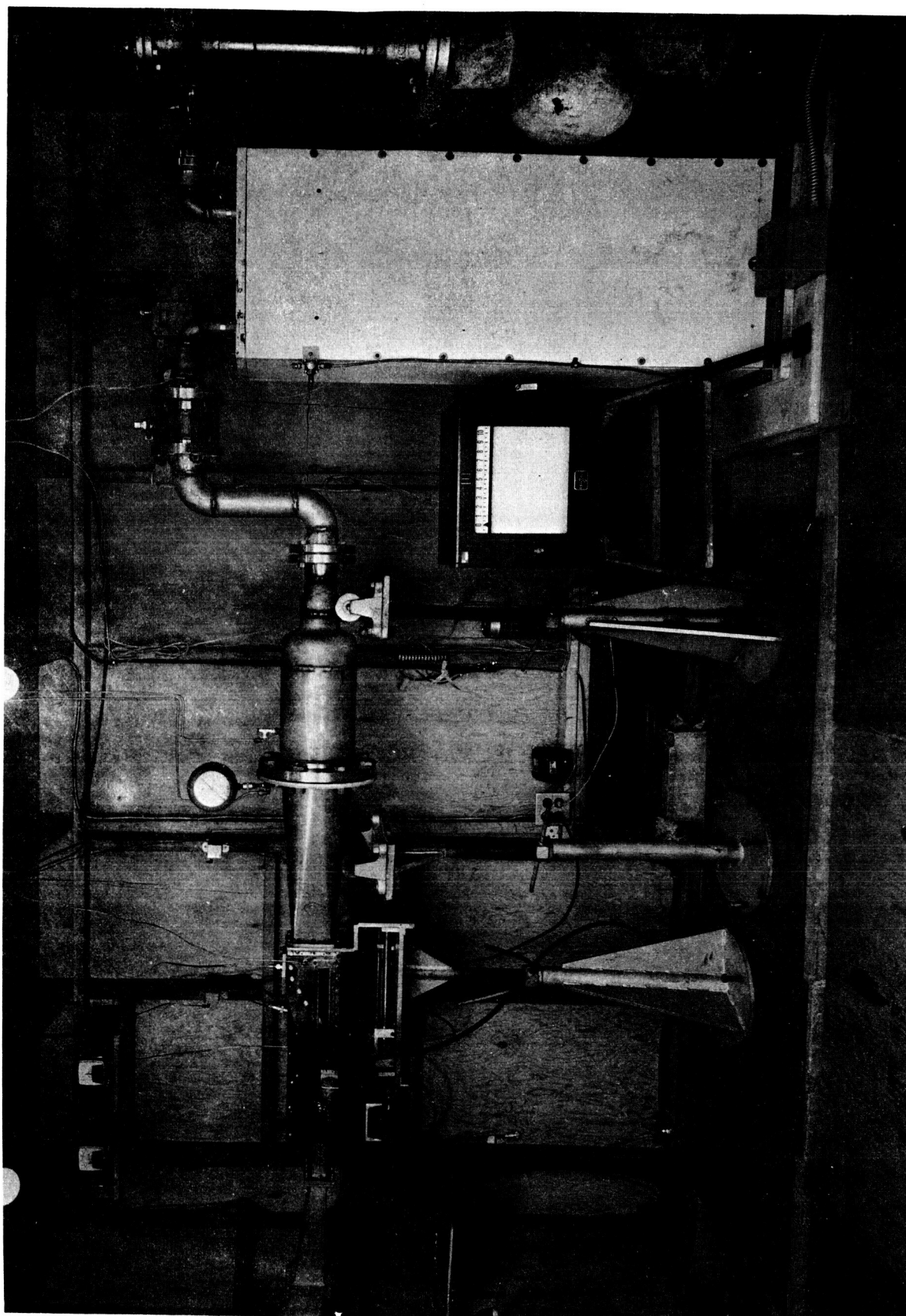
FIVE BEAM ABSORPTION PHOTOMETER



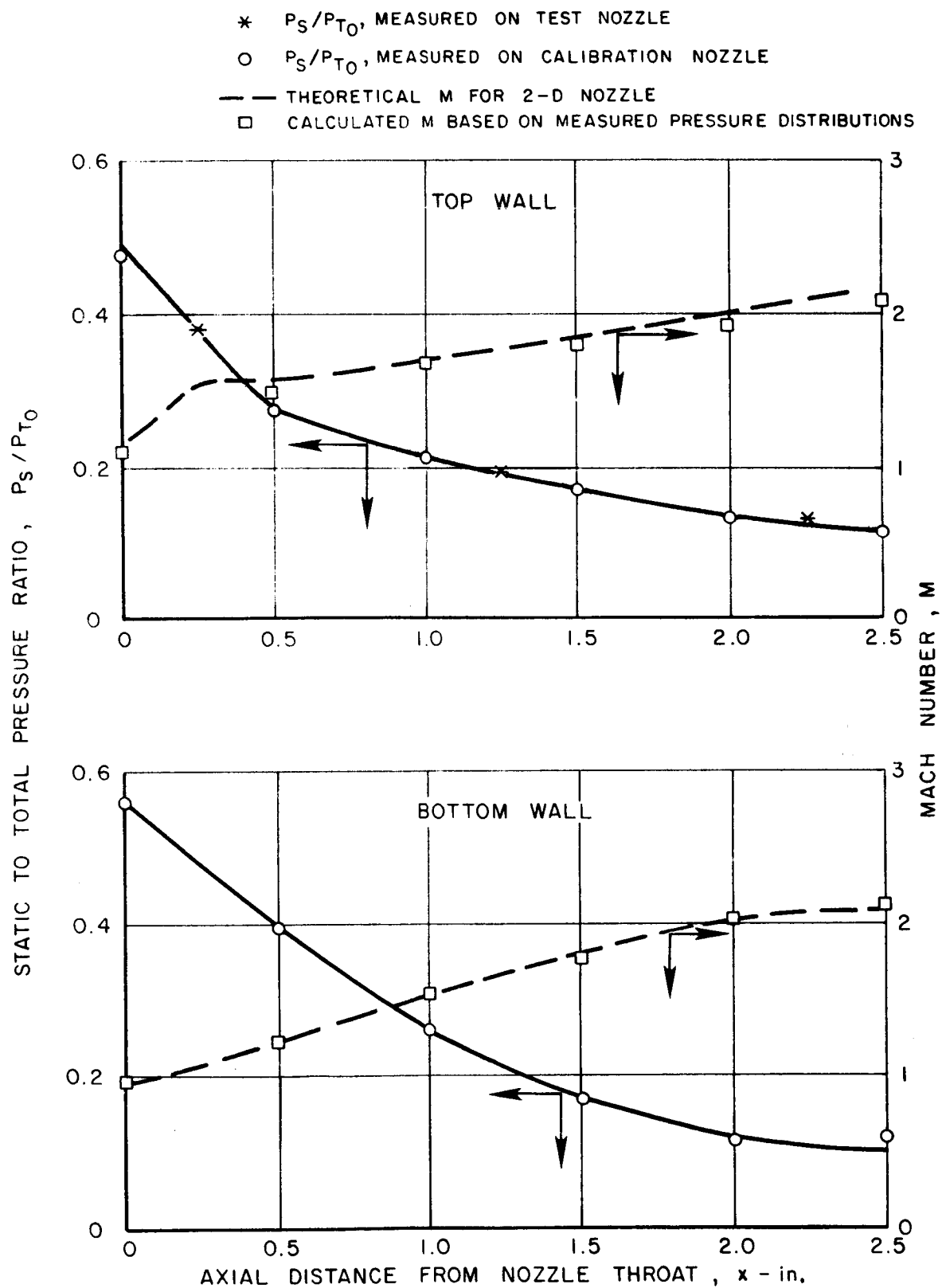
FIVE BEAM ABSORPTION PHOTOMETER

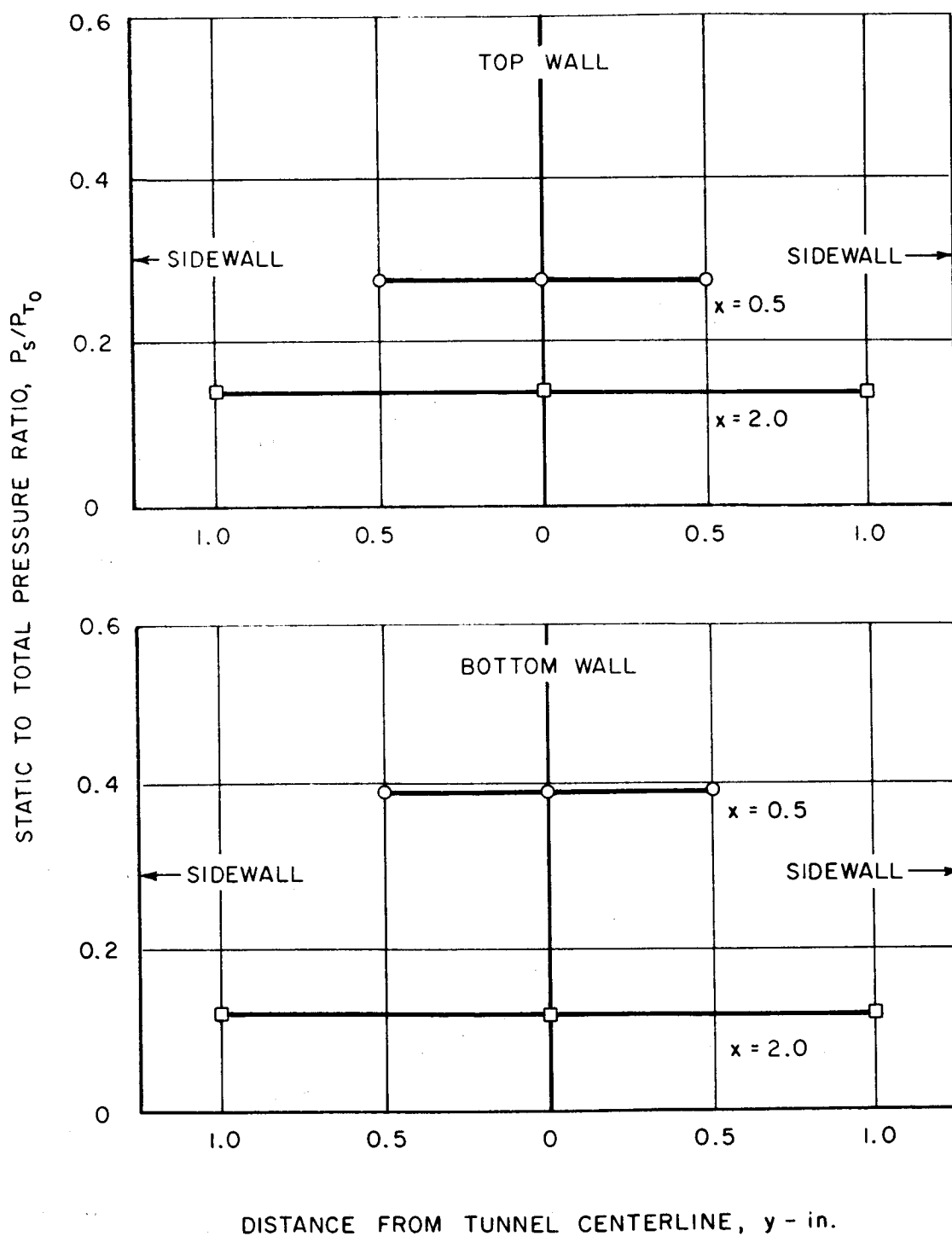


PHOTOGRAPH OF MAIN TEST SECTION

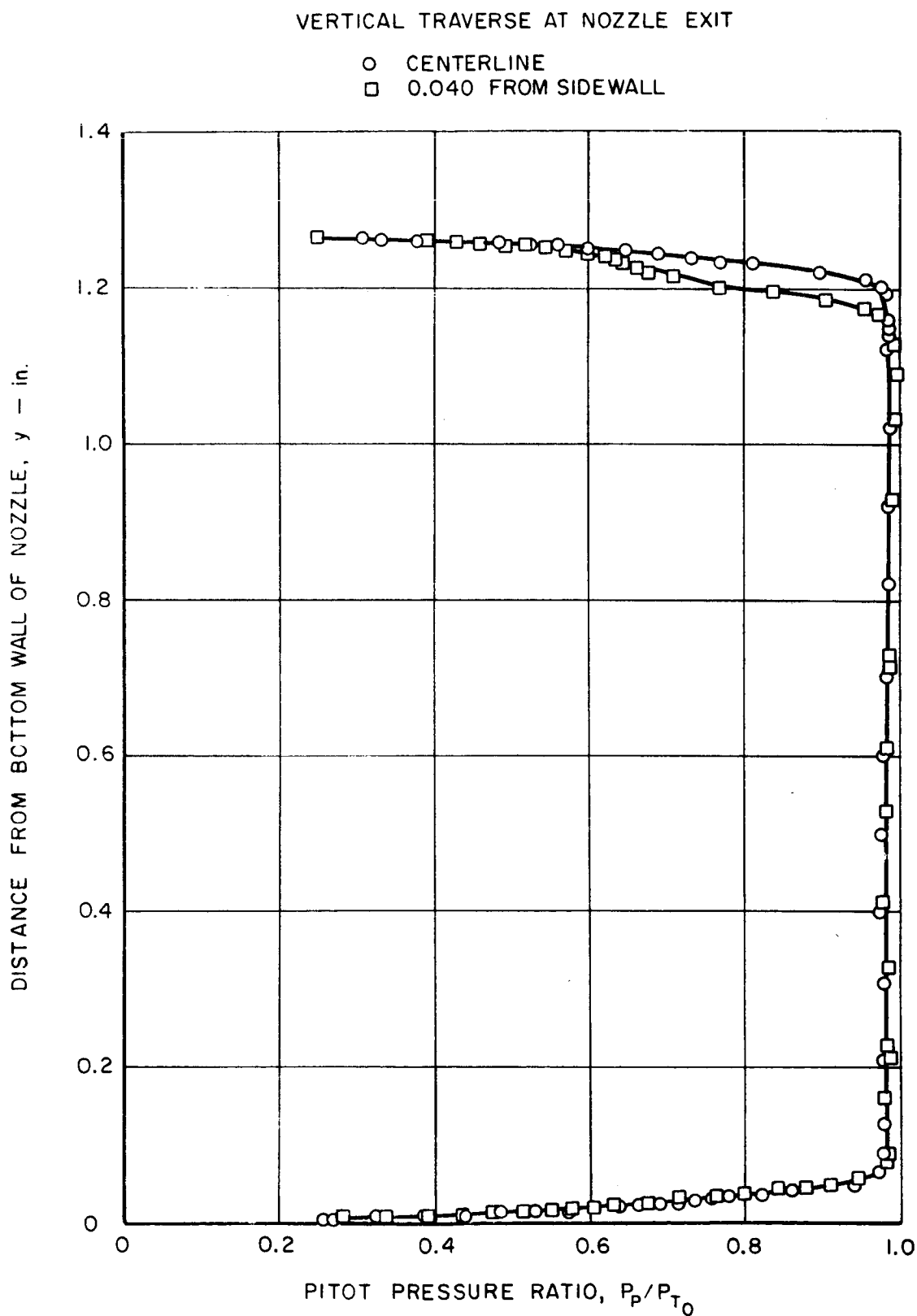


VARIATION OF MACH NUMBER AND PRESSURE RATIO WITH AXIAL DISTANCE FROM NOZZLE THROAT

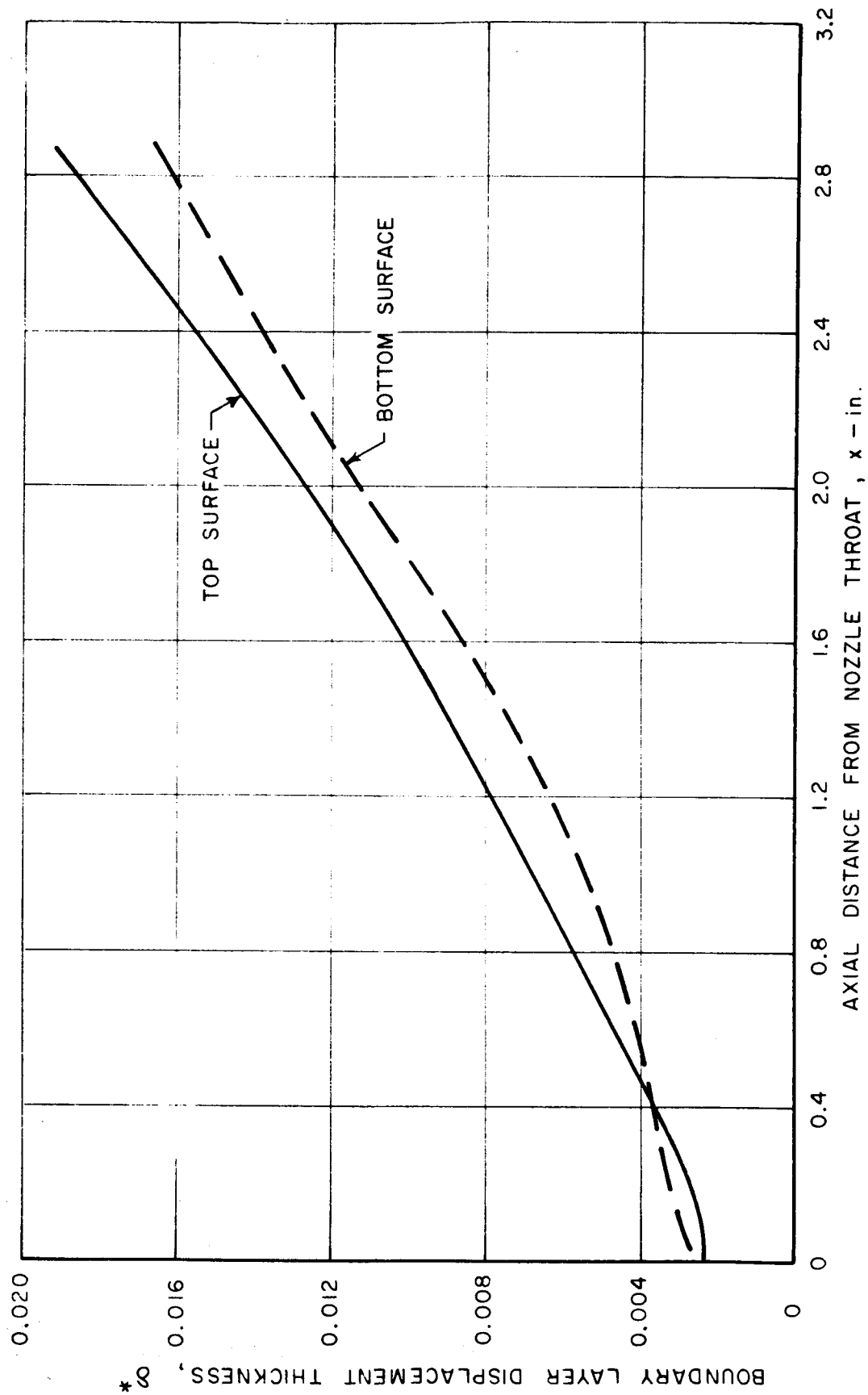


TRANSVERSE PRESSURE DISTRIBUTIONS AT VARIOUS
AXIAL LOCATIONS IN CALIBRATION NOZZLE

VARIATION OF PITOT PRESSURE RATIO WITH DISTANCE FROM BOTTOM WALL OF NOZZLE

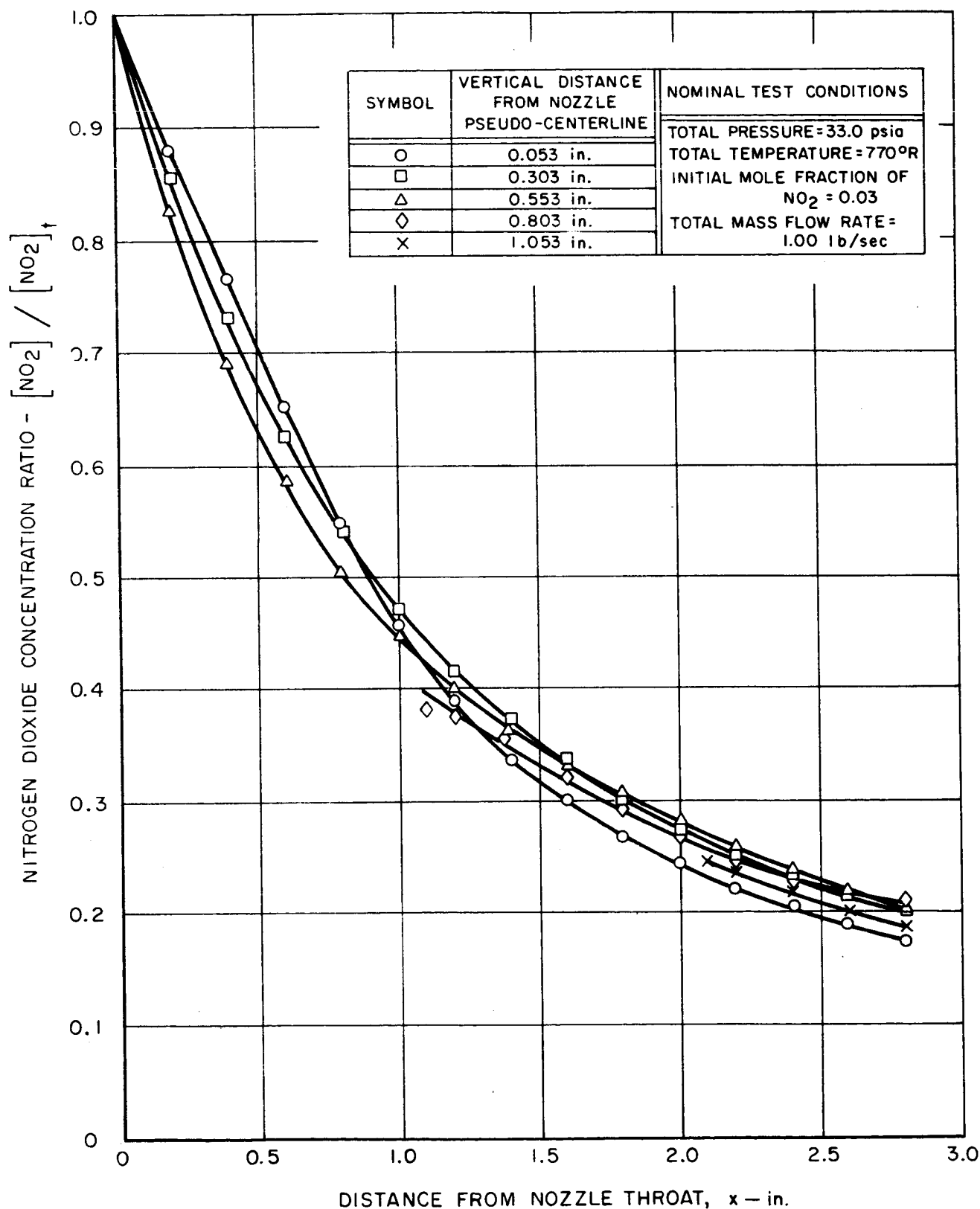


VARIATION OF BOUNDARY LAYER DISPLACEMENT THICKNESS
WITH AXIAL DISTANCE FROM NOZZLE THROAT



VARIATION OF NITROGEN DIOXIDE CONCENTRATION RATIO IN THE SUPERSONIC PORTION OF THE TEST NOZZLE

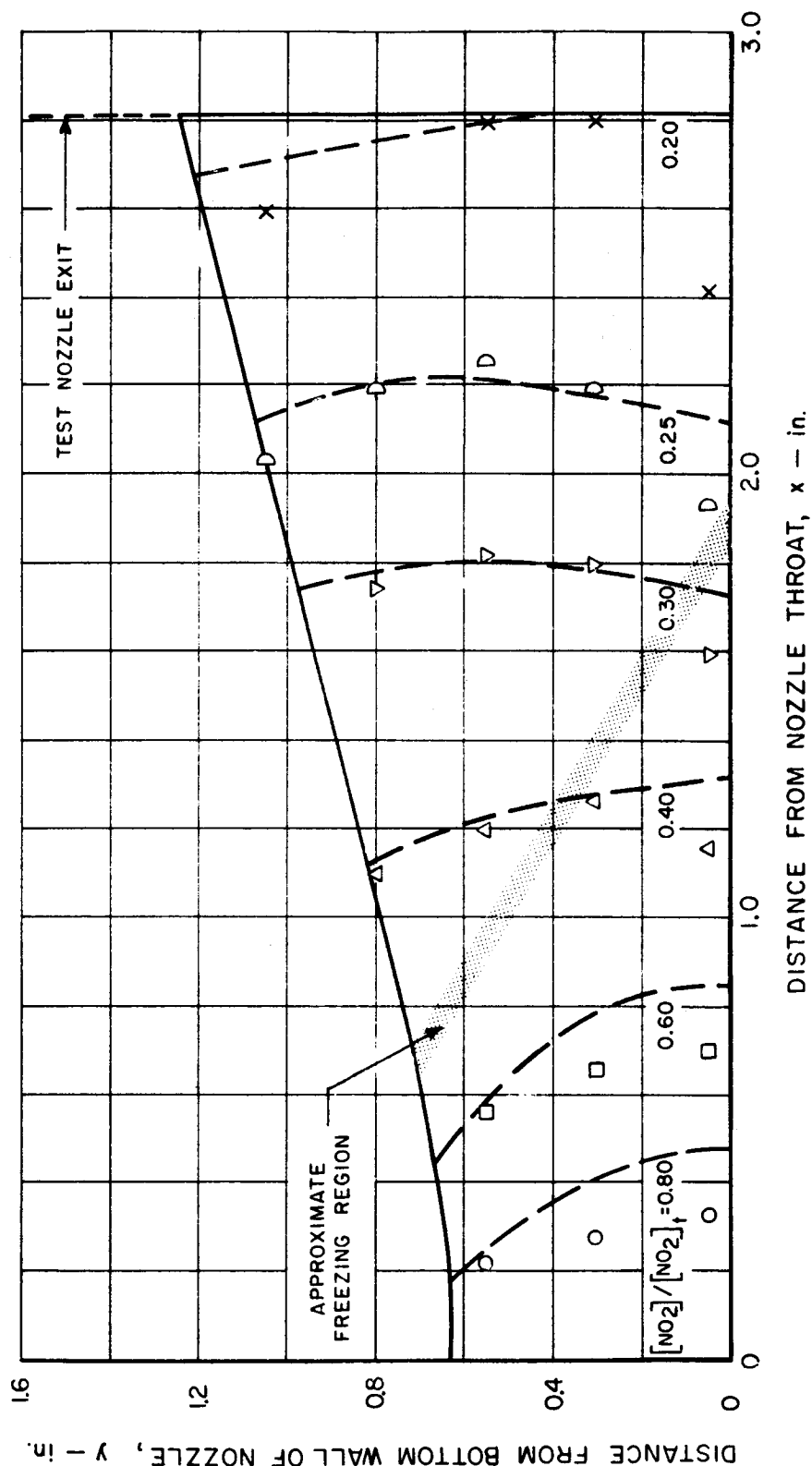
NOTE: DATA PRESENTED ARE AVERAGED FROM THREE EXPERIMENTS



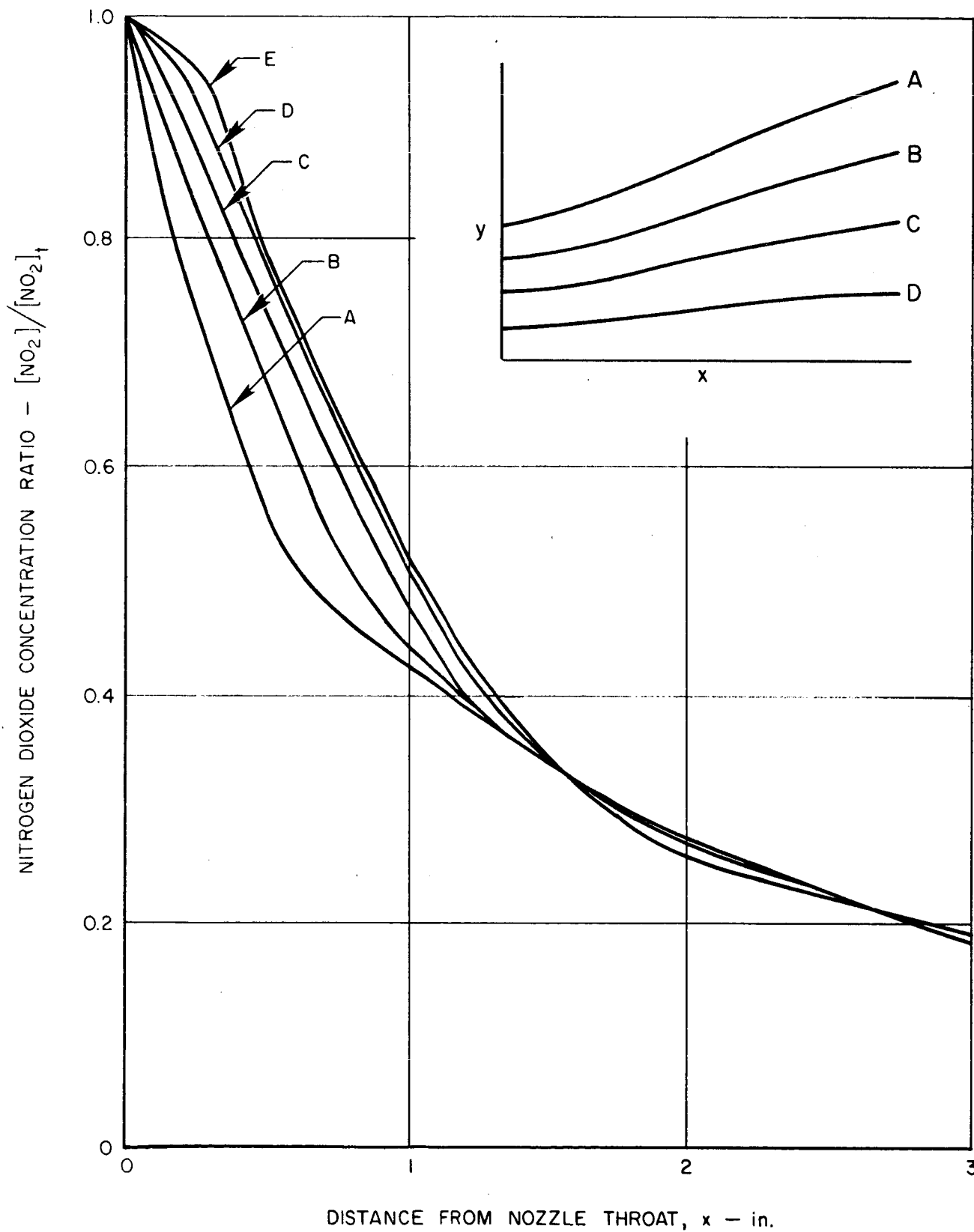
COMPARISON OF PREDICTED AND MEASURED NITROGEN DIOXIDE CONCENTRATION RATIOS IN SUPERSONIC PORTION OF TEST NOZZLE

NOTE: DATA PRESENTED ARE AVERAGED FROM THREE EXPERIMENTS

SYMBOL	$[NO_2]/[NO_2]_t$	NOMINAL TEST CONDITIONS	
		TOTAL PRESSURE = 33.0 psia	TOTAL TEMPERATURE = 770 °R
O	0.80	INITIAL MOLE FRACTION OF $NO_2 = 0.03$ TOTAL MASS FLOW RATE = 1.0 lb/sec	
□	0.60		
△	0.40		
▽	0.30		
D	0.25		
X	0.20		



CALCULATED VARIATION OF NITROGEN DIOXIDE CONCENTRATION
RATIO IN THE SUPERSONIC PORTION OF THE TEST NOZZLE



PHOTOMULTIPLIER TUBE CIRCUIT

